

Measurements of the Transverse Emittance at the VUV-FEL

Diploma Thesis
by
Florian Lühl

submitted to the
Department of Physics of the University of Hamburg

prepared at
Deutsches Elektronen-Synchrotron (DESY), Hamburg

DESY-THESIS 2005-014
TESLA-FEL 2005-03

Hamburg, July 2005

Abstract

The TESLA Test Facility (TTF) linear accelerator (linac) at DESY has been extended to drive a new Free Electron Laser facility (VUV-FEL) in the wavelength range from the vacuum-ultraviolet (VUV) to soft X-rays. With the upgraded photo injector and increased electron beam energy up to 1 GeV, wavelengths down to 6 nm can be achieved. During the commissioning phase of the VUV-FEL the emphasis is on lasing with a wavelength of 30 nm.

A high quality electron beam is required for the lasing process. At the VUV-FEL the design values are 2 mm mrad normalized transverse emittance, 2500 A peak current, and 0.1 % energy spread.

In order to understand and optimize the electron beam, precise measurements of the beam properties are essential. In this diploma thesis, measurements of the transverse emittance during the commissioning of the VUV-FEL are presented. The transverse beam distribution is measured using optical transition radiation at four positions along the linac. The emittance is determined from the measured distributions using two methods: a fit of the Twiss parameters together with the emittance to the measured beam sizes, and as a second method, the tomographic reconstruction of the phase space density distributions using the Maximum Entropy Algorithm.

Zusammenfassung

Um eine neue Freie-Elektronen Laser Anlage zu betreiben, ist der Linearbeschleuniger der TESLA Test Anlage (TTF) am DESY erweitert worden. Mit dem verbesserten Photoinjektor und einer erhöhten Strahlenergie von bis zu 1 GeV kann FEL-Strahlung im Wellenlängenbereich vom Vakuum-Ultraviolett (VUV) bis zu weicher Röntgenstrahlung (6 nm) erzeugt werden. Während der Inbetriebnahme des VUV-FEL wird ein Laserbetrieb mit einer Wellenlänge von 30 nm angestrebt.

Eine hohe Strahlqualität ist wichtig für den Laserprozess. Am VUV-FEL liegen die Designwerte der normierten transversalen Strahlemittanz bei 2 mm mrad, des Spitzenstroms bei 2500 A und der Energiebreite bei 0.1 %.

Für das Verständnis und zum Optimieren des Elektronenstrahls sind präzise Messungen der Elektronenstrahl-Eigenschaften essentiell. Im Rahmen dieser Diplomarbeit werden Messungen der transversalen Strahlemittanz während der Inbetriebnahme präsentiert. Die transversale Strahlverteilung wird an vier Positionen im Beschleuniger mit Hilfe von optischer Übergangsstrahlung gemessen. Aus diesen Verteilungen wird die Strahlemittanz über zwei verschiedene Methoden bestimmt: aus einem Fit der Twiss Parameter und der Strahlemittanz an die gemessenen Strahlbreiten und zum anderen aus der tomographischen Rekonstruktion der Phasenraum-Dichteverteilung unter Benutzung des Maximum-Entropie-Algorithmus.

Florian Löh
Deutsches Elektronen-Synchrotron
Notkestraße 85
22607 Hamburg, Germany
florian.loehl@desy.de

German title:
Messungen der transversalen Emittanz am VUV-FEL

Published under DESY report numbers:
DESY-THESIS 2005-014
TESLA-FEL 2005-03

Printed by the DESY copy center.
This document was typeset using \LaTeX and KOMA-Script.

Contents

1	Introduction	1			
1.1	The VUV-FEL	2			
2	Linear beam dynamics and beam parameters	3			
2.1	Transfer matrix formalism	3			
2.2	Liouville’s theorem	4			
2.3	Two-dimensional phase space ellipse	5			
2.4	Beam matrix	5			
2.5	Statistical definition of the beam matrix	6			
2.6	Different definitions of the transverse beam emittance	6			
3	Determination of the transverse emittance	9			
3.1	Determination of the (2D) emittance	9			
3.2	Fitting of the measured data	9			
3.3	Error estimation of the fitted parameters	10			
3.4	Determination of the intrinsic emittance	10			
3.5	Tomographic phase space reconstruction	11			
4	Experimental setup	15			
4.1	Injector	15			
4.2	First bunch compressor section (BC2 section)	15			
4.3	SUND diagnostic section	16			
4.4	OTR monitors	16			
4.4.1	Optical transition radiation	18			
4.4.2	OTR monitors	18			
5	Systematic errors	21			
5.1	Mismatch parameter	21			
5.2	Dependence of the determined emittance on the mismatch for different errors in the beam sizes	21			
5.3	Dependence of the determined emittance on energy errors	21			
5.4	Simulation of the (2D) phase space reconstruction with the MENT Algorithm in the BC2 section	23			
6	Image analysis	27			
6.1	Image analysis algorithm to reconstruct the second moments of the entire beam	27			
6.2	Beam intensity cut to calculate the core emittance	28			
6.3	Noise reduction with filters	29			
6.4	Determination of MENT profiles	29			
7	Measurements	31			
7.1	Calibration of the OTR monitors	31			
7.2	Emittance measurements	31			
7.2.1	Matching of the Twiss parameters in the BC2 diagnostic section	31			
7.2.2	Dependence of the emittance on the main solenoid current	33			
7.2.3	Dependence of the emittance on the ACC1 off-crest phase	33			
7.2.4	Reproducibility of the emittance measurements	36			
7.2.5	Smallest emittances measured	36			
8	Conclusion	41			
A	Transfer matrices of important beam line elements	43			
B	Symplectic transformation to calculate the intrinsic emittances	44			
C	Tables with measurement results	45			

List of Tables

4.1	Calibration constants and magnetic lengths of TQA type quadrupoles	15	C.1	Measured normalized horizontal rms emittances for different main solenoid currents	45
4.2	Twiss parameters for matched optics in the BC2 and SUND diagnostic sections	16	C.2	Measured normalized vertical rms emittances for different main solenoid currents	46
5.1	MENT simulation in the BC2 section	24	C.3	Measured normalized rms emittances for different ACC1 off-crest phases (horizontal plane)	47
7.1	Calibration factors for the OTR monitors in the BC2 diagnostic section	32	C.4	Measured normalized rms emittances for different ACC1 off-crest phases (vertical plane)	48
7.2	Example for a matching procedure of the Twiss parameters in the BC2 diagnostic section	33	C.5	Reproducibility of the emittance measurement (horizontal plane)	49
7.3	Smallest emittances measured	36	C.6	Reproducibility of the emittance measurement (vertical plane)	49

List of Figures

1.1	Comparison of the peak brilliance of conventional synchrotron radiation sources with SASE free electron lasers	1	5.5	Example for MENT reconstruction in the BC2 diagnostic section	25
1.2	Schematic layout of the VUV-FEL	2	6.1	Dependence of the reconstructed beam sizes on the size of the region-of-interest	27
2.1	Accelerator coordinate system	3	6.3	Example images to demonstrate the image analysis algorithm	28
2.2	Phase space ellipse	6	6.2	Projection of the measured 2D distribution onto the y -axis for the entire image and for the region-of-interest	29
3.1	Example of MENT reconstruction using rotation matrices	13	6.4	Example image to demonstrate the intensity cut performed to calculate core emittances	29
4.1	Layout of the injector and the BC2 section	16	6.5	Projection of the region-of-interest onto the y -axis with and without applying a wavelet filter	30
4.2	Periodic solution for the beta functions in the BC2 diagnostic section	17	6.6	Difference between original and wavelet filtered image	30
4.3	Layout of the SUND diagnostic section	17	7.1	Calibration of the OTR monitors	32
4.4	Periodic solution for the beta functions in the SUND FODO lattice	17	7.2	Normalized emittance versus the current of the main solenoid	33
4.5	Angular distribution of the transition radiation for an electron crossing a metallic foil	18	7.3	Reconstructed phase space distributions (horizontal plane) for different currents of the main solenoid	34
4.6	Transition radiation for normal and oblique incidence	19	7.4	Reconstructed phase space distributions (vertical plane) for different currents of the main solenoid	35
4.7	Standard VUV-FEL OTR monitor	19	7.5	Normalized emittance versus the phase of the accelerator module ACC1	36
5.1	Graphical representation of the phase space ellipse in normalized coordinates	22	7.6	Reconstructed phase space distributions (horizontal plane) for different phases of the accelerator module ACC1	37
5.2	Results of Monte Carlo simulations for a mismatched beam in the BC2 section	22	7.7	Reconstructed phase space distributions (vertical plane) for different phases of the accelerator module ACC1	38
5.3	Relative error in the horizontal emittance as a function of the Twiss parameters α_x and β_x on the first screen (4DBC2) in the BC2 diagnostic section for beam size errors of 5%	23	7.8	Reproducibility of the measured emittance	39
5.4	Relative deviation of the normalized horizontal emittance as a function of the Twiss parameters α_x and β_x on the first screen (4DBC2) in the BC2 diagnostic section for an energy deviation of 5%	24			

1 Introduction

Synchrotron radiation is a powerful diagnostic tool applied in many different disciplines ranging from physics, chemistry, and biology to material sciences, geophysics, and medical diagnostics. It offers a broad spectrum, ranging from the infrared to the hard X-ray regime. For many experiments the relevant figure of merit of a synchrotron light source is the *brilliance*, which is defined for transversely coherent radiation sources as

$$\text{brilliance} = \frac{\text{spectral flux}}{\left(\frac{\lambda}{2}\right)^2}. \quad (1.1)$$

Synchrotron radiation is generated when high energy electrons are deflected in magnetic fields. In the first generation of light sources the synchrotron light was generated in bending magnets. Higher brilliances can be reached using wigglers and undulators¹ instead of bending magnets.

In free electron lasers (FEL), often considered to be the fourth generation of light sources, the electrons radiate coherently. This yields an increase of many orders of magnitude in brilliance. An overview of the brilliance for different types of synchrotron light sources is given in Fig. 1.1. The radiation field generated inside an undulator magnet interacts with the electron beam. This interaction can be achieved in two different ways. In a *low-gain* FEL an optical cavity similar to that in a classical laser is used to amplify the synchrotron light in many reflection cycles. This works only for wavelengths in the infrared, visible, and soft ultraviolet regime. For shorter wavelengths no suitable backward reflecting mirrors are available. Therefore, FELs in the X-ray regime need to achieve laser amplification and saturation within a single pass of the electron beam through the undulator (*high-gain* FEL). The interaction of the undulator radiation with the electron bunches produces a longitudinal charge density modulation inside the electron bunches, called *microbunching*. Many electrons in these microbunches start to radiate coherently, which leads to an exponential growth of the radiation intensity along the undulator.

One way to initialize the lasing process is through *Self-Amplified Spontaneous Emission* (SASE). Spontaneous undulator radiation with a wavelength λ_{ph} fulfilling the resonance condition of the undulator

$$\lambda_{ph} = \frac{\lambda_u}{2\gamma_{rel}^2} \left(1 + \frac{K^2}{2}\right) \quad \text{with} \quad K = \frac{eB_u\lambda_u}{2\pi m_e c} \quad (1.2)$$

is amplified along the undulator. Here λ_u is the period length of the undulator, $\gamma_{rel} = E/m_e c^2$, E the electron energy, e the elementary charge, c the speed of light in vacuum, and B_u the peak magnetic field in the undulator. Equation (1.2) shows that the photon wavelength λ_{ph} can easily be tuned by changing the energy of the electron beam.

The lasing process in a high gain FEL depends critically on the quality of the driving electron beam. The gain G of an external electromagnetic wave travelling along the undulator is defined as (high gain definition)

$$G = \frac{\text{field energy at exit}}{\text{initial field energy}}.$$

¹ Structures with periodically alternating transverse magnetic fields.

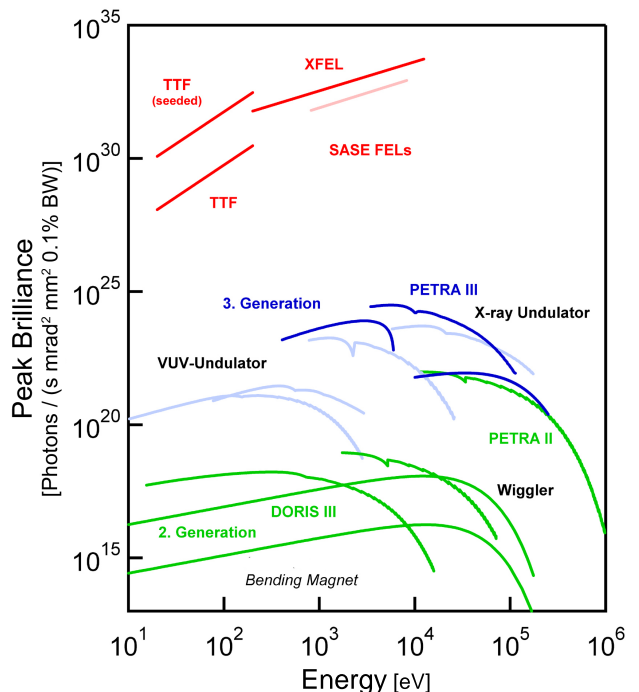


Figure 1.1: Comparison of the peak brilliance of conventional synchrotron radiation sources with SASE free electron lasers.

In case of a mono-energetic electron beam matching the resonance energy and neglecting three dimensional effects, the gain G increases exponentially along the undulator [SSY99]

$$G(z) \propto \exp\left(\frac{z}{L_G}\right) \quad \text{for} \quad z \gg L_G \quad (1.3)$$

and the gain length L_G is proportional to

$$L_G \propto \left(\frac{\sigma_t^2}{I_0}\right)^{\frac{1}{3}}. \quad (1.4)$$

The quantity σ_t denotes the transverse rms beam size and I_0 is the peak current. We can realize that a high peak current and a small transverse beam size are needed to obtain a short gain length. As we will see later, the beam size is proportional to the square root of the transverse beam emittance ϵ , a quantity describing the occupied area in the transverse phase space.

In a real accelerator, however, the beam is not mono-energetic and three dimensional effects like the beam emittance cannot be neglected. A beam energy spread induces a longitudinal velocity spread, which drastically increases the gain length [SSY99]. The transverse beam emittance leads to an additional longitudinal velocity spread, since particles with the same energies but different angles with respect to the design orbit have different longitudinal velocities. This velocity spread can be considered as an additional contribution to the energy spread. Assuming a Gaussian transverse phase space distribution, this contribution is proportional to the square of the emittance [SSY99]. Therefore, an electron beam with a small energy spread and a small transverse emittance is needed to drive a free electron laser.

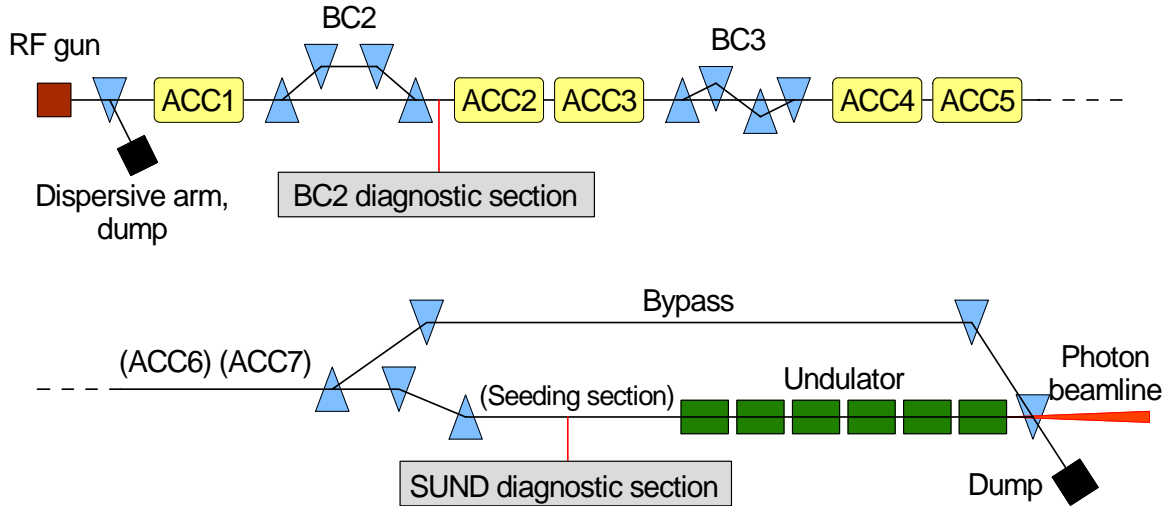


Figure 1.2: Schematic layout of the VUV-FEL. The electron source is an RF photo-injector. The electrons are accelerated in five modules (ACC1 to ACC5) up to an energy of 800 MeV. In order to reach energies of up to 1 GeV two additional modules ACC6 and ACC7 can be added at a later stage. The bunches are longitudinally compressed in two bunch compressors BC2 and BC3. The locations of the diagnostic sections dedicated to emittance measurements (BC2 and SUND diagnostic section) are indicated in the figure. The total length is about 250 m.

The high demands on the beam quality make accurate beam diagnostic tools essential for the understanding and optimization of the machine. Within this diploma thesis measurements of the transverse emittance at the VUV-FEL at DESY during the commissioning of the machine are presented. The measurements are performed using a four screen method. At optical transition radiation screens at four different positions along the beam line the spatial beam distribution is measured. From these measurements the emittance is determined in two different ways: by a fit of the Twiss parameters and the emittance to the measured beam sizes, and from the tomographic reconstruction of the phase space density distribution using the Maximum Entropy Algorithm.

1.1 The VUV-FEL

The VUV-FEL² [The02] is a new SASE FEL user facility at DESY (Hamburg). It is an upgrade of the TESLA Test Facility (TTF) linac³, which was operated until November 2002 to perform various tests related to the TESLA⁴ Linear Collider Project [B⁺01] and to drive a SASE FEL at a wavelength range of 120 nm to 80 nm [A⁺02a],[A⁺02b]. With an upgraded photo injector and an increased electron beam energy (up to 1 GeV) wavelengths down to 6 nm will be achievable in the future. During the commissioning phase of the VUV-FEL the emphasis was on lasing with a wavelength of 30 nm.

The VUV-FEL consists of a laser driven photocathode RF gun, five accelerator modules (ACC1 to ACC5) each having eight superconducting 9-cell niobium cavities with a resonance frequency of 1.3 GHz, two magnetic chicane bunch compressors (BC2 and BC3⁵), and an undulator section composed of six 4.5 m long undulator segments. Two additional accelerator modules (ACC6 and ACC7) can be

installed at a later stage. The total length of the linac is about 250 m. A schematic layout is shown in Fig. 1.2.

The RF gun generates bunch trains with a nominal charge of 1 nC per bunch. The maximum length of the bunch train is 800 μ s and the bunch spacing is 1 μ s (1 MHz). A 9 MHz operation is in preparation. The repetition rate of the bunch trains is 1 to 10 Hz.

In the first bunch compressor BC2, where the beam energy is about 130 MeV, the initial bunch length (about 2 mm) can be reduced by a factor of eight. The second bunch compressor (BC3) can reduce the bunch length by an additional factor of five [Stu04]. During the first commissioning phase the electron beam has been compressed mainly in the first bunch compressor.

The electron energy for a FEL wavelength of 30 nm amounts to 450 MeV. This energy is achieved using reduced gradients in the accelerator modules. In order to reach the minimum photon wavelength of 6 nm a beam energy of 1 GeV, a peak current of 2500 A, and a normalized transverse emittance of less than 2 mm mrad are needed.

The commissioning of the new facility started in the beginning of 2004. First lasing with a wavelength of 32 nm was achieved in January 2005.

² Vacuum ultra-violet free electron laser

³ linear accelerator

⁴ TeV Energy Superconducting Linear Accelerator

⁵ To be compatible with the TTF1 nomenclature, the numeration begins with two.

2 Linear beam dynamics and beam parameters

In this chapter, we give an introduction to linear beam dynamics and consider parameters and concepts required for emittance calculations. Furthermore, we will introduce different definitions of the emittance.

2.1 Transfer matrix formalism

In this section, we introduce the transfer matrix formalism, which allows the description of the movement of particles along the beam line in a simple way. A more detailed discussion can be found in [Wie03a], [RS93], or [Bro82].

The motion of a particle in the accelerator can be characterized in canonical phase space by a six-dimensional canonical vector $\tilde{\mathbf{X}} = (\mathbf{x}, \mathbf{p})$ with the spatial coordinates $\mathbf{x} = (x, y, s)$ and the momentum vector $\mathbf{p} = (p_x, p_y, p_s)$. Here x and y denote the transverse displacement from the design orbit and s is the coordinate along the reference orbit. Instead of the canonical phase space, it is common in accelerator physics to use the geometrical coordinates \mathbf{X} . In this geometrical phase space, also called *trace space*, the coordinates describing the particle motion are

$$\mathbf{X}(s) = \begin{pmatrix} x \\ x' \\ y \\ y' \\ l \\ \delta \end{pmatrix}, \quad (2.1)$$

where x and y denote the horizontal and vertical displacement from the reference orbit, and l is the longitudinal displacement from the reference particle. The coordinates $x' = dx/ds$ and $y' = dy/ds$ describe the horizontal and the vertical slopes with respect to the reference trajectory, $\delta = \Delta p/p$ is the relative momentum deviation from the reference momentum. If the momentum of the particles is constant also these coordinates are canonically conjugated.

A sketch of the coordinate system is shown in Fig. 2.1. This coordinate system is orthogonal, right-handed (x, y, s) , and it follows the reference particle along the design orbit.

In order to guide a beam of charged particles through a beam line and to change the particle energy we make use of the Lorentz force (SI-system)

$$\mathbf{F} = q(\mathbf{E} + \mathbf{v} \times \mathbf{B}), \quad (2.2)$$

where q is the charge of the particle, \mathbf{v} its velocity, and \mathbf{E} and \mathbf{B} are the electric and magnetic field vectors. Electric fields are used to accelerate the particles, while magnetic fields are used to deflect and to focus the beam. In the following, we will concentrate on the effect of magnetic fields on the particle motion.

Since the equation of motion for a charged particle under the influence of an arbitrary distribution of electromagnetic fields cannot be solved explicitly, some simplifications and restrictions have to be used in order to derive mathematical tools to describe the motion of particles in the accelerator.

If the beam line consists only of drift spaces, dipole, and quadrupole magnets, the magnetic fields depend linearly on the deviation of the particle from the reference path.

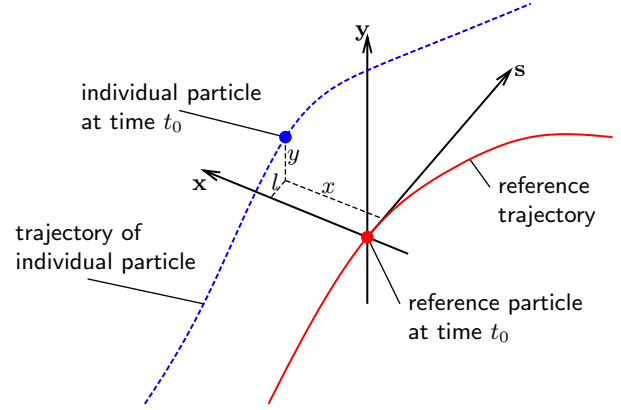


Figure 2.1: Accelerator coordinate system

Then the equations of horizontal and vertical motion can be written by

$$u''(s) + K_u(s)u(s) = \frac{\delta}{\rho_u(s)}, \quad (2.3)$$

where $u(s)$ stands for $x(s)$, $y(s)$, respectively. The parameter $\rho_u(s)$ denotes the bending radius of the reference trajectory at the position s and $K_u(s)$ is defined as

$$\begin{aligned} K_x(s) &= -k(s) + \frac{1}{\rho_x^2(s)} \\ K_y(s) &= k(s) + \frac{1}{\rho_y^2(s)} \end{aligned} \quad \text{with } k(s) = \frac{qg(s)}{p}. \quad (2.4)$$

Here $g(s)$ is the gradient of the magnetic field in the quadrupole. For the magnets, the so called *hard-edge model* is used: we assume that the magnetic field starts and ends abruptly at the beginning and end of the magnet and that the field gradient is constant inside the magnet.

Inside a quadrupole the left hand side of Eq. (2.3) simplifies to the form of a harmonic oscillator. The principal solutions of this homogeneous equation are

$$\begin{aligned} \left. \begin{aligned} C_u(s) &= \cos(\sqrt{K_u} s) \\ S_u(s) &= \frac{1}{\sqrt{K_u}} \sin(\sqrt{K_u} s) \end{aligned} \right\} \quad \text{for } K_u > 0 \\ \left. \begin{aligned} C_u(s) &= \cosh(\sqrt{K_u} s) \\ S_u(s) &= \frac{1}{\sqrt{K_u}} \sinh(\sqrt{K_u} s) \end{aligned} \right\} \quad \text{for } K_u < 0. \end{aligned} \quad (2.5)$$

Together with a particular solution u_i of the inhomogeneous equation we can formulate the general solution of Eq. (2.3) as

$$\begin{aligned} u(s) &= u_0 C_u(s) + u'_0 S_u(s) + \delta \eta_u(s) \\ u'(s) &= u_0 C'_u(s) + u'_0 S'_u(s) + \delta \eta'_u(s) \end{aligned} \quad (2.6)$$

with

$$\eta_u(s) = \frac{u_i}{\delta}.$$

The terms $\delta \eta_u(s)$ and $\delta \eta'_u(s)$ describe the momentum dependent part of the motion and the function $\eta_u(s)$ is called the *dispersion function*. The constants u_0 and u'_0 are the initial parameters of the particle trajectory. It can be shown

that the dependence of the dispersion trajectory $\eta_u(s)$ on $C_u(s)$ and $S_u(s)$ has the following form [RS93]:

$$\eta_u(s) = \eta_{u_0} C_u(s) + \eta'_{u_0} S_u(s) + S_u(s) \int_{s_0}^s \frac{1}{\rho(\tau)} C_u(\tau) d\tau - C_u(s) \int_{s_0}^s \frac{1}{\rho(\tau)} S_u(\tau) d\tau, \quad (2.7)$$

where η_{u_0} and η'_{u_0} denote the initial conditions of the dispersion function. Equation (2.7) states that outside of bending magnets the dispersion function propagates like any other particle trajectory and therefore, outside of bending magnets we cannot distinguish the motion caused by dispersion from the 'normal' particle motion.

The longitudinal displacement l of an arbitrary particle with respect to the reference particle transforms according to [Bro82]

$$l = x_0 \underbrace{\int_{s_0}^s \frac{C_x(\tau)}{\rho_x(\tau)} d\tau}_{R_{51}} + x'_0 \underbrace{\int_{s_0}^s \frac{S_x(\tau)}{\rho_x(\tau)} d\tau}_{R_{52}} + y_0 \underbrace{\int_{s_0}^s \frac{C_y(\tau)}{\rho_y(\tau)} d\tau}_{R_{53}} + y'_0 \underbrace{\int_{s_0}^s \frac{S_y(\tau)}{\rho_y(\tau)} d\tau}_{R_{54}} + \delta R_{56} + l_0, \quad (2.8)$$

where l_0 denotes the initial longitudinal deviation from the reference particle. The matrix element R_{56} is defined as the change of the orbit length ΔL divided by the relative momentum deviation of the particle:

$$R_{56} = \frac{\Delta L}{\delta} = \int_{s_0}^s \frac{\eta_x(\tau)}{\rho_x(\tau)} d\tau + \int_{s_0}^s \frac{\eta_y(\tau)}{\rho_y(\tau)} d\tau. \quad (2.9)$$

Equations (2.6) and (2.8) can be combined to a matrix equation

$$\begin{pmatrix} x \\ x' \\ y \\ y' \\ l \\ \delta \end{pmatrix} = \underbrace{\begin{pmatrix} R_{11} & R_{12} & R_{13} & R_{14} & R_{15} & R_{16} \\ R_{21} & R_{22} & R_{23} & R_{24} & R_{25} & R_{26} \\ R_{31} & R_{32} & R_{33} & R_{34} & R_{35} & R_{36} \\ R_{41} & R_{42} & R_{43} & R_{44} & R_{45} & R_{46} \\ R_{51} & R_{52} & R_{53} & R_{54} & R_{55} & R_{56} \\ R_{61} & R_{62} & R_{63} & R_{64} & R_{65} & R_{66} \end{pmatrix}}_{\mathbf{R}} \begin{pmatrix} x_0 \\ x'_0 \\ y_0 \\ y'_0 \\ l_0 \\ \delta_0 \end{pmatrix}, \quad (2.10)$$

where the transfer matrix \mathbf{R} is

$$\mathbf{R} = \begin{pmatrix} C_x & S_x & 0 & 0 & 0 & R_{16} \\ C'_x & S'_x & 0 & 0 & 0 & R_{26} \\ 0 & 0 & C_y & S_y & 0 & R_{36} \\ 0 & 0 & C'_y & S'_y & 0 & R_{46} \\ R_{51} & R_{52} & R_{53} & R_{54} & R_{55} & R_{56} \\ 0 & 0 & 0 & 0 & 0 & 1 \end{pmatrix}. \quad (2.11)$$

The matrix elements R_{16} and R_{36} characterize the dispersion, and the elements R_{26} and R_{46} represent the angular dispersion generated by the magnet described by the transfer matrix \mathbf{R} in the x -, y -plane, respectively:

$$\begin{aligned} R_{16} &= S_x(s) \int_{s_0}^s \frac{1}{\rho(\tau)} C_x(\tau) d\tau - C_x(s) \int_{s_0}^s \frac{1}{\rho(\tau)} S_x(\tau) d\tau \\ R_{26} &= S'_x(s) \int_{s_0}^s \frac{1}{\rho(\tau)} C_x(\tau) d\tau - C'_x(s) \int_{s_0}^s \frac{1}{\rho(\tau)} S_x(\tau) d\tau \\ R_{36} &= S_y(s) \int_{s_0}^s \frac{1}{\rho(\tau)} C_y(\tau) d\tau - C_y(s) \int_{s_0}^s \frac{1}{\rho(\tau)} S_y(\tau) d\tau \\ R_{46} &= S'_y(s) \int_{s_0}^s \frac{1}{\rho(\tau)} C_y(\tau) d\tau - C'_y(s) \int_{s_0}^s \frac{1}{\rho(\tau)} S_y(\tau) d\tau. \end{aligned} \quad (2.12)$$

Using Eq. (2.10) we can calculate the transformation of the vector \mathbf{X} through the entire beam line by simple multiplications of the transfer matrices \mathbf{R}_j ($j = 1, \dots, n$) corresponding to the different elements in the beam line

$$\mathbf{X}_f = \mathbf{R}_n \cdot \mathbf{R}_{n-1} \cdot \dots \cdot \mathbf{R}_1 \cdot \mathbf{X}_i, \quad (2.13)$$

where the subscripts i and f denote the initial and final position, respectively. The transfer matrices of the most common beam line elements can be found in Appendix A.

2.2 Liouville's theorem

We can use Eq. (2.13) to track the trajectory of each particle of the beam through the beam line. However, since a typical beam consists of a large number of particles¹, it would be practical to describe the motion of many particles in phase space. *Liouville's theorem* provides a powerful tool to do this. Let us consider a system with the general set of coordinates $(q_1(t), \dots, q_N(t), p_1(t), \dots, p_N(t))$. Conservative systems can be described using the Hamiltonian $H(q_1, \dots, q_N, p_1, \dots, p_N, t)$. The Hamilton equations are [Wie03b]

$$\dot{q}_i = \frac{\partial H}{\partial p_i} \quad \dot{p}_i = -\frac{\partial H}{\partial q_i}, \quad (2.14)$$

where \dot{q} is the derivative of q with respect to the time t .

Let $\Psi(q_1, \dots, q_N, p_1, \dots, p_N, t)$ be the phase space density at the time t . The total derivative of Ψ with respect to t is given by

$$\begin{aligned} \frac{d\Psi}{dt} &= \frac{\partial \Psi}{\partial t} + \sum_i \frac{\partial \Psi}{\partial q_i} \frac{\partial q_i}{\partial t} + \sum_i \frac{\partial \Psi}{\partial p_i} \frac{\partial p_i}{\partial t} \\ &= \frac{\partial \Psi}{\partial t} + \sum_i \dot{q}_i \frac{\partial \Psi}{\partial q_i} + \sum_i \dot{p}_i \frac{\partial \Psi}{\partial p_i}. \end{aligned} \quad (2.15)$$

Using the equation of continuity

$$\frac{\partial \Psi}{\partial t} + \nabla \cdot (\Psi \mathbf{v}) = 0 \quad (2.16)$$

with $\mathbf{v} = (\dot{q}_1, \dots, \dot{q}_N, \dot{p}_1, \dots, \dot{p}_N)$ it can be shown that the total time derivative of Ψ vanishes:

$$\begin{aligned} 0 &= \frac{\partial \Psi}{\partial t} + \sum_i \dot{q}_i \frac{\partial \Psi}{\partial q_i} + \sum_i \dot{p}_i \frac{\partial \Psi}{\partial p_i} + \Psi \sum_i \left(\frac{\partial \dot{q}_i}{\partial q_i} + \frac{\partial \dot{p}_i}{\partial p_i} \right) \\ &= \frac{\partial \Psi}{\partial t} + \sum_i \dot{q}_i \frac{\partial \Psi}{\partial q_i} + \sum_i \dot{p}_i \frac{\partial \Psi}{\partial p_i} \\ &\quad + \Psi \sum_i \underbrace{\left(\frac{\partial}{\partial q_i} \frac{\partial H}{\partial p_i} - \frac{\partial}{\partial p_i} \frac{\partial H}{\partial q_i} \right)}_{=0}. \end{aligned}$$

This is Liouville's theorem. It states that the phase space density in the vicinity of an arbitrary particle stays constant under the influence of conservative forces.

According to [Wie03a] the volume V of a phase space element transforms as

$$V_f = \det \mathbf{R} \cdot V_i, \quad (2.17)$$

where V_i and V_f are the initial and final volume, and \mathbf{R} denotes the transfer matrix introduced above. Due to Liouville's theorem, this volume stays constant, and we obtain the important result

$$\det \mathbf{R} = 1. \quad (2.18)$$

This is only valid if the coordinates defined in Eq. (2.1) are canonically conjugated, i.e. if the particle momentum is kept constant.

¹ A beam at the VUV-FEL with 1 nC charge consists of about $6 \cdot 10^9$ electrons.

2.3 Two-dimensional phase space ellipse

Thanks to Liouville's theorem the knowledge of the phase space area occupied by particles at a certain position in the beam line is sufficient to determine the occupied phase space area at any other position in the beam line. In accelerator physics a fraction of particles is commonly enclosed by a so-called *phase space ellipse*.

In the following we will only consider the horizontal motion but all equations are equivalent for the vertical motion.

For particles with the momentum deviation $\delta = 0$ the equation of the horizontal motion (2.3) simplifies to

$$x''(s) + K_x(s)x(s) = 0. \quad (2.19)$$

The general solution of this equation is [Wie03a]

$$x(s) = a\sqrt{\beta_x(s)}\cos(\psi_x(s) - \psi_{x_0}), \quad (2.20)$$

where a and the phase ψ_{x_0} are constants, and the phase function $\psi_x(s)$ is given by

$$\psi_x(s) = \int_0^s \frac{d\bar{s}}{\beta_x(\bar{s})}. \quad (2.21)$$

The *beta function* $\beta_x(s)$ has to fulfil the differential equation

$$\frac{1}{2}\beta_x(s)\beta_x''(s) - \frac{1}{4}\beta_x'^2(s) + K_x(s)\beta_x^2(s) = 1. \quad (2.22)$$

Equation (2.20) and its derivative

$$x'(s) = \frac{a\beta_x'(s)}{2\sqrt{\beta_x(s)}}\cos(\psi_x(s) - \psi_{x_0}) - \frac{a}{\sqrt{\beta_x(s)}}\sin(\psi_x(s) - \psi_{x_0}) \quad (2.23)$$

can be combined to the invariant of motion a^2

$$\left(\frac{1 + \frac{\beta_x'^2(s)}{4}}{\beta_x(s)}\right)x^2(s) - \beta_x'(s)x(s)x'(s) + \beta_x(s)x'^2(s) = a^2, \quad (2.24)$$

called *Courant-Snyder invariant*. With the abbreviations

$$\alpha_x(s) = -\frac{1}{2}\beta_x'(s) \quad \text{and} \quad \gamma_x(s) = (1 + \alpha_x(s)^2)/\beta_x(s) \quad (2.25)$$

Eq. (2.24) simplifies to

$$\gamma_x(s)x^2(s) + 2\alpha_x(s)x(s)x'(s) + \beta_x(s)x'^2(s) = a^2. \quad (2.26)$$

This is the equation of an ellipse. The ellipse parameter functions $\alpha_x(s)$, $\beta_x(s)$, and $\gamma_x(s)$, called *betatron functions* or *Twiss parameters*, determine the shape and the orientation of the ellipse. The motion of a particle described by Eq. (2.19) is called *betatron motion*, and the area enclosed by the ellipse is given by πa^2 .

We see that a single particle, whose motion is described by Eq. (2.19), moves along the contour of an ellipse given by Eq. (2.26). The ellipse changes its form when moving through the accelerator, but its area stays constant. This also means that the ellipse describing the motion of a second particle with a smaller betatron amplitude always stays within the phase space ellipse of the first particle.

If we consider only the transverse motion described by Eq. (2.19), the transfer matrix given by Eq. (2.11) simplifies to a 2×2 -matrix such that the transformation is given by

$$\begin{pmatrix} x \\ x' \end{pmatrix} = \begin{pmatrix} R_{11} & R_{12} \\ R_{21} & R_{22} \end{pmatrix} \begin{pmatrix} x_0 \\ x'_0 \end{pmatrix}. \quad (2.27)$$

Using Eq. (2.20) and its derivative with respect to s , we can express the trajectory of a particle in terms of the β -function, its derivative, and the phase function. By writing this in a matrix form we obtain the transfer matrix from the position s_0 to s

$$\mathbf{R} = \begin{pmatrix} \sqrt{\frac{\beta_x(s)}{\beta_x(s_0)}}(\cos\Phi_{s_0s} + \alpha_x(s_0)\sin\Phi_{s_0s}) \\ \frac{\alpha_x(s_0) - \alpha_x(s)}{\sqrt{\beta_x(s)\beta_x(s_0)}}\cos\Phi_{s_0s} - \frac{1 + \alpha_x(s)\alpha_x(s_0)}{\sqrt{\beta_x(s)\beta_x(s_0)}}\sin\Phi_{s_0s} \\ \sqrt{\beta_x(s)\beta_x(s_0)}\sin\Phi_{s_0s} \\ \sqrt{\frac{\beta_x(s_0)}{\beta_x(s)}}(\cos\Phi_{s_0s} - \alpha_x(s)\sin\Phi_{s_0s}) \end{pmatrix}, \quad (2.28)$$

which is equivalent to the matrix \mathbf{R} in Eq. (2.27). Here the *phase advance* Φ_{s_0s} from the position s_0 to s is given by

$$\Phi_{s_0s} = \psi_x(s) - \psi_x(s_0). \quad (2.29)$$

The transformation of the phase space ellipse through the beam line can be calculated using Eq. (2.27) which provides the transformation of x_0 and x'_0 from the position s_0 to s . Substituting the two transformation formulas of Eq. (2.27) for x_0 and x'_0 into Eq. (2.26) and using $\det \mathbf{R} = 1$ yields

$$\begin{pmatrix} \beta_x(s) \\ \alpha_x(s) \\ \gamma_x(s) \end{pmatrix} = \begin{pmatrix} R_{11}^2 & -2R_{11}R_{12} & R_{12}^2 \\ -R_{11}R_{21} & R_{12}R_{21} + R_{11}R_{22} & -R_{12}R_{22} \\ R_{21}^2 & -2R_{21}R_{22} & R_{22}^2 \end{pmatrix} \begin{pmatrix} \beta_x(s_0) \\ \alpha_x(s_0) \\ \gamma_x(s_0) \end{pmatrix}. \quad (2.30)$$

Now, knowing the transfer matrix from the initial position s_0 to the final position s , we can transform the Twiss parameters through the beamline.

Up to now, we have only considered the motion of a single particle within phase space. Let us now assume an entire bunch of particles, whose trajectories fill a certain area in the (x, x') -phase space. As we have seen above, when we surround an ensemble of particles by a phase space ellipse, all particles within this ellipse always remain inside of it while moving through the accelerator. Only the shape of this ellipse changes while its area stays constant.

The area A of this ellipse, enclosing a certain fraction² of particles in phase space, divided by π , is called *horizontal emittance* ϵ_x

$$\epsilon_x = \frac{A}{\pi}. \quad (2.31)$$

Since we have considered, so far, only the betatron motion and no dispersion, we will indicate this using the expression *pure betatron emittance* instead of horizontal emittance [MMSS91].

Figure 2.2 shows the phase space ellipse

$$\gamma_x x^2 + 2\alpha_x x x' + \beta_x x'^2 = \epsilon_x \quad (2.32)$$

indicating also the relations between the ellipse and the Twiss parameters.

2.4 Beam matrix

The equation of the phase space ellipse can be written in a different way by introducing the symmetric two-dimensional *beam matrix* σ :

$$(x \ x') \begin{pmatrix} \sigma_{11} & \sigma_{12} \\ \sigma_{21} & \sigma_{22} \end{pmatrix}^{-1} \begin{pmatrix} x \\ x' \end{pmatrix} = 1. \quad (2.33)$$

Since $\sigma_{21} = \sigma_{12}$ this can be written by

$$\sigma_{22}x^2 - 2\sigma_{12}xx' + \sigma_{11}x'^2 = \det\sigma, \quad (2.34)$$

² There are different conventions how the enclosed fraction of particles is determined. We will introduce a statistical definition of the emittance in Section 2.5.

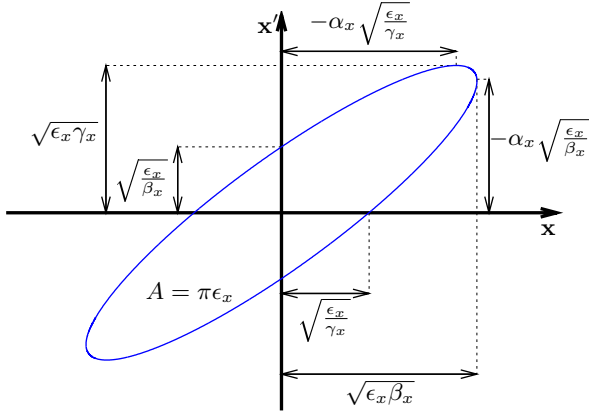


Figure 2.2: Phase space ellipse in the horizontal plane and meaning of the Twiss parameters.

and comparison with Eq. (2.32) yields the following relations between the Twiss parameters, the (pure betatron) emittance, and the beam matrix:

$$\sigma = \begin{pmatrix} \sigma_{11} & \sigma_{12} \\ \sigma_{12} & \sigma_{22} \end{pmatrix} = \epsilon_x \begin{pmatrix} \beta_x & -\alpha_x \\ -\alpha_x & \gamma_x \end{pmatrix} \quad (2.35)$$

$$\epsilon_x = \sqrt{\det \sigma} = \sqrt{\sigma_{11}\sigma_{22} - \sigma_{12}^2}. \quad (2.36)$$

This concept can be generalized from two-dimensional to n -dimensional phase space. Instead of an ellipse, the particles are enclosed by an n -dimensional hyper-ellipsoid. The equation for such a hyper-ellipsoid is given by [Wie03a]

$$\mathbf{X}_{nD}^T \sigma^{nD-1} \mathbf{X}_{nD} = 1, \quad (2.37)$$

where σ^{nD} is the symmetric $n \times n$ -beam matrix and \mathbf{X}_{nD} denotes an n -dimensional coordinate vector.

The volume of this n -dimensional hyper-ellipsoid can be expressed by

$$V_n = g_n \sqrt{\det \sigma^{nD}} \quad \text{with} \quad g_n = \frac{\pi^{n/2}}{\Gamma(1 + n/2)}, \quad (2.38)$$

and an n -dimensional emittance can then be defined³ as $\epsilon^{nD} = \sqrt{\det \sigma^{nD}}$.

In our case, a six-dimensional space is sufficient to describe the motion of the particles. The coordinate vector is in this case defined by Eq. (2.1).

The transformation of the beam matrix from the position s_0 to s can be calculated using the identities $\mathbf{I} = \mathbf{R}^{-1} \mathbf{R} = \mathbf{R}^T \mathbf{R}^{T-1}$ in Eq. (2.37)

$$\begin{aligned} \mathbf{X}_0^T \mathbf{R}^T \mathbf{R}^{T-1} \sigma_0^{-1} \mathbf{R}^{-1} \mathbf{R} \mathbf{X}_0 &= 1 \\ (\mathbf{R} \mathbf{X}_0)^T (\mathbf{R} \sigma_0 \mathbf{R}^T)^{-1} \mathbf{R} \mathbf{X}_0 &= 1 \\ \mathbf{X}^T (\mathbf{R} \sigma_0 \mathbf{R}^T)^{-1} \mathbf{X} &= 1, \end{aligned}$$

and therefore, the beam matrix at the position s is

$$\sigma = \mathbf{R} \sigma_0 \mathbf{R}^T, \quad (2.39)$$

where \mathbf{R} is the transfer matrix from position s_0 to s .

³ There are different conventions to define the emittance, e.g. the volume of the hyper-ellipsoid is defined as emittance instead of the volume divided by g_n .

2.5 Statistical definition of the beam matrix

The definition of the beam matrix has a certain degree of arbitrariness. For example, the hyper-ellipsoid enclosing the particles can contain almost all particles of the beam or only a certain fraction of them. Also the size, shape, and orientation of the hyper-ellipsoid is not yet well defined. Therefore, we need to define statistical beam parameters which uniquely specify the hyper-ellipsoid.

This can be done using the *second moments* $\langle uv \rangle$ of the beam distribution. They are defined by [MZ03]

$$\langle uv \rangle = \frac{\int_{-\infty}^{\infty} (u - \langle u \rangle)(v - \langle v \rangle) \Psi(x, x', y, y', l, \delta) dx dx' dy dy' dl d\delta}{\int_{-\infty}^{\infty} \Psi(x, x', y, y', l, \delta) dx dx' dy dy' dl d\delta}, \quad (2.40)$$

where $\langle u \rangle$ denotes the *first moment* of the variable u :

$$\langle u \rangle = \frac{\int_{-\infty}^{\infty} u \Psi(x, x', y, y', l, \delta) dx dx' dy dy' dl d\delta}{\int_{-\infty}^{\infty} \Psi(x, x', y, y', l, \delta) dx dx' dy dy' dl d\delta}. \quad (2.41)$$

Here u and v may be x, x', y, y', l, δ , and Ψ represents the intensity distribution of the beam in six-dimensional phase space. The second moments $\langle x^2 \rangle$ and $\langle y^2 \rangle$ are the variances of the beam distribution in the horizontal and vertical plane. The square root of these variances defines the rms beam sizes in the corresponding plane, i.e. $x_{\text{rms}} = \sqrt{\langle x^2 \rangle}$ and $y_{\text{rms}} = \sqrt{\langle y^2 \rangle}$.

Using these moments, the beam matrix can be written as

$$\begin{aligned} \sigma^{6D} &= \begin{pmatrix} \langle x^2 \rangle & \langle xx' \rangle & \langle xy \rangle & \langle xy' \rangle & \langle xl \rangle & \langle x\delta \rangle \\ \langle xx' \rangle & \langle x'^2 \rangle & \langle x'y \rangle & \langle x'y' \rangle & \langle x'l \rangle & \langle x'\delta \rangle \\ \langle xy \rangle & \langle x'y \rangle & \langle y^2 \rangle & \langle yy' \rangle & \langle yl \rangle & \langle y\delta \rangle \\ \langle xy' \rangle & \langle x'y' \rangle & \langle yy' \rangle & \langle y'^2 \rangle & \langle y'l \rangle & \langle y'\delta \rangle \\ \langle xl \rangle & \langle x'l \rangle & \langle yl \rangle & \langle y'l \rangle & \langle l^2 \rangle & \langle l\delta \rangle \\ \langle x\delta \rangle & \langle x'\delta \rangle & \langle y\delta \rangle & \langle y'\delta \rangle & \langle l\delta \rangle & \langle \delta^2 \rangle \end{pmatrix} \\ &= \begin{pmatrix} \sigma_{xx} & \sigma_{xy} & \sigma_{xl} \\ \sigma_{xy}^T & \sigma_{yy} & \sigma_{yl} \\ \sigma_{xl}^T & \sigma_{yl}^T & \sigma_{ll} \end{pmatrix}, \end{aligned} \quad (2.42)$$

where $\sigma_{xx}, \sigma_{yy}, \sigma_{ll}, \sigma_{xy}, \sigma_{xl}$ and σ_{yl} are 2×2 -matrices, e.g.

$$\sigma_{xx} = \begin{pmatrix} \langle x^2 \rangle & \langle xx' \rangle \\ \langle xx' \rangle & \langle x'^2 \rangle \end{pmatrix}. \quad (2.43)$$

In the following, we will always use this statistical definition of the beam matrix.

The statistical emittance is commonly used for electron accelerators. If we consider a two-dimensional Gaussian phase space distribution in the (x, x') -plane and only consider the (2D) emittance defined by Eq. (2.36), the ellipse determined by the second moments encloses about 39% of the particles in the beam (1σ emittance). At proton accelerators traditionally the 2σ emittance is quoted.

2.6 Different definitions of the transverse beam emittance

Let us assume the six-dimensional beam matrix is known. Then $\epsilon_{\text{rms}}^{6D} = \sqrt{\det \sigma^{6D}}$ denotes the six-dimensional rms beam emittance.

The projection of the six-dimensional hyper-ellipsoid onto the transverse planes yields a 4×4 -beam matrix, which

describes the dimensions of the projected beam in transverse phase space

$$\sigma^{4D} = \begin{pmatrix} \sigma_{xx} & \sigma_{xy} \\ \sigma_{xy}^T & \sigma_{yy} \end{pmatrix}, \quad (2.44)$$

where σ_{xx} , σ_{yy} , and σ_{xy} are 2×2 -matrices as defined above. In the following, we always mean this projection when we refer to the emittance, except where it is specifically indicated.

When dispersion is present, the second beam moments consist of two contributions. The first derives from the betatron motion and the second is due to dispersion. When separating these two parts, we can express σ^{4D} as

$$\sigma^{4D} = \begin{pmatrix} \langle x_\beta^2 \rangle + \eta_x^2 \langle \delta^2 \rangle & \langle x_\beta x'_\beta \rangle + \eta_x \eta'_x \langle \delta^2 \rangle \\ \langle x_\beta x'_\beta \rangle + \eta_x \eta'_x \langle \delta^2 \rangle & \langle x'^2_\beta \rangle + \eta'^2_x \langle \delta^2 \rangle \\ \langle x_\beta y_\beta \rangle + \eta_x \eta_y \langle \delta^2 \rangle & \langle x'_\beta y_\beta \rangle + \eta'_x \eta_y \langle \delta^2 \rangle \\ \langle x_\beta y_\beta \rangle + \eta_x \eta_y \langle \delta^2 \rangle & \langle x'_\beta y'_\beta \rangle + \eta'_x \eta'_y \langle \delta^2 \rangle \\ \langle x_\beta y_\beta \rangle + \eta_x \eta_y \langle \delta^2 \rangle & \langle x_\beta y'_\beta \rangle + \eta_x \eta'_y \langle \delta^2 \rangle \\ \langle x'_\beta y \rangle + \eta'_x \eta_y \langle \delta^2 \rangle & \langle x'_\beta y'_\beta \rangle + \eta'_x \eta'_y \langle \delta^2 \rangle \\ \langle y^2_\beta \rangle + \eta_y^2 \langle \delta^2 \rangle & \langle y_\beta y'_\beta \rangle + \eta_y \eta'_y \langle \delta^2 \rangle \\ \langle y_\beta y'_\beta \rangle + \eta_y \eta'_y \langle \delta^2 \rangle & \langle y'^2_\beta \rangle + \eta_y'^2 \langle \delta^2 \rangle \end{pmatrix}, \quad (2.45)$$

where the horizontal dispersion function $\eta_x = \eta_x(s)$ and the horizontal angular dispersion function $\eta'_x = \eta'_x(s)$ statistically are defined by

$$\begin{aligned} \eta_x(s) &= \frac{\langle x(s)\delta \rangle}{\langle \delta^2 \rangle} \\ \eta'_x(s) &= \frac{\langle x'(s)\delta \rangle}{\langle \delta^2 \rangle}. \end{aligned} \quad (2.46)$$

The corresponding functions in the vertical plane are equivalent.

The emittance $\epsilon_{\text{rms}}^{4D} = \sqrt{\det \sigma^{4D}}$, where σ^{4D} is given by Eq. (2.45), is called *effective* projected four-dimensional transverse rms emittance. The pure betatron emittance can be calculated by subtracting the contribution due to dispersion from each element in the beam matrix. If the dispersion vanishes, $\epsilon_{\text{rms}}^{4D}$ reduces to the pure betatron emittance.

Typically, we are interested in the two-dimensional transverse emittance. Also in this case, we can distinguish the effective emittance including the dispersion contribution from the pure betatron emittance.

When we use Eq. (2.35) to calculate the Twiss parameters in the presence of dispersion, we have to first subtract the dispersion contribution from the second moments. Otherwise, the Twiss parameters do not describe the betatron motion, but instead describe the superposition of the betatron motion and the dispersion. One may call these η -dependent Twiss parameters *effective* Twiss parameters. They are defined by [MMSS91]

$$\begin{aligned} \sigma_{11} &= \beta_x \epsilon_{x,\text{rms}} \\ \sigma_{12} &= -\alpha_x \epsilon_{x,\text{rms}} \\ \sigma_{22} &= \gamma_x \epsilon_{x,\text{rms}}. \end{aligned} \quad (2.47)$$

If the dispersion terms are zero, the effective Twiss parameters reduce to the ones of the pure betatron motion.

Besides the dispersion, a coupling of the horizontal and vertical betatron oscillations is possible, caused for example by skew quadrupoles or by solenoidal fields. This is described by σ_{xy} . If all the elements of σ_{xy} are equal to zero, the beam is transversely uncoupled. In presence of coupling it is possible to define *projected* (2D) emittances in the horizontal and vertical plane. They are the square

root of the determinant of the on-diagonal 2×2 -matrices of σ^{4D}

$$\begin{aligned} \epsilon_{x,\text{rms}} &= \sqrt{\det \sigma_{xx}} \\ \epsilon_{y,\text{rms}} &= \sqrt{\det \sigma_{yy}}. \end{aligned} \quad (2.48)$$

Coupling between the (x, x') - and (y, y') -plane means that the principle axes of the (4D) hyper-ellipsoid are rotated with respect to the (x, x') - and (y, y') -planes. Using a symplectic transformation [Kub99], a new coordinate system, in which the beam matrix is diagonalized, can be introduced [WE00],[BL01]

$$U^T \sigma^{4D} U = \begin{pmatrix} \epsilon_{1,\text{rms}} & 0 & 0 & 0 \\ 0 & \epsilon_{1,\text{rms}} & 0 & 0 \\ 0 & 0 & \epsilon_{2,\text{rms}} & 0 \\ 0 & 0 & 0 & \epsilon_{2,\text{rms}} \end{pmatrix}, \quad (2.49)$$

where $\epsilon_{1,\text{rms}}$ and $\epsilon_{2,\text{rms}}$ are the *intrinsic* rms emittances, describing the phase space distribution in the new coordinate system. More details of the symplectic transformation and the transformation matrix U can be found in Appendix B. It can be shown that the product of the intrinsic emittances cannot be larger than the product of $\epsilon_{x,\text{rms}}$ and $\epsilon_{y,\text{rms}}$ [Buo93]:

$$\epsilon_{\text{rms}}^{4D} = \epsilon_{1,\text{rms}} \epsilon_{2,\text{rms}} \leq \epsilon_{x,\text{rms}} \epsilon_{y,\text{rms}}. \quad (2.50)$$

The two-dimensional transverse emittances ϵ_x and ϵ_y are called *geometrical* emittances, since they are defined with geometric coordinates. The geometrical emittance is preserved only if there is no coupling in the beam line lattice, the particle energy is constant, and stochastic effects can be neglected.

If the beam energy is increased, the transverse coordinates (x, x') and (y, y') are no longer canonically conjugated variables. However, according to Liouville's theorem, the phase space density is preserved in the canonical coordinates (x, p_x) and (y, p_y) . During acceleration, only the longitudinal momentum p_s increases while the transverse momenta p_x and p_y stay constant. Therefore, the slopes $x' = p_x/p_s$ and $y' = p_y/p_s$ decrease proportionally to $1/p$, where p is the momentum of the beam. The decrease of the geometric emittance with increasing beam energy is called *adiabatic damping*.

When we multiply the geometric emittance by the factor p/m_0c we get a new quantity called the *normalized* emittance

$$\epsilon_N = \frac{p}{m_0c} \epsilon. \quad (2.51)$$

The normalized emittance stays constant also during acceleration of the particles, in absence of coupling in the beam lattice and of stochastic effects.

3 Determination of the transverse emittance

In order to calculate the emittance, we need to reconstruct the beam matrix. Since we know the transformation of the beam matrix from an initial position s_0 to another position s_i , we can reconstruct the entire transverse beam matrix σ^{4D} from measurements and linear transformations of the second moments $\langle x^2 \rangle$, $\langle y^2 \rangle$, and $\langle xy \rangle$ of the beam distribution. For the reconstruction of the projected (2D) emittances, it is sufficient to measure $\langle x^2 \rangle$ and $\langle y^2 \rangle$ after different linear transformations.

The linear transformation from the fixed position s_0 to the position s_i is described by the transfer matrix $\mathbf{R}^{(i)}$. A change in this transformation can be achieved by two different approaches. The first is to keep s_i fixed while changing the optics in between the position s_0 and s_i . This can be done by changing the gradient of quadrupoles in between s_0 and s_i (*quadrupole scan*). The second possibility is to use fixed optics in the accelerator and to change the position s_i where the measurement of the second moments is performed. Combinations of these two approaches are possible.

The measurements presented in this thesis are performed using the fixed optics approach. However, the formalism presented in this chapter is valid also for quadrupole scans.

We can reconstruct the beam matrix from the second moments, but we do not obtain information about the phase space density distribution. This information can be obtained with tomographic reconstruction methods. They offer the possibility to determine the phase space density distribution from projections measured on different planes.

3.1 Determination of the (2D) emittance

Emittance measurements at the VUV-FEL are performed in special diagnostic sections. In these sections, the matrix elements $R_{16}^{(i)}$ and $R_{36}^{(i)}$ vanish, since there are no bending magnets. We will describe the equations only in the horizontal plane. Considerations in the vertical plane are equivalent.

According to Eq. (2.39) for vanishing $R_{16}^{(i)}$ elements, the second moment $\langle x^2 \rangle$ is transformed by

$$\langle x_{(i)}^2 \rangle = R_{11}^{(i)2} \langle x_0^2 \rangle + R_{12}^{(i)2} \langle x_0'^2 \rangle + 2R_{11}^{(i)} R_{12}^{(i)} \langle x_0 x_0' \rangle. \quad (3.1)$$

The knowledge of $\langle x_{(i)}^2 \rangle$, i.e. the square of the rms beam size, after three different transformations described by $\mathbf{R}^{(i)}$ gives the possibility to determine the three different beam matrix elements of σ_x :

$$\begin{pmatrix} \langle x_{(1)}^2 \rangle \\ \langle x_{(2)}^2 \rangle \\ \langle x_{(3)}^2 \rangle \end{pmatrix} = \underbrace{\begin{pmatrix} R_{11}^{(1)2} & 2R_{11}^{(1)} R_{12}^{(1)} & R_{12}^{(1)2} \\ R_{11}^{(2)2} & 2R_{11}^{(2)} R_{12}^{(2)} & R_{12}^{(2)2} \\ R_{11}^{(3)2} & 2R_{11}^{(3)} R_{12}^{(3)} & R_{12}^{(3)2} \end{pmatrix}}_{\mathbf{A}} \begin{pmatrix} \langle x_0^2 \rangle \\ \langle x_0 x_0' \rangle \\ \langle x_0'^2 \rangle \end{pmatrix} \quad (3.2)$$

$$\begin{pmatrix} \langle x_0^2 \rangle \\ \langle x_0 x_0' \rangle \\ \langle x_0'^2 \rangle \end{pmatrix} = \mathbf{A}^{-1} \begin{pmatrix} \langle x_{(1)}^2 \rangle \\ \langle x_{(2)}^2 \rangle \\ \langle x_{(3)}^2 \rangle \end{pmatrix} \quad (3.3)$$

The (2D effective) rms emittance is given by Eq. (2.48):

$$\epsilon_{x,\text{rms}} = \sqrt{\langle x_0^2 \rangle \langle x_0'^2 \rangle - \langle x_0 x_0' \rangle^2} \quad (3.4)$$

Using Eq. (2.47) the (effective) Twiss parameters are

$$\begin{pmatrix} \beta_{x_0} \\ \alpha_{x_0} \\ \gamma_{x_0} \end{pmatrix} = \begin{pmatrix} \langle x_0^2 \rangle / \epsilon_{x,\text{rms}} \\ -\langle x_0 x_0' \rangle / \epsilon_{x,\text{rms}} \\ \langle x_0'^2 \rangle / \epsilon_{x,\text{rms}} \end{pmatrix}. \quad (3.5)$$

We see that we cannot determine the dispersion and therefore, we can only calculate the effective emittance, containing the contribution of the dispersion.

For measurements of the pure betatron emittance either the dispersion function $\eta(s)$ and the energy spread $\langle \delta^2 \rangle$ must be known, or the emittance measurements must be performed in a section with bending magnets where the $R_{16}^{(i)}$ elements do not vanish. In the latter case, the transformation for the second moment $\langle x^2 \rangle$ is given by

$$\begin{aligned} \langle x^2 \rangle = & R_{11}^{(i)2} \langle x_0^2 \rangle + R_{12}^{(i)2} \langle x_0'^2 \rangle + 2R_{11}^{(i)} R_{12}^{(i)} \langle x_0 x_0' \rangle \\ & + 2R_{11}^{(i)} R_{16}^{(i)} \langle x_0 \delta_0 \rangle + 2R_{12}^{(i)} R_{16}^{(i)} \langle x_0' \delta_0 \rangle + R_{16}^{(i)2} \langle \delta_0^2 \rangle, \end{aligned} \quad (3.6)$$

and the six beam matrix elements in Eq. (3.6) can be obtained from measurements of $\langle x^2 \rangle$ with six different transfer matrices $\mathbf{R}^{(i)}$. This also yields the dispersion and the energy spread. However, this method is not possible in the VUV-FEL diagnostic sections.

3.2 Fitting of the measured data

In order to be less sensitive to measurement errors, it is preferable to measure $\langle x_{(i)}^2 \rangle$ for more than three different transformations and then to find a solution for the beam matrix elements which has the highest likelihood of representing the measured data. This can be done using the chi-square (χ^2)-method, which is described in [PTVF93]. An application for emittance measurements can be found in [HC04] and [MZ03].

According to the χ^2 -method the best estimates for the second moments $\langle x_{(i)}^2 \rangle$ are obtained by minimizing the expression

$$\chi^2 = \sum_{i=1}^n \left[\frac{\langle x_{(i)}^2 \rangle - f_i(\langle x_0^2 \rangle, \langle x_0 x_0' \rangle, \langle x_0'^2 \rangle)}{\sigma_{\langle x_{(i)}^2 \rangle}} \right]^2. \quad (3.7)$$

Here n is the number of measurements, $\sigma_{\langle x_{(i)}^2 \rangle}$ denotes the error of $\langle x_{(i)}^2 \rangle$ and

$$\begin{aligned} f_i(\langle x_0^2 \rangle, \langle x_0 x_0' \rangle, \langle x_0'^2 \rangle) = & R_{11}^{(i)2} \langle x_0^2 \rangle + 2R_{11}^{(i)} R_{12}^{(i)} \langle x_0 x_0' \rangle \\ & + R_{12}^{(i)2} \langle x_0'^2 \rangle. \end{aligned} \quad (3.8)$$

Equation (3.7) can be written in a compact form by introducing the matrix

$$\mathbf{B} = \begin{pmatrix} \frac{R_{11}^{(1)2}}{\sigma_{\langle x_{(1)}^2 \rangle}} & \frac{2R_{11}^{(1)} R_{12}^{(1)}}{\sigma_{\langle x_{(1)}^2 \rangle}} & \frac{R_{12}^{(1)2}}{\sigma_{\langle x_{(1)}^2 \rangle}} \\ \frac{R_{11}^{(2)2}}{\sigma_{\langle x_{(2)}^2 \rangle}} & \frac{2R_{11}^{(2)} R_{12}^{(2)}}{\sigma_{\langle x_{(2)}^2 \rangle}} & \frac{R_{12}^{(2)2}}{\sigma_{\langle x_{(2)}^2 \rangle}} \\ \vdots & \vdots & \vdots \\ \frac{R_{11}^{(n)2}}{\sigma_{\langle x_{(n)}^2 \rangle}} & \frac{2R_{11}^{(n)} R_{12}^{(n)}}{\sigma_{\langle x_{(n)}^2 \rangle}} & \frac{R_{12}^{(n)2}}{\sigma_{\langle x_{(n)}^2 \rangle}} \end{pmatrix} \quad (3.9)$$

and the vectors

$$\mathbf{a} = \begin{pmatrix} \langle x_0^2 \rangle \\ \langle x_0 x_0' \rangle \\ \langle x_0'^2 \rangle \end{pmatrix} \quad \text{and} \quad \mathbf{b} = \begin{pmatrix} \frac{\langle x_{(1)}^2 \rangle}{\sigma_{\langle x_{(1)}^2 \rangle}} \\ \frac{\langle x_{(2)}^2 \rangle}{\sigma_{\langle x_{(2)}^2 \rangle}} \\ \vdots \\ \frac{\langle x_{(n)}^2 \rangle}{\sigma_{\langle x_{(n)}^2 \rangle}} \end{pmatrix}. \quad (3.10)$$

With these definitions Eq. (3.7) can be expressed by

$$\chi^2 = \sum_{i=1}^n \left[b_i - \sum_{j=1}^3 B_{ij} a_j \right]^2. \quad (3.11)$$

To find the minimum of χ^2 the derivatives with respect to the parameters a_1 , a_2 , and a_3 have to vanish:

$$\begin{pmatrix} \partial\chi^2/\partial a_1 \\ \partial\chi^2/\partial a_2 \\ \partial\chi^2/\partial a_3 \end{pmatrix} = 2 \begin{pmatrix} \sum_{i=1}^n \sum_{j=1}^3 B_{ij} B_{i1} a_j \\ \sum_{i=1}^n \sum_{j=1}^3 B_{ij} B_{i2} a_j \\ \sum_{i=1}^n \sum_{j=1}^3 B_{ij} B_{i3} a_j \end{pmatrix} - 2 \begin{pmatrix} \sum_{i=1}^n b_i B_{i1} \\ \sum_{i=1}^n b_i B_{i2} \\ \sum_{i=1}^n b_i B_{i3} \end{pmatrix} = \begin{pmatrix} 0 \\ 0 \\ 0 \end{pmatrix}. \quad (3.12)$$

These vectors can be written as a matrix product such that Eq. (3.12) simplifies to

$$\mathbf{B}^T \mathbf{b} = (\mathbf{B}^T \mathbf{B}) \mathbf{a}. \quad (3.13)$$

Multiplying both sides of Eq. (3.13) from the left side with $(\mathbf{B}^T \mathbf{B})^{-1}$ yields the searched parameter vector

$$\mathbf{a} = (\mathbf{B}^T \mathbf{B})^{-1} \mathbf{B}^T \mathbf{b}. \quad (3.14)$$

3.3 Error estimation of the fitted parameters

The squared error of a function $g(x_1, x_2, \dots, x_n)$ can be determined by error propagation as

$$\sigma_g^2 = \sum_{i=1}^n \left(\frac{\partial g}{\partial x_i} \right)^2 \sigma_{x_i}^2 + \sum_{i=1}^n \sum_{j=1, j \neq i}^n \frac{\partial g}{\partial x_i} \frac{\partial g}{\partial x_j} \text{cov}(i, j). \quad (3.15)$$

The first sum represents the variance of the function g , the second sum is the contribution of the covariances.

We are interested in the errors of the beam matrix elements as well as the errors of β_{x_0} , α_{x_0} , and ϵ_{x_0} . The last three quantities can be described by the function f :

$$\mathbf{f} = \begin{pmatrix} \beta_{x_0} \\ \alpha_{x_0} \\ \epsilon_{x_0, \text{rms}} \end{pmatrix} = \begin{pmatrix} a_1 / \sqrt{a_1 a_3 - a_2^2} \\ -a_2 \sqrt{a_1 a_3 - a_2^2} \\ \sqrt{a_1 a_3 - a_2^2} \end{pmatrix}, \quad (3.16)$$

where the parameters a_1 , a_2 , and a_3 are the components of the vector \mathbf{a} defined above. The variances and covariances of a_1 , a_2 , and a_3 are needed for the error calculation. The variance of a_k is

$$\sigma_{a_k}^2 = \sum_{i=1}^n \left(\frac{\partial a_k}{\partial \langle x_{(i)}^2 \rangle} \right)^2 \sigma_{\langle x_{(i)}^2 \rangle}^2. \quad (3.17)$$

Using Eq. (3.14) with the abbreviation $\mathbf{C} = (\mathbf{B}^T \mathbf{B})^{-1}$, we can write a_k as

$$a_k = \sum_{j=1}^3 C_{kj} [\mathbf{B}^T \mathbf{b}]_j, \quad (3.18)$$

where \mathbf{B} and \mathbf{b} are given by Eq. (3.9) and (3.10), respectively. The partial derivative of a_k with respect to $\langle x_{(i)}^2 \rangle$ is then

$$\frac{\partial a_k}{\partial \langle x_{(i)}^2 \rangle} = \frac{1}{\sigma_{\langle x_{(i)}^2 \rangle}} \sum_{j=1}^3 C_{kj} B_{ij}. \quad (3.19)$$

Inserting Eq. (3.19) in Eq. (3.17) leads to the final result for the variance of a_k :

$$\begin{aligned} \sigma_{a_k}^2 &= \sum_{i=1}^n \left(\sum_{j=1}^3 C_{kj} B_{ij} \right)^2 \\ &= \sum_{i=1}^n \sum_{j=1}^3 \sum_{l=1}^3 C_{kj} C_{kl} B_{ij} B_{il} \\ &= \sum_{j=1}^3 \sum_{l=1}^3 C_{kj} C_{kl} \underbrace{\sum_{i=1}^n B_{ij} B_{il}}_{[\mathbf{B}^T \mathbf{B}]_{jl} = [\mathbf{C}^{-1}]_{lj}} \end{aligned} \quad (3.20)$$

$$= \sum_{j=1}^3 C_{kj} \sum_{l=1}^3 C_{kl} [\mathbf{C}^{-1}]_{lj} \quad (3.21)$$

$$= C_{kk}. \quad (3.22)$$

In Eq. (3.20) we have used the fact that matrix $\mathbf{B}^T \mathbf{B}$ is symmetrical, and Eq. (3.21) has been simplified using the definition of the inverse of a matrix:

$$D_{ij} = [\mathbf{C} \mathbf{C}^{-1}]_{ij} = \sum_{l=1}^3 C_{il} [\mathbf{C}^{-1}]_{lj} = \begin{cases} 0 & \forall i \neq j \\ 1 & \forall i = j \end{cases}. \quad (3.23)$$

Equation (3.22) states that the diagonal elements of \mathbf{C} are the variances of the fitted parameters a_i . It can be shown that the off-diagonal elements C_{ij} are the covariances between a_i and a_j . By knowing matrix \mathbf{B} , we can determine $\mathbf{C} = (\mathbf{B}^T \mathbf{B})^{-1}$, whose elements are the variances and covariances of the fitted parameters a_i .

When we know the variances and covariances of the parameters a_1 , a_2 , and a_3 , we can calculate the errors of the emittance and of the Twiss parameters by applying Eq. (3.15) to Eq. (3.16). Another possibility is to calculate the error matrix containing the squared errors of the searched parameters as diagonal elements [MZ03]:

$$\sigma_f^2 = (\nabla_a \mathbf{f})^T \mathbf{C} (\nabla_a \mathbf{f}) = \begin{pmatrix} \sigma_{\beta_{x_0}}^2 & \dots & \dots \\ \dots & \sigma_{\alpha_{x_0}}^2 & \dots \\ \dots & \dots & \sigma_{\epsilon_{x_0, \text{rms}}}^2 \end{pmatrix}. \quad (3.24)$$

Both notations are equivalent. In computer codes it is often more practical to use Eq. (3.24) for the error calculation.

3.4 Determination of the intrinsic emittance

In order to calculate the intrinsic emittance we have to determine also the four coupling elements of matrix σ_{xy} in addition to the beam matrices σ_x and σ_y . The quantity that can be measured is $\langle xy_{(i)} \rangle$. The transformation of this beam matrix element for vanishing $R_{16}^{(i)}$ and $R_{36}^{(i)}$ is given as

$$\begin{aligned} \langle xy_{(i)} \rangle &= R_{11}^{(i)} R_{33}^{(i)} \langle xy_{(0)} \rangle + R_{12}^{(i)} R_{33}^{(i)} \langle x' y_{(0)} \rangle \\ &\quad + R_{34}^{(i)} R_{11}^{(i)} \langle xy'_{(0)} \rangle + R_{34}^{(i)} R_{12}^{(i)} \langle x' y'_{(0)} \rangle. \end{aligned} \quad (3.25)$$

Since there are four unknown beam matrix elements in Eq. (3.25), $\langle xy_{(i)} \rangle$ must be measured under four different transformations, described by the transfer matrices $\mathbf{R}^{(i)}$.

The solution of the searched beam matrix elements can be obtained as

$$\underbrace{\begin{pmatrix} \langle xy(1) \rangle \\ \langle xy(2) \rangle \\ \langle xy(3) \rangle \\ \langle xy(4) \rangle \end{pmatrix}}_l = \underbrace{\begin{pmatrix} R_{11}^{(1)} R_{33}^{(1)} & R_{12}^{(1)} R_{33}^{(1)} & R_{34}^{(1)} R_{11}^{(1)} & R_{34}^{(1)} R_{12}^{(1)} \\ R_{11}^{(2)} R_{33}^{(2)} & R_{12}^{(2)} R_{33}^{(2)} & R_{34}^{(2)} R_{11}^{(2)} & R_{34}^{(2)} R_{12}^{(2)} \\ R_{11}^{(3)} R_{33}^{(3)} & R_{12}^{(3)} R_{33}^{(3)} & R_{34}^{(3)} R_{11}^{(3)} & R_{34}^{(3)} R_{12}^{(3)} \\ R_{11}^{(4)} R_{33}^{(4)} & R_{12}^{(4)} R_{33}^{(4)} & R_{34}^{(4)} R_{11}^{(4)} & R_{34}^{(4)} R_{12}^{(4)} \end{pmatrix}}_K \underbrace{\begin{pmatrix} \langle xy(0) \rangle \\ \langle x'y(0) \rangle \\ \langle xy'(0) \rangle \\ \langle x'y'(0) \rangle \end{pmatrix}}_k \quad (3.26)$$

$$k = K^{-1}l.$$

If $\langle xy(i) \rangle$ has been measured for more than four different transfer matrices $\mathbf{R}^{(i)}$, the same procedure described above can be used to fit the parameters to the measured data.

The matrix corresponding to the matrix \mathbf{B} is

$$\mathbf{E} = \begin{pmatrix} \frac{R_{11}^{(1)} R_{33}^{(1)}}{\sigma_{\langle xy(1) \rangle}} & \frac{R_{12}^{(1)} R_{33}^{(1)}}{\sigma_{\langle xy(1) \rangle}} & \frac{R_{34}^{(1)} R_{11}^{(1)}}{\sigma_{\langle xy(1) \rangle}} & \frac{R_{34}^{(1)} R_{12}^{(1)}}{\sigma_{\langle xy(1) \rangle}} \\ \frac{R_{11}^{(2)} R_{33}^{(2)}}{\sigma_{\langle xy(2) \rangle}} & \frac{R_{12}^{(2)} R_{33}^{(2)}}{\sigma_{\langle xy(2) \rangle}} & \frac{R_{34}^{(2)} R_{11}^{(2)}}{\sigma_{\langle xy(2) \rangle}} & \frac{R_{34}^{(2)} R_{12}^{(2)}}{\sigma_{\langle xy(2) \rangle}} \\ \vdots & \vdots & \vdots & \vdots \\ \frac{R_{11}^{(n)} R_{33}^{(n)}}{\sigma_{\langle xy(n) \rangle}} & \frac{R_{12}^{(n)} R_{33}^{(n)}}{\sigma_{\langle xy(n) \rangle}} & \frac{R_{34}^{(n)} R_{11}^{(n)}}{\sigma_{\langle xy(n) \rangle}} & \frac{R_{34}^{(n)} R_{12}^{(n)}}{\sigma_{\langle xy(n) \rangle}} \end{pmatrix} \quad (3.27)$$

and instead of the vector \mathbf{b} , we use

$$\mathbf{e} = \begin{pmatrix} \langle xy(1) \rangle \\ \sigma_{\langle xy(1) \rangle} \\ \langle xy(2) \rangle \\ \sigma_{\langle xy(2) \rangle} \\ \vdots \\ \langle xy(n) \rangle \\ \sigma_{\langle xy(n) \rangle} \end{pmatrix}. \quad (3.28)$$

The beam matrix elements of σ_{xy} can then be obtained from

$$l = (\mathbf{E}^T \mathbf{E})^{-1} \mathbf{E}^T \mathbf{e}, \quad (3.29)$$

and the error matrix corresponding to the matrix \mathbf{C} with the variances of the fitted parameters as diagonal elements is

$$\mathbf{F} = (\mathbf{E}^T \mathbf{E})^{-1}. \quad (3.30)$$

Since all elements of the transverse beam matrix σ^{4D} are now known, we can calculate the intrinsic emittances using Eq. (2.49).

3.5 Tomographic phase space reconstruction

By using the second moments, we can determine the emittance and the area occupied by the particles in phase space. This method does, however, not provide information about the density distribution within phase space. This information is often of special interest for tuning and operation of the accelerator.

The emittance is very sensitive to tails in the phase space density distribution. A small fraction of particles in these tails can cause a significant increase of the emittance. The knowledge of the phase space density distribution offers the possibility to calculate the emittance of the beam core (*core emittance*) by neglecting a certain fraction (e.g. 10%) of particles in the tails. Such a core emittance characterizes the main part of the beam while being much less sensitive to small changes in the phase space distribution.

Tomographic reconstruction algorithms offer the possibility to reconstruct multi-dimensional density distributions from measurements of different projections of these distributions. Most algorithms need a large number of different projections for this reconstruction. The Maximum Entropy (MENT) Algorithm provides a reconstruction of

the searched distribution with a minimal amount of artefacts from only a few projections. A detailed description of the MENT Algorithm and of the computer code used in this thesis can be found in [Sch04a]. This method is also described in [Mot85], and for the four dimensional case in [MSJ81].

In the following it is assumed that there is no coupling between the (x, x') -, (y, y') -, and (l, δ) -planes. The considerations described here are valid for quadrupole scans as well as for fixed optics measurements.

As seen above, the horizontal motion in absence of coupling is described by

$$\begin{pmatrix} x \\ x' \end{pmatrix} = \begin{pmatrix} R_{11} & R_{12} \\ R_{21} & R_{22} \end{pmatrix} \begin{pmatrix} x_0 \\ x'_0 \end{pmatrix}. \quad (3.31)$$

Let $\Psi_0(x_0, x'_0)$ be the initial density distribution of the horizontal phase space. The matrix $\mathbf{R}^{(i)}$ transforms this distribution to $\Psi_i(x, x')$. The projection $G_i(x)$ of this distribution onto the x -axis can be expressed as

$$G_i(x) = \int_{-\infty}^{\infty} \Psi_0(x_0^{(i)}(x, x'), x_0'^{(i)}(x, x')) dx', \quad (3.32)$$

and since $\det \mathbf{R}^{(i)} = 1$, Eq. (3.31) yields for the coordinates $x_0^{(i)}(x, x')$ and $x_0'^{(i)}(x, x')$

$$\begin{aligned} x_0^{(i)}(x, x') &= R_{22}^{(i)} x - R_{12}^{(i)} x' \\ x_0'^{(i)}(x, x') &= R_{11}^{(i)} x' - R_{21}^{(i)} x. \end{aligned} \quad (3.33)$$

The goal is now to invert Eq. (3.32) and to determine the initial density distribution $\Psi_0(x_0, x'_0)$. Let us assume that the projections $G_i(x)$ have been measured for n different transfer matrices $\mathbf{R}^{(i)}$. Due to the limited number of measurements, the inversion of Eq. (3.32) is not unique and therefore, many different density distributions $\Psi_0(x_0, x'_0)$ exist that reproduce all measured projections $G_i(x)$. Out of these distributions the one $\Psi_0(x_0, x'_0)$ with the largest probability is the most appropriate one.

From statistical mechanics we know that the probability of a system of N similar particles in the microscopic states $i = 1, \dots, n$ can be quantified by the *entropy* S

$$S = -k_B \sum_{i=1}^n \omega_i \ln \omega_i \quad \text{with} \quad \omega_i = \frac{M_i}{N}. \quad (3.34)$$

Here M_i is the number of particles in the microscopic state i and k_B is the Boltzmann constant. We can use the same concept to describe the probability of the phase space density distribution Ψ_0 . Instead of the discrete variable ω_i describing the fraction of particles in the state i , we use the continuous function

$$\omega(x_0, x'_0) = \frac{\Psi_0(x_0, x'_0)}{N},$$

where $N = \int_{-\infty}^{\infty} \int_{-\infty}^{\infty} \Psi_0(x_0, x'_0) dx_0 dx'_0$ is the total number of particles in the beam. The function $\omega(x_0, x'_0)$ describes the fraction of particles in the phase space area $([x_0, x_0 + dx_0], [x'_0, x'_0 + dx'_0])$. With this modification, we have to replace the sum in Eq. (3.34) by an integral. When we ignore the constants k_B and N , we get the following expression quantifying the probability of the phase space density distribution $\Psi_0(x_0, x'_0)$

$$\bar{S}(\Psi_0) = - \int_{-\infty}^{\infty} \int_{-\infty}^{\infty} \Psi_0(x_0, x'_0) \ln \Psi_0(x_0, x'_0) dx_0 dx'_0. \quad (3.35)$$

Since this quantity is proportional to the entropy of $\Psi_0(x_0, x'_0)$, it is maximum for the distribution $\Psi_0(x_0, x'_0)$ with the largest probability.

Therefore, the searched density distribution $\Psi_0(x_0, x'_0)$ maximizes Eq. (3.35) while simultaneously satisfying all constraints given by Eq. (3.32). In order to find the stationary solution of Eq. (3.35) with the constraints of Eq. (3.32), the Lagrange multiplier technique can be used. The Lagrange function for this case is

$$L(\Psi_0, \Lambda) = - \int_{-\infty}^{\infty} \int_{-\infty}^{\infty} \Psi_0(x_0, x'_0) \ln \Psi_0(x_0, x'_0) dx_0 dx'_0 + \sum_{i=1}^n \int_{-\infty}^{\infty} \left[\int_{-\infty}^{\infty} \Lambda_i(x) \left(\Psi_0(x_0^{(i)}(x, x'), x_0'^{(i)}(x, x')) dx' - G_i(x) \right) \right] dx, \quad (3.36)$$

where $\Lambda_i(x)$ denotes the n Lagrange multiplier functions. The conditions for the stationary solution are

$$\frac{\partial L(\Psi, \Lambda)}{\partial \Psi} = 0 \quad (3.37)$$

$$\frac{\partial L(\Psi, \Lambda)}{\partial \Lambda_i} = 0 \quad \text{for } i = 1, \dots, n. \quad (3.38)$$

Equation (3.38) gives

$$\int_{-\infty}^{\infty} \left[\int_{-\infty}^{\infty} \Psi_0(x_0^{(i)}(x, x'), x_0'^{(i)}(x, x')) dx' - G_i(x) \right] dx = 0$$

for $i = 1, \dots, n$, which is equivalent to the equations for the constraints defined by Eq. (3.32).

In order to find the solution for Eq. (3.38), we have to first perform a coordinate transformation in the second term of Eq. (3.36) by introducing the new coordinates (see Eq. (3.31)):

$$\begin{aligned} x^{(i)}(x_0, x'_0) &= R_{11}^{(i)} x_0 + R_{12}^{(i)} x'_0 \\ x'^{(i)}(x_0, x'_0) &= R_{21}^{(i)} x_0 + R_{22}^{(i)} x'_0. \end{aligned} \quad (3.39)$$

Since $\det \mathbf{R}^{(i)} = 1$ this yields

$$L(\Psi_0, \Lambda) = - \int_{-\infty}^{\infty} \int_{-\infty}^{\infty} \Psi_0(x_0, x'_0) \ln \Psi_0(x_0, x'_0) dx_0 dx'_0 + \sum_{i=1}^n \int_{-\infty}^{\infty} \left[\int_{-\infty}^{\infty} \Lambda_i(x^{(i)}(x_0, x'_0)) \left(\Psi_0(x_0, x'_0) dx'_0 - G_i(x^{(i)}(x_0, x'_0)) \right) \right] dx_0, \quad (3.40)$$

and Eq. (3.37) can then be expressed as

$$- \int_{-\infty}^{\infty} \int_{-\infty}^{\infty} \left[1 + \ln \Psi_0(x_0, x'_0) - \sum_{i=1}^n \Lambda_i(x^{(i)}(x_0, x'_0)) \right] dx_0 dx'_0 = 0. \quad (3.41)$$

Therefore, the condition for the stationary solution is

$$\ln \Psi_0(x_0, x'_0) = \sum_{i=1}^n \Lambda_i(x^{(i)}(x_0, x'_0)) - 1 \quad (3.42)$$

$$\Psi_0(x_0, x'_0) = \exp \left[\sum_{i=1}^n \Lambda_i(x^{(i)}(x_0, x'_0)) - 1 \right], \quad (3.43)$$

and with the definition

$$H_i(x) = \exp \left[\Lambda_i(x) - \frac{1}{n} \right] \quad (3.44)$$

the searched distribution $\Psi_0(x_0, x'_0)$ can be written as a simple product

$$\Psi_0(x_0, x'_0) = \prod_{i=1}^n H_i(x^{(i)}(x_0, x'_0)). \quad (3.45)$$

Combining Eq. (3.45) and Eq. (3.32) gives the constraint integral

$$G_i(x) = \int_{-\infty}^{\infty} \prod_{j=1}^n H_j(x^{(j)}(x_0^{(i)}, x_0'^{(i)})) dx'. \quad (3.46)$$

Reference [Min79] shows that $H_i(x)$ can always be factored out of Eq. (3.46):

$$G_i(x) = H_i(x) \int_{-\infty}^{\infty} \prod_{j \neq i}^n H_j(x^{(j)}(x_0^{(i)}, x_0'^{(i)})) dx'. \quad (3.47)$$

The last equation represents an iteration law for $H_i(x)$ which can be solved, for example, with a non-linear Gauss-Seidel algorithm (see [Sch04a]).

The power of the MENT Algorithm is shown in Fig. 3.1 for two examples: a two-dimensional distribution consisting of three Gaussian profiles of different widths and heights, and a single asymmetric Gaussian profile. In both cases the initial distributions have been transformed by using simple rotation matrices

$$\mathbf{R}_{rot}(\alpha_i) = \begin{pmatrix} \cos \alpha_i & \sin \alpha_i \\ -\sin \alpha_i & \cos \alpha_i \end{pmatrix} \quad (3.48)$$

with a rotation angle $\alpha_i = 0^\circ, 45^\circ, 90^\circ, 135^\circ$ as transfer matrices $R^{(i)}$. From these transformed distributions, the projections G_i are calculated, and used for the MENT Algorithm.

The reconstruction quality can be quantified using the mean-square deviation δ of the reconstructed solution $\Psi_{rec}(x, x')$ from the original value $\Psi_0(x, x')$ (see [Sch04a])

$$\delta_{rec} = \sqrt{\frac{\int_{-\infty}^{\infty} \int_{-\infty}^{\infty} [\Psi_{rec}(x, x') - \Psi_0(x, x')]^2 dx dx'}{\int_{-\infty}^{\infty} \int_{-\infty}^{\infty} [\Psi_{rec}(x, x')]^2 dx dx'}}. \quad (3.49)$$

In our examples in Fig. 3.1 this deviation is $\delta_{rec} = 6.62\%$ for the distribution consisting of three two-dimensional Gaussian and $\delta_{rec} = 1.23\%$ for the single two-dimensional Gaussian distribution.

We can see that the amount of reconstruction artefacts is very low even if only four projections are used. Compared to other tomographic reconstruction algorithms, like the filtered back-projection algorithm [Gei99], this is a big advantage.

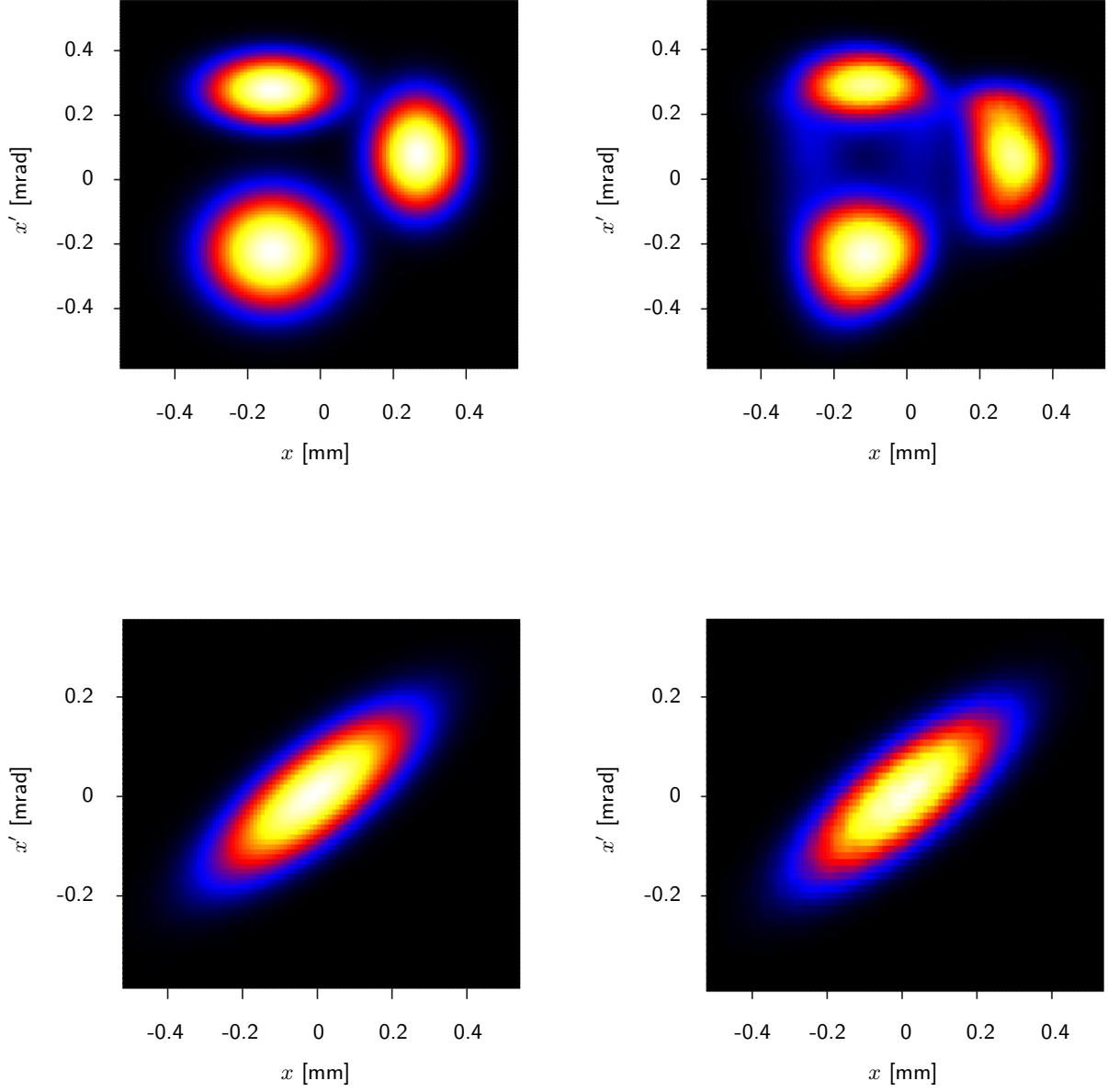


Figure 3.1: Example of MENT reconstruction from four projections G_i ($\mathbf{R}_{rot}(0^\circ, 45^\circ, 90^\circ, 135^\circ)$) for two different two-dimensional density distributions. Top: density distribution consisting of three two-dimensional Gaussian profiles of different widths. Input distribution (left) and reconstructed distribution ($\delta_{rec} = 6.62\%$) (right). Bottom: density distribution consisting of a single rotated two-dimensional Gaussian profile. Input distribution (left) and reconstructed distribution ($\delta_{rec} = 1.23\%$) (right).

4 Experimental setup

There are two sections dedicated to emittance measurements in the VUV-FEL beam line. The first one, called BC2 section, is located downstream of the first bunch compressor BC2. The second one, called SUND section, is placed directly in front of the undulator section. It is a temporary beam line reserved for the upcoming seeding undulator. The positions of the two diagnostic sections are shown in Fig. 1.2. Both sections consist of three FODO¹ cells and four OTR² stations for beam distribution measurements. In the BC2 section additional wire scanners are installed for beam profile measurements.

4.1 Injector

The injector is the key component of a low emittance accelerator. A laser driven RF photo injector is used at the VUV-FEL. The laser is a Nd:YLF-laser converted to a wavelength of 262 nm [Sch04b]. Electron bunches with a nominal charge of 1 nC are generated on a Cs₂Te cathode and accelerated in a 1.5 cell cavity operating at a frequency of 1.3 GHz (an RF gun) [Sch04b]. In order to counteract emittance growth induced by internal Coulomb forces, the electron beam is focused by a solenoid magnet (main solenoid). A second solenoid is used to reduce the magnetic field on the cathode surface to zero.

At present, the longitudinal laser pulse profile is nearly Gaussian shaped with a length of $\sigma_z = (4.4 \pm 0.1)$ ps [Sch04b]. However, in order to obtain a small transverse emittance a transversally and longitudinally flat laser pulse profile is preferred. At PITZ³ a laser pulse-shaper producing longitudinally flat laser pulses with a length of about 20 ps [K⁺04] has been tested and the measured transverse emittance has consequently been reduced by a factor of two [MAA⁺04]. A similar pulse-shaper can be installed in the VUV-FEL laser system at a later stage.

In the first accelerator module (ACC1) consisting of 8 superconducting cavities [Wei03] the beam energy is increased to about 130 MeV. To avoid strong focusing and the resulting increased space charge forces, the first four cavities are operated with a moderate gradient of 12 MV/m. The last four cavities accelerate with the full gradient (~ 20 MV/m).

The longitudinal shape of the electron bunches has been measured with a streak camera using synchrotron light from the last dipole of the bunch compressor. Without compression the bunches are longitudinally Gaussian shaped with a bunch length of $\sigma_z = (1.7 \pm 0.2)$ mm [Sch04b].

A schematic of the injector and the BC2 section is shown in Fig. 4.1.

4.2 First bunch compressor section (BC2 section)

The BC2 section is located after the first accelerator module ACC1 where the electron energy is about 130 MeV. It consists of a bunch compressor, a diagnostic section dedicated to emittance measurements, and two groups of five

magnet	magnetic length [mm]	$C_{mag} [\frac{T}{Am}]$
Q5DBC2	269.11	0.1299
Q6DBC2	270.08	0.1301
Q7DBC2	269.02	0.1299
Q8DBC2	270.26	0.1299
Q9DBC2	268.73	0.1300
Q10DBC2	269.64	0.1300

Table 4.1: Calibration constants and magnetic lengths of TQA type quadrupoles

quadrupoles, the first one upstream of the bunch compressor and the second one downstream of it (see Fig. 4.1). The quadrupoles are intended to match the beam to the design optics inside the bunch compressor and the diagnostic section.

The functional principle of a bunch compressor is indicated in Fig. 4.1: In ACC1 an energy modulation is produced by positioning the bunch on the positive slope of the fundamental harmonic RF wave in the cavities. This yields a higher energy of the particles in the bunch-tail compared to those in the bunch-head. In the bunch compressor, the path length of particles with higher energy is shorter than that of particles with a lower energy. The bunch is therefore shortened, and the compression strength can be adjusted by the phase of the RF wave in ACC1. The RF wave induces a curvature in the energy-phase plane after acceleration, which leads to a high peak current and a long tail in the longitudinal bunch structure [S⁺02a]. To compensate for this curvature a superconducting third harmonic cavity [S⁺02b] will be installed at a later stage (see Fig. 4.1).

All quadrupoles in the matching section downstream of the bunch compressor as well as the quadrupoles in the FODO cells are TQA type magnets produced by the Efremov Institute in Saint-Petersburg, Russia. The field gradient as function of the current is determined from field gradient measurements [Efr02] done at 50 A. The maximum current of the quadrupoles is 298 A. We can assume that at a current of about 10.5 A, as it is used in the diagnostic section, the field gradient depends linearly on the current:

$$g \left[\frac{T}{m} \right] = C_{mag} \cdot I [A], \quad (4.1)$$

where C_{mag} is a constant. The value of C_{mag} as well as the magnetic length L_{mag} for the magnets in the FODO cells is given in Table 4.1. In the calculation of the field gradient we have not considered remanent fields and higher-order contributions. Based on measurements of one of the TQA type magnets [Hol05], we estimate that the systematic error of the quadrupole field gradients is 6%. Appropriate cycling procedures have been applied to ensure that always the same branch of the hysteresis circles of the quadrupoles is used.

Using Eq. (4.1), we can numerically calculate the k -value (see Eq. (2.4)) of the quadrupoles as [RS93]

$$k [m^{-2}] = 0.2998 \cdot \frac{g [T/m]}{p [GeV/c]}. \quad (4.2)$$

The rest mass of the electron can be neglected for high energies, yielding $p = E/c$. Here E denotes the beam energy.

¹ A pair of focusing and defocusing quadrupoles.

² optical transition radiation

³ Photo Injector Test Facility at DESY Zeuthen

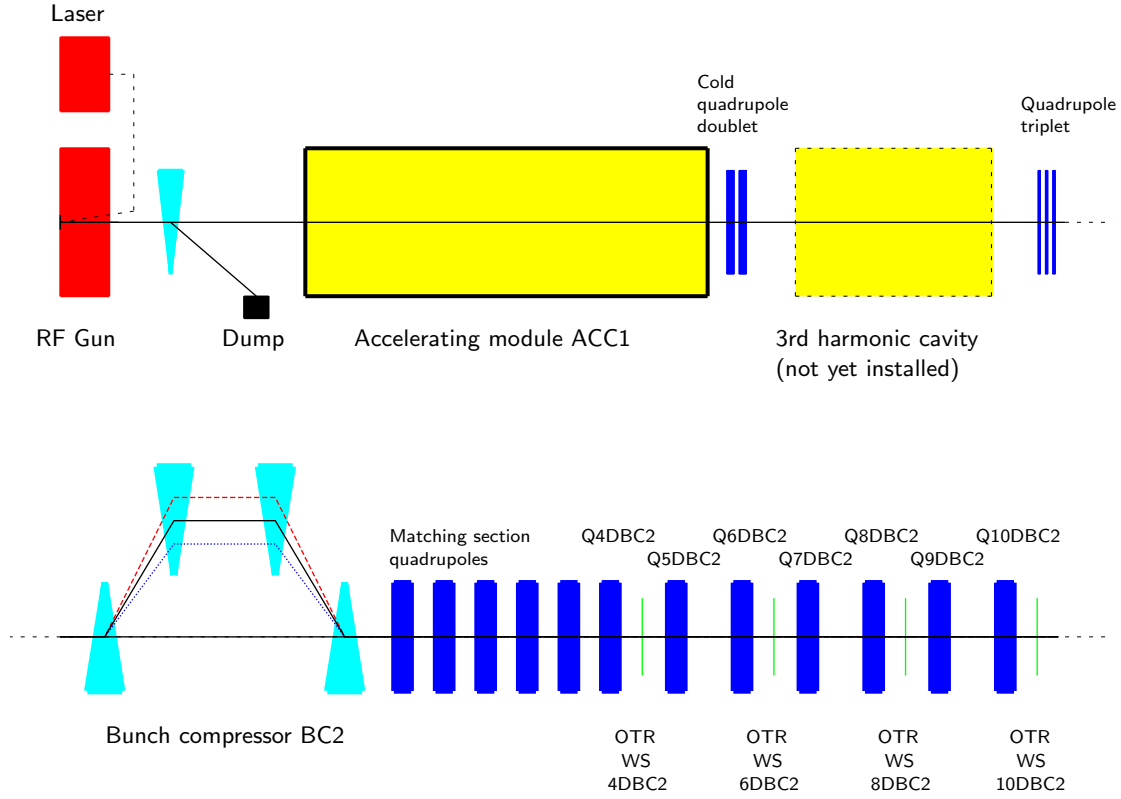


Figure 4.1: Schematic layout of the injector and the BC2 section.

The functional principle of the bunch compressor is indicated. Particles with a higher energy (dotted) are deflected less in the magnetic chicane and therefore have a shorter orbit through the chicane than the particles with lower energy (dashed). An appropriate chirp in the beam energy distribution leads to a compression of the bunch.

The quadrupoles Q4DBC2 to Q10DBC2 (see Fig. 4.1) are powered by a common power supply. The polarity for the nominal setup is chosen so that the first quadrupole after each screen is focusing in the horizontal plane and the second one is defocusing.

The three FODO cells in the diagnostic section have a length of $2L = 1.9\text{m}$, L being the distance between the centres of two successive quadrupoles. For the periodic (matched) solution the beta function has the same value in the centre of all focusing quadrupoles. This is fulfilled both in the x - and y -plane. Reference [Cas03] shows that for the setup used here the error of an emittance measurement is smallest with a phase advance of 45° inside each FODO cell. This can be understood easily, since the reconstruction of the phase space ellipse is a kind of tomography. For a phase advance of $45^\circ = 180^\circ/4$, the four projections differ from each other by the largest amount.

The periodic solution for a 45° phase advance per cell is shown in Fig. 4.2. At the positions of the screens the beta function is about 2.5m in both planes. Therefore, we expect round beams on the screens for equal (2D) emittances in both planes. The nominal Twiss parameters at the OTR screens for a phase advance of 45° are given in Table 4.2.

4.3 SUND diagnostic section

The SUND diagnostic section is located directly in front of the first undulator at a position, where at a later stage a seeding undulator can be installed. It consists of three FODO cells, a matching section with five quadrupoles, and four OTR screens. A fifth screen is available in front of the FODO lattice, between the two last quadrupoles of the

	BC2 (45°)	SUND (45°)	SUND (76.5°)
$\beta_{x,D}$ [m]	2.47	11.91	7.64
$\alpha_{x,D}$	-1.19	1.12	1.32
$\beta_{y,D}$ [m]	2.51	11.67	7.36
$\alpha_{y,D}$	1.21	-1.10	-1.28

Table 4.2: Twiss parameters for matched optics in the BC2 and SUND diagnostic sections at the OTR screens in the FODO lattice. The phase advance in the FODO cells is indicated in brackets.

matching section. Since these quadrupoles are used for the matching inside the FODO lattice, the phase advance between this screen and the others can be varied. A sketch of the diagnostic section is given in Fig. 4.3. The length of the FODO cells is $2L = 8.9802\text{m}$, where L is the distance between the centres of the quadrupoles. The quadrupoles used in the matching section and in the FODO cells are of the same type as those in the BC2 section (TQA).

During commissioning, a phase advance of 76.5° instead of 45° was used. The Twiss parameters for matched optics with 76.5° and 45° phase advance in the FODO cells are given in Table 4.2. The periodic solution for 76.5° phase advance is presented in Fig. 4.4.

4.4 OTR monitors

The transverse beam distribution is measured with imaging devices based on *optical transition radiation* (OTR). We give a short summary of the main properties of the optical transition radiation and describe the OTR monitors.

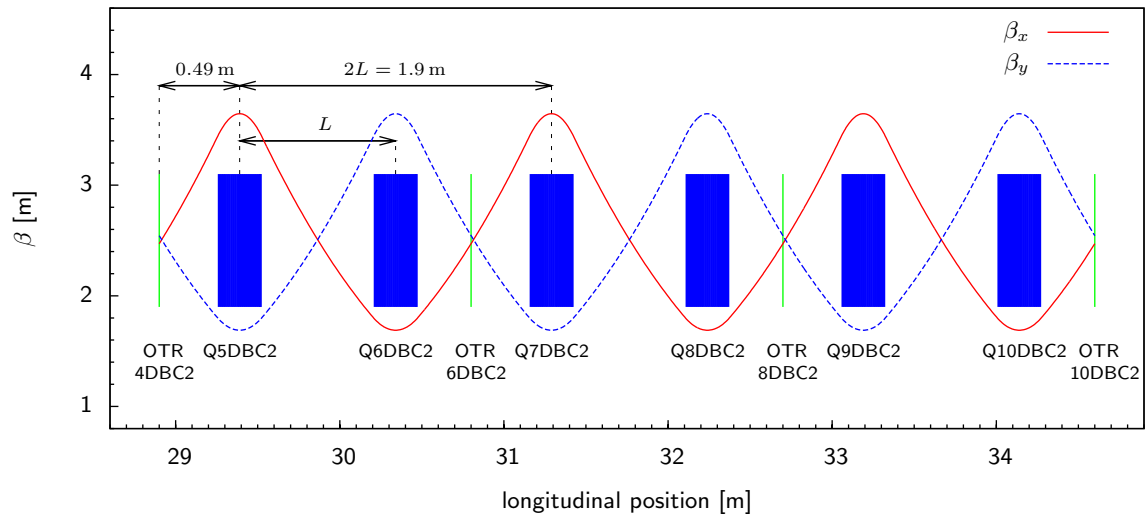


Figure 4.2: Periodic solution for the beta functions in the BC2 diagnostic section with a phase advance of 45° in each FODO cell.

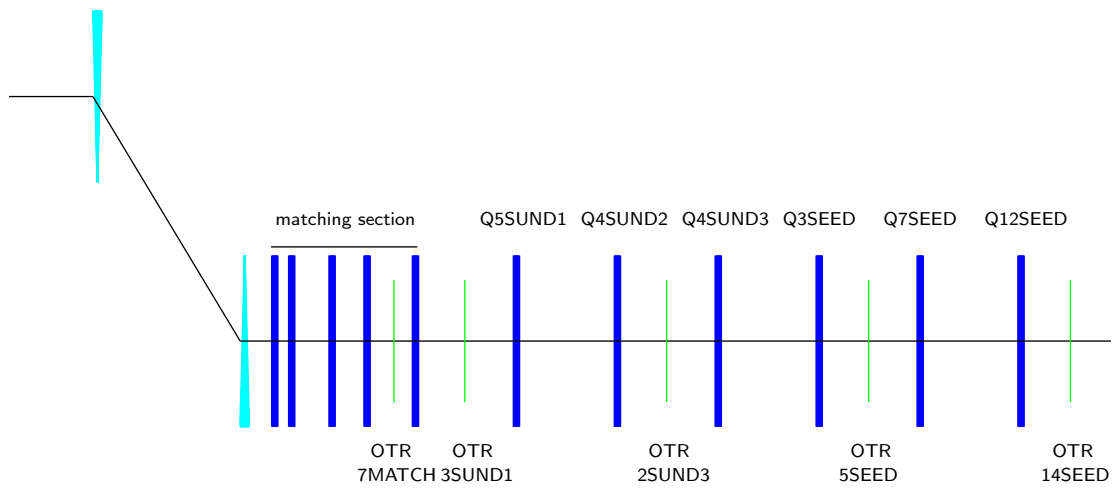


Figure 4.3: Schematic layout of the SUND diagnostic section.

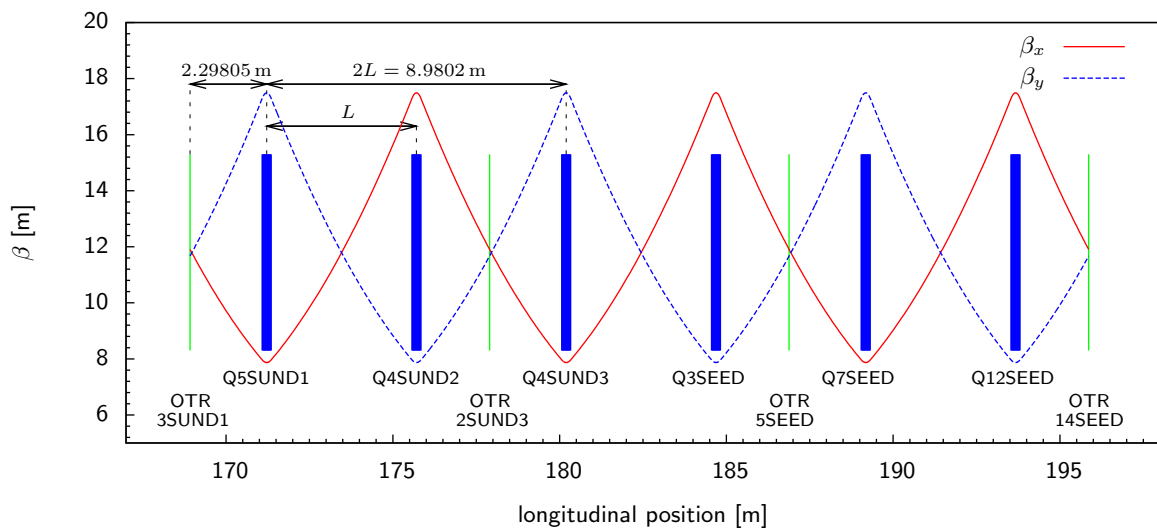


Figure 4.4: Periodic solution for the beta functions in the SUND FODO lattice with a phase advance of 76.5° in each FODO cell.

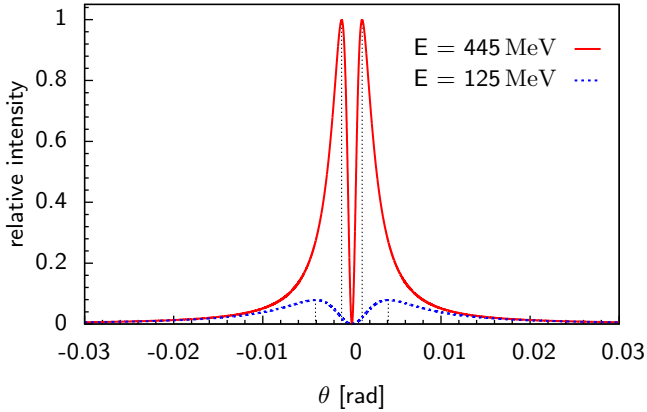


Figure 4.5: Angular distribution of the transition radiation for an electron crossing a metallic foil with an energy of $E = 125$ MeV and $E = 445$ MeV, respectively. The angle θ is defined with respect to the direction of specular reflection (backward radiation) or to the particle trajectory (forward radiation).

4.4.1 Optical transition radiation

Whenever a charged particle crosses a boundary between two media with different dielectric properties, *transition radiation* is emitted. This was first predicted by Ginzburg and Frank in 1945 [GF45]. The transition radiation is emitted in the forward and backward direction with respect to the boundary surface.

Assuming a perfectly reflecting metallic surface, the emitted energy per solid-angle $d\Omega$ and per frequency-interval $d\omega$ by a single electron can be approximated by a simple expression [Gei99]

$$I(\theta, \omega) = \frac{d^2W}{d\omega d\Omega} \approx \frac{e^2}{4\pi^3\epsilon_0 c} \frac{\beta^2 \sin^2 \theta}{(1 - \beta^2 \cos^2 \theta)^2}. \quad (4.3)$$

The angle θ is defined with respect to the direction of specular reflection for the backward radiation and with respect to the particle trajectory for the forward radiation (see Fig. 4.6). At ultra relativistic energies, the angular distribution given by Eq. (4.3) is symmetric with a peak of the angular distribution at

$$\theta_{max} = \frac{1}{\gamma_{rel}}. \quad (4.4)$$

Figure 4.5 shows the angular distribution for electrons with two different energies (125 MeV and 445 MeV).

Optical transition radiation is the part of the transition radiation with wavelengths in the visible spectrum (≈ 400 nm to 800 nm). Since the angular distribution does not depend on the wavelength of the radiation in this range, OTR can be used for beam distribution measurements without the necessity of frequency-dependent corrections.

4.4.2 OTR monitors

For the beam distribution measurements we use screens mounted with an angle of 45° with respect to the design orbit. The backward transition radiation is emitted at an angle of 90° with respect to the design orbit and, therefore, it is easy to guide it out of the beam pipe through a window (see Fig. 4.6). By imaging this radiation onto a CCD camera we obtain an image of the transverse density distribution of the beam. The OTR phenomenon is fast

(~ 0.1 ps) and by using a fast-gated camera measurements within the bunch train are possible. We, however, use normal CCD cameras that integrate the signal over the whole bunch train. Single-bunch measurements are possible with bunch trains of one bunch only. This is a big advantage compared to wire scanners, especially when there is a jitter in the electron beam orbit. In addition, not only the beam profiles can be measured, but the projected transverse beam distribution information is available. This is especially useful for the calculation of the coupling elements $\langle xy \rangle$ in the beam matrix.

The VUV-FEL OTR system has been designed and constructed in a collaboration between DESY and INFN-LNF/Roma2 (Italy). It is described in detail in [HBF⁺03] and in [CCC⁺04]. A total of 24 OTR monitors are installed along the accelerator. A sketch of a standard OTR monitor is shown in Fig. 4.7. The remotely controlled system offers the possibility to use two different screens: a $350 \mu\text{m}$ thick polished silicon screen and a polished silicon screen with a 40 nm aluminium coating. The latter has a higher reflectivity in the optical wavelengths, providing a stronger light signal. However, since the silicon screen has a higher thermal resistance, it is better suited for high charge densities. Calibration marks on the screen-holder help to calibrate the optical system.

The optical transition radiation is extracted out of the beam pipe through a fused silica window (DUV-200) [Isi] which is resistant to X-rays and provides a good transmittivity for visible wavelengths. The OTR light is reflected downwards using a mirror. This has two advantages: direct X-rays from the screen cannot reach the camera and the camera can be mounted near the floor, where the overall radiation level is lower. Three lenses can be remotely moved in or out of the optical axis of the system. Only one lens is inserted at any time. The lenses are achromats having a focal lengths of 250 mm, 200 mm, and 160 mm. They provide nominal magnifications of 1.0, 0.39, and 0.25, respectively. Three neutral density filters with transmissions of 10%, 25%, and 40% can be used to attenuate the light signal. The complete system is shielded against scattered light. The CCD camera has a lead shield to protect it against X-rays.

As CCD cameras we use Basler A301f cameras [Bas02]. They have squared pixels with a size of $9.9 \mu\text{m}$ and a dynamic range of 8 bit. These cameras offer a non-interlaced data transfer, can be triggered, and are equipped with a remote gain and shutter control. The cameras are connected using IEEE1394 (firewire) links to compact industrial personal computers located inside the accelerator tunnel. These computers are connected via local ethernet to an image server located in the control room. The image server controls the complete camera system. The camera control software, both on the image server and on the computers in the tunnel, is based on LabVIEWTM [Lab]. A detailed description of the camera read-out system can be found in [C⁺05].

Due to diffraction effects caused by the limited angular acceptance of an imaging system, the image of a point-like source is not a point anymore but a more complicated structure called *Point Spread Function* (PSF). Imperfections of the lenses cause aberrations [Wet80] which may also degrade the image. In our optical system, the effects of geometrical aberrations are reduced by using a diaphragm on the lens [HBF⁺03]. The resolution of the system has been determined by measuring the edge profile of a rectangular object on a calibration target. We can determine the rms width of the Gaussian shape PSF characterizing the

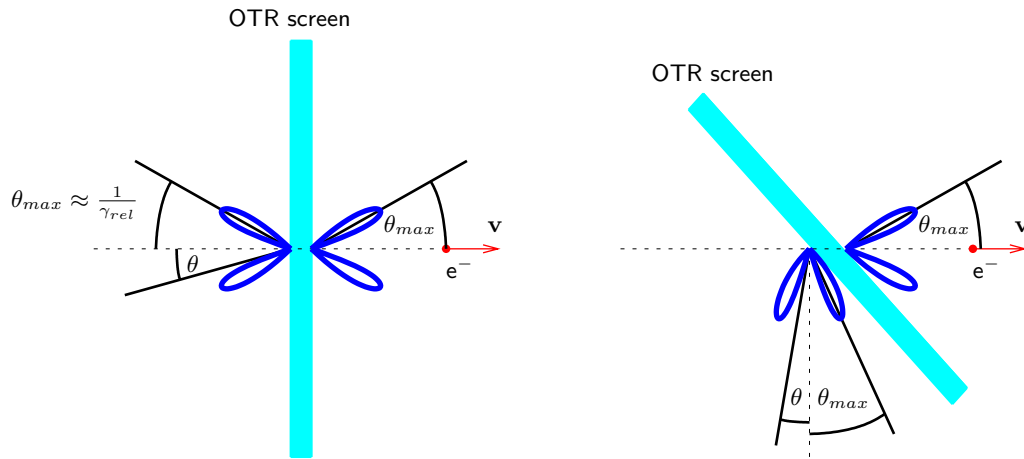


Figure 4.6: Schematic of transmitted transition radiation in forward and backward direction for normal incidence (left) and incidence under an angle of 45° (right).

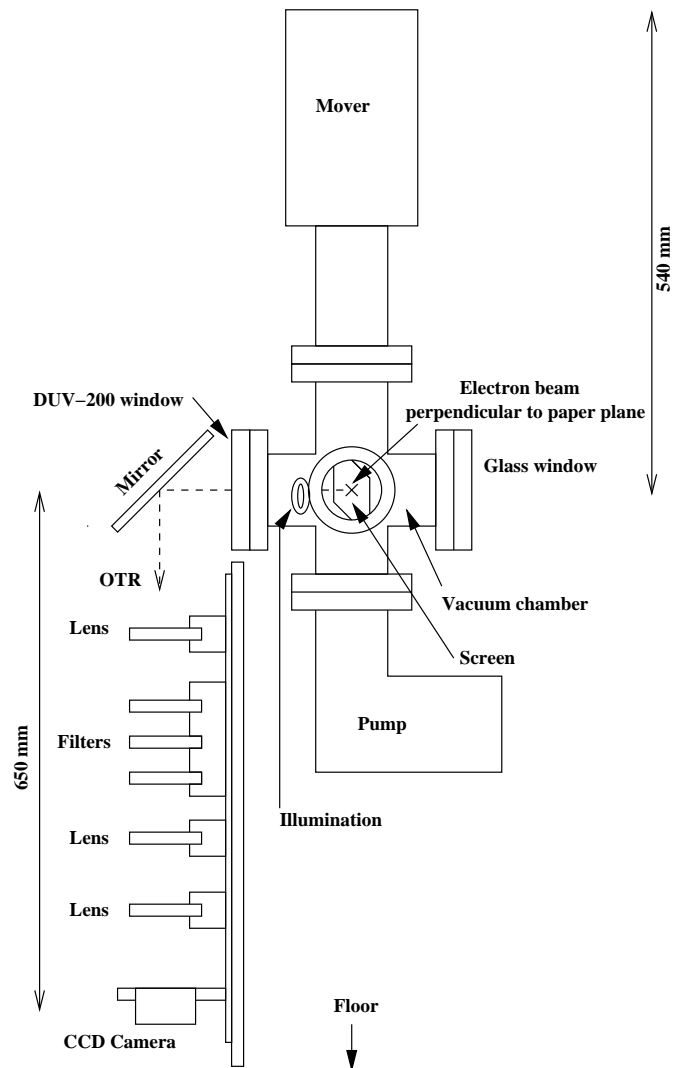


Figure 4.7: Schematic of a standard VUV-FEL OTR monitor providing three different magnifications and the possibility to use intensity filters to avoid saturated images [HBF⁺03].

4 *Experimental setup*

system from the measured profile [HBF⁺03]. The average rms-resolution measured with the highest magnification is 11 μm [CCC⁺04].

5 Systematic errors

In this chapter we analyse the dependence of the determined emittance on errors in parameters needed for the emittance calculation. We will see that the resulting error for the emittance depends sensitively on the matching of the beam inside the FODO lattice. Only the BC2 diagnostic section is discussed but the following consideration are also valid for the SUND diagnostic section, since the layout of these two sections is similar.

5.1 Mismatch parameter

The Twiss parameters in the diagnostic section are periodic only if they are matched to the design values (see Table 4.2). If they differ from these values, the beam is mismatched. A parameter ξ is commonly used to quantify the mismatch. It is defined as [MZ03]

$$\xi = \frac{1}{2}(\beta\gamma_D - 2\alpha\alpha_D + \gamma\beta_D), \quad (5.1)$$

where subscript D denotes the design values. For a matched beam the mismatch factor is $\xi = 1$.

A graphical way to represent the mismatch is to plot the design phase space ellipse given in Eq. (2.32) at a certain position in the lattice (we choose here the OTR screen 4DBC2) using normalized coordinates [MZ03]

$$\left(\frac{u}{\sqrt{\beta_{u,D}}}, \frac{\alpha_{u,D}u + \beta_{u,D}u'}{\sqrt{\beta_{u,D}}} \right) \quad \text{with} \quad u = x, y. \quad (5.2)$$

Within these coordinates the design ellipse is a circle, and we normalize it such that its radius is unity. Plotting the actual (measured) ellipse by using the same coordinates shows the degree of the mismatch. The area of the actual ellipse compared to the design ellipse shows the deviation in the emittance.

The quality of the emittance measurement can be indicated in these mismatch plots by tracking or backtracking the measured beam sizes to the position used in the plot (OTR 4DBC2). The beam sizes are plotted as lines in the graph by using the same coordinates as above. An example is given in Fig. 5.1 for two different ξ . The mismatch is induced by changing α_x on the first screen (4DBC2) according to

$$\alpha_x = \alpha_{x,D} - \sqrt{2\xi - 2} \quad (5.3)$$

while fixing β_x to its design value $\beta_{x,D}$.

5.2 Dependence of the determined emittance on the mismatch for different errors in the beam sizes

The dependence of the determined emittance on beam size measurement errors differs strongly in cases of a matched and a mismatched beam. Figure 5.2 shows the results of Monte Carlo simulations using 20000 random number seeds for different degrees of mismatch and for different uncertainties in the rms beam sizes. A Gaussian distribution is used to describe the probability distribution of this error. Only the results for the (2D) rms emittance in the horizontal plane are presented. The normalized emittance used in

the simulations is 2 mm mrad and the energy is 125 MeV. The mismatch is induced as described above.

We can see from Fig. 5.2 that the probability-distribution obtained from the Monte Carlo simulations is almost symmetric (top right) for a matched beam. The rms width of the emittance distribution increases strongly with an increasing ξ (top left). For a matched beam ($\xi = 1$) the error in the calculated normalized emittances is the same as that of the beam sizes. With increasing ξ the probability distribution gets a long tail towards smaller emittances (see Fig. 5.2, right side). This yields a decreased mean value of the distribution (middle left). For large ξ and large beam size errors the reconstructed beam matrix may become negative, yielding imaginary emittances. The fraction of these non-physical solutions is given in the bottom left plot in Fig. 5.2. Since the imaginary solutions are not included in the calculation of the mean value, the two curves for larger beam size errors in the middle left plot begin to increase at a certain value of ξ .

We can see from Fig. 5.2 that accurate emittance measurements are only possible if the induced mismatch is small ($\xi \approx 1$). As expected, the error in the emittance estimated from Monte Carlo simulations (rms width of the distribution) agrees with the error we obtain from the χ^2 -fit (see chapter 3.3) when assuming the same uncertainties in the beam sizes.

So far we have chosen the mismatch induced by Eq. (5.3) quite arbitrarily. The dependence of the emittance error on errors in the beam sizes can be considered more generally by calculating the emittance error for a large range of possible Twiss parameters inside the FODO section. Figure 5.3 shows the relative emittance error in the horizontal plane as a function of the Twiss parameters α_x and β_x on the first screen (4DBC2) in the BC2 diagnostic section. For the beam sizes at the four screens an error of 5% is assumed. The emittance error is evaluated by using the χ^2 -fit (see chapter 3.3).

We can see that the design values of the Twiss parameters α_x and β_x are chosen in a way that the error in the emittance has a small value. However, the region in the parameter space having a small emittance error is quite large, so other working points are possible as well. If only a beam size error is considered, a working point at larger beta functions would be even better, since the increase of the emittance error would be smaller when deviating slightly from this working point.

5.3 Dependence of the determined emittance on energy errors

Another possible error source in the emittance measurement is an uncertainty in the beam energy. However, [Cas03] shows that for a matched beam the normalized emittance is independent of energy errors.

The energy E is used for the calculation of the quadrupole k -values. According to Eq. (4.2) the perturbed k -value for the energy $E = E_0(1 + \Delta)$ is

$$k = \frac{k_0}{1 + \Delta}, \quad (5.4)$$

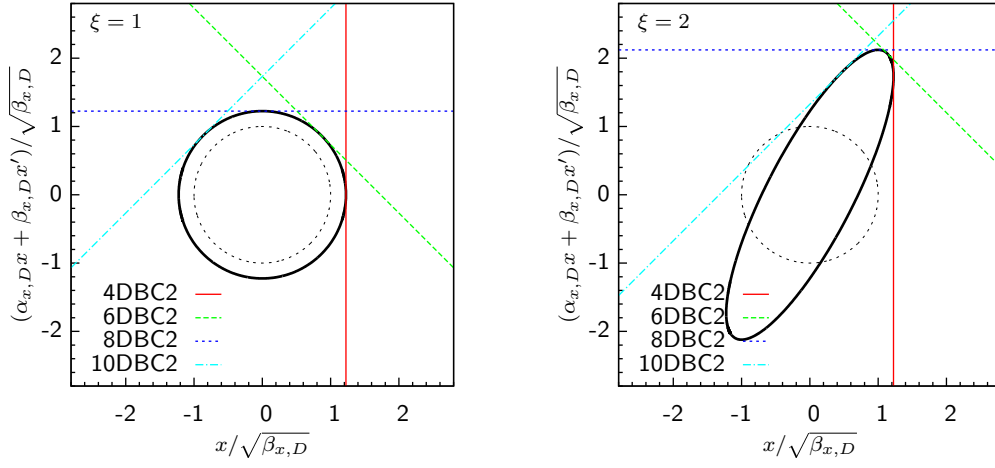


Figure 5.1: Graphical representation of the phase space ellipse in normalized coordinates. The left plot shows a matched beam and the right plot is a mismatched beam with $\xi = 2$. The dotted ellipse represents the design ellipse, the solid ellipse is an example for a hypothetical measurement. The normalized (2D) emittances of the design ellipse and the 'measured' one are 2 mm mrad and 3 mm mrad, respectively. The lines represent the beam sizes on the different screens.

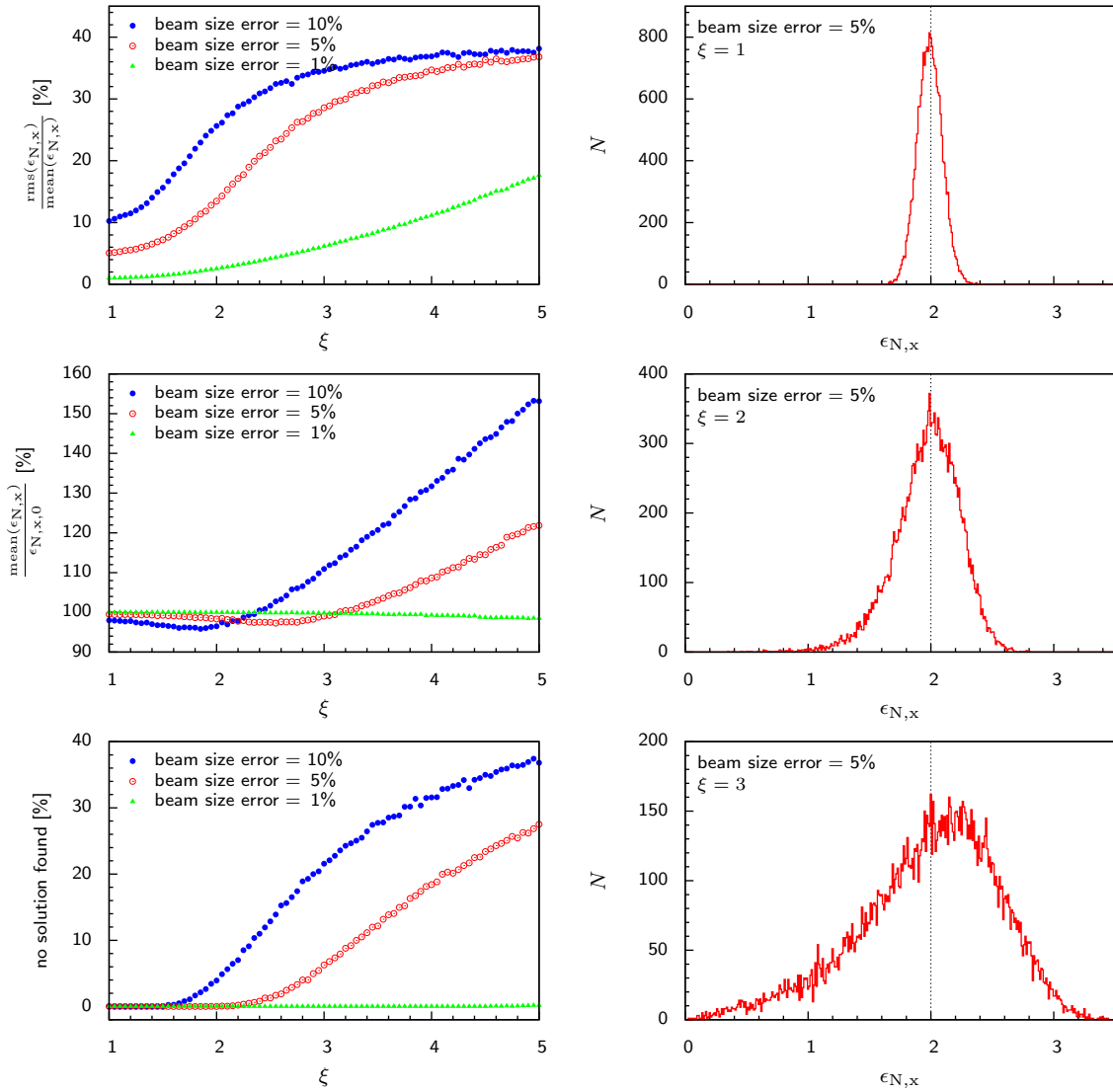


Figure 5.2: Results of Monte Carlo simulations of (2D) emittance measurement in the BC2 diagnostic section. The normalized input emittance is $\epsilon_{N,x,0} = 2$ mm mrad. Right hand side: Probability distribution of the measured emittance for three different values of the mismatch parameter ξ . The assumed beam size error is 5%. The input emittance is indicated as dotted line. Top left: relative emittance error as function of ξ . Middle left: deviation of the mean value from the input emittance. Bottom left: fraction of cases where no solution was found.

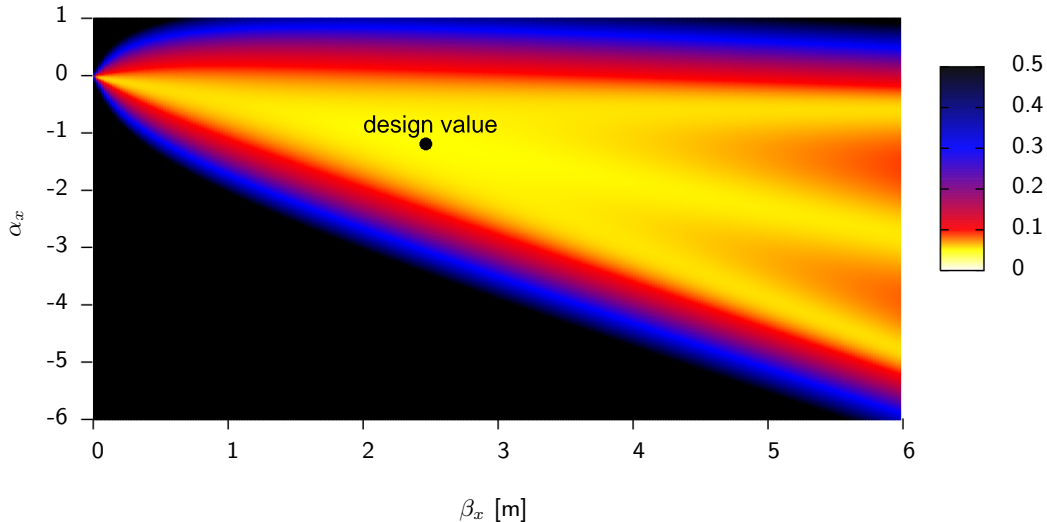


Figure 5.3: Relative error in the horizontal emittance as a function of the Twiss parameters α_x and β_x on the first screen (4DBC2) in the BC2 diagnostic section. A beam size error of 5% is assumed at all four screens. The colour black indicates a relative emittance error larger than 50%.

where ΔE_0 is the error in the energy. For a periodic solution in the FODO cells the beta function is inversely proportional to k and therefore

$$\beta = \beta_0(1 + \Delta). \quad (5.5)$$

Since we know the beta function for the matched solution, we can calculate the (2D) emittance for the unperturbed case by

$$\epsilon_0 = \frac{\langle x^2 \rangle}{\beta_0}, \quad (5.6)$$

and for the perturbed case by

$$\epsilon = \frac{\langle x^2 \rangle}{\beta} = \frac{\langle x^2 \rangle}{\beta_0(1 + \Delta)} = \frac{\epsilon_0}{1 + \Delta}. \quad (5.7)$$

The geometrical emittance has therefore an error of $(1 + \Delta)^{-1}$. In the normalized emittance, this error cancels out:

$$\gamma_{\text{rel}}\epsilon = \gamma_{\text{rel},0}(1 + \Delta)\frac{\epsilon_0}{1 + \Delta} = \gamma_{\text{rel},0}\epsilon_0 \quad (5.8)$$

This is the case, if the beta function is periodic. If the beam is not matched to the periodic solution, also the normalized emittance may depend strongly on the energy error. Figure 5.4 shows the relative deviation of the horizontal normalized emittance for two different deviations (+5% and -5%) of the beam energy as a function of the Twiss parameters α_x and β_x on the first screen (4DBC2) in the BC2 diagnostic section. Errors of the beam sizes are not included.

We can see that for our design values of α_x and β_x the energy dependence of the normalized emittance is negligible. At this working point the normalized emittance is most insensitive on energy errors when deviating slightly from the design values $\alpha_{x,D}$ and $\beta_{x,D}$.

5.4 Simulation of the (2D) phase space reconstruction with the MENT Algorithm in the BC2 section

The power of the MENT Algorithm to reconstruct the phase space distribution from four beam profiles at the OTR screens is shown in Fig. 5.5. A phase advance of 45° and a beam energy of 125 MeV is used for the reconstruction. The pixel size of the profiles is $10 \mu\text{m}/\text{pixel}$, which is similar to that of the OTR monitors. Two different phase space distributions Ψ_0 at the position of the first OTR screen are assumed. The first one consists of three two-dimensional Gaussian profiles of different widths, and the second one is chosen as

$$\Psi_0(x, x') \propto \exp\left(-\frac{x^2}{2\beta_{x,D}\epsilon_x} - xx' \frac{\alpha_{x,D}}{\beta_{x,D}\gamma_{x,D}\epsilon_x} - \frac{x'^2}{2\gamma_{x,D}\epsilon_x}\right), \quad (5.9)$$

corresponding to a Gaussian distribution in phase space, which is rotated in a way that the beam is matched ($\xi = 1$) in the BC2 diagnostic section. These phase space distributions are transformed, using the transfer matrices between the four screens, to calculate the distribution on each screen. Then the profiles of these four distributions are used as input for the MENT Algorithm. The difference to the MENT reconstruction shown in Fig. 3.1 is that here we use real transfer matrices, instead of a simple rotation. Therefore the phase space distribution is not only rotated but also sheared.

We observe a very good reconstruction of the phase space distribution even if only four projections are used (see Fig. 5.5). The initial and reconstructed normalized emittances as well as the mean square deviations of the reconstruction δ_{rec} are presented in Table 5.1.

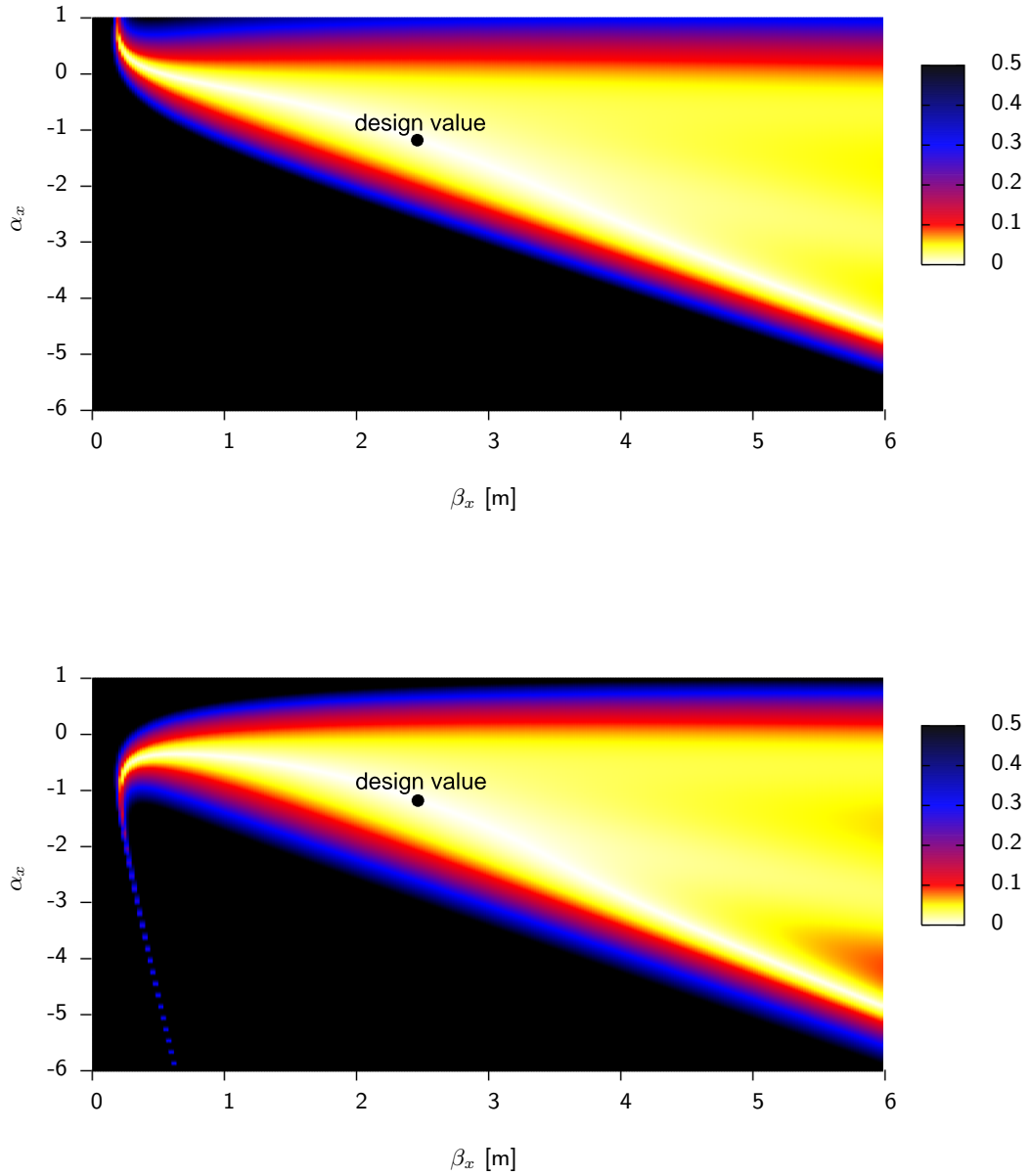


Figure 5.4: Relative deviation of the normalized horizontal emittance as a function of the Twiss parameters α_x and β_x on the first screen (4DBC2) in the BC2 diagnostic section. The energy deviation from the correct energy is +5% (top) and -5% (bottom). Errors in the beam sizes are not included. The colour black indicates a relative error in the normalized emittance larger than 50%.

	$\epsilon_{N,x,ini}$ [mm mrad]	$\epsilon_{N,x,rec}$ [mm mrad]	δ_{rec} [%]
Three (2D) Gaussian distributions	11.21	11.22	5.18
One (2D) Gaussian distribution	2.003	2.001	1.23

Table 5.1: MENT simulation in the BC2 section: initial and reconstructed emittances together with the mean square deviations δ_{rec} .

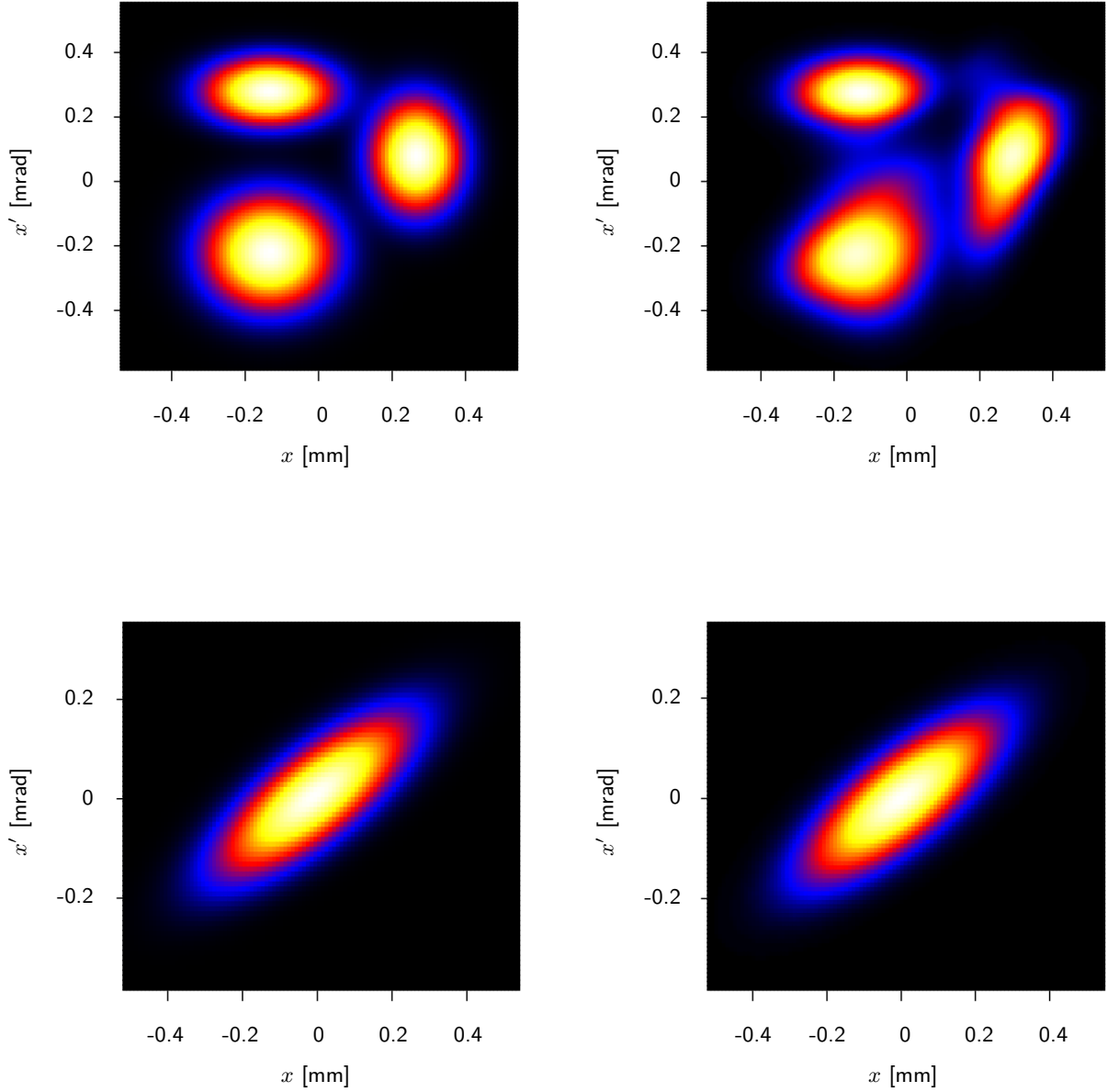


Figure 5.5: Example for MENT reconstruction in the BC2 diagnostic section for two different two-dimensional phase space density distributions. Upper graph: density distribution consisting of three two-dimensional Gaussian profiles of different widths. Left: simulated distribution, right: reconstructed distribution. Lower graph: density distribution consisting of a matched ($\xi = 1$) two-dimensional Gaussian distribution. Left: simulated distribution, right: reconstructed distribution.

6 Image analysis

As we have seen in the previous chapter, the accurate reconstruction of the rms beam sizes is important. The measurement of the spatial beam distribution with the OTR monitors delivers images consisting of 640 (hor) \times 480 (ver) pixels. Background images are subtracted in order to remove darkcurrent¹, to correct the offset generated by noise in the camera system and by X-rays, and to remove the influence of damaged pixels. In order to reduce fluctuations, the average of typically 20 background images is used.

Even after the background subtraction, Eq. (2.40) cannot directly be used to calculate the second moments of the beam distribution from the entire beam image. The second moments depend very sensitively on small offsets in the intensity. These offsets occur due to small background fluctuations and may change the second moments significantly. Therefore, a stable offset correction has to be applied.

Even if we use the highest magnification of the OTR monitors, a typical measured beam distribution covers only a small part of the entire image. The remaining part of the image contains only noise, decreasing the signal to noise ratio. Therefore, it is advantageous to evaluate only a small region on the image that includes the entire beam. This part of the image used for the beam size calculations is called region-of-interest (ROI). The signal to noise ratio of the measured beam distribution is increased using this method and in addition we get the possibility to determine the offset with higher accuracy from the remaining part of the image outside the ROI.

Figure 6.1 shows the dependence of the calculated beam sizes on the size of the ROI for a measured beam distribution. From a single beam image we subtract the averaged background image. Then, as a starting ROI, a circle with a radius of 10 pixels is selected. The maximum of the beam profiles in both planes is defined as the centre. The part of the image outside of the ROI is used to calculate the average value for the offset. This offset is subtracted from the entire image. For the calculation of the rms beam sizes, only the fraction of the image inside the ROI is used. The next regions-of-interest, indicated by an index i in Eq. (6.1), are ellipses that are chosen so that the half-axis in the x-direction, a_x , increases continuously while the half-axis in the y-direction, a_y , is scaled with the ratio of the rms beam sizes calculated for the previous, smaller ROI, indicated by the index $i - 1$:

$$a_y^{(i)} = a_x^{(i)} \cdot \frac{x_{\text{rms}}^{(i-1)}}{y_{\text{rms}}^{(i-1)}} = a_x^{(i)} \cdot \frac{\sqrt{\langle x_{(i-1)}^2 \rangle}}{\sqrt{\langle y_{(i-1)}^2 \rangle}}. \quad (6.1)$$

In each step, a different offset resulting from the average intensity outside the ROI is subtracted from the entire image.

Increasing the size of the ellipse for a small ROI that does not contain the entire beam results in a steep increase of the rms beam sizes (see Fig. 6.1). At a certain ellipse size the determined rms beam sizes become insensitive to

¹ Due to the electric fields in the gun and the accelerator modules, electrons may be released from the cavity surface by field emission and accelerated to high energies. These electrons are outside the regular bunches and generate a continuous current which is called darkcurrent.

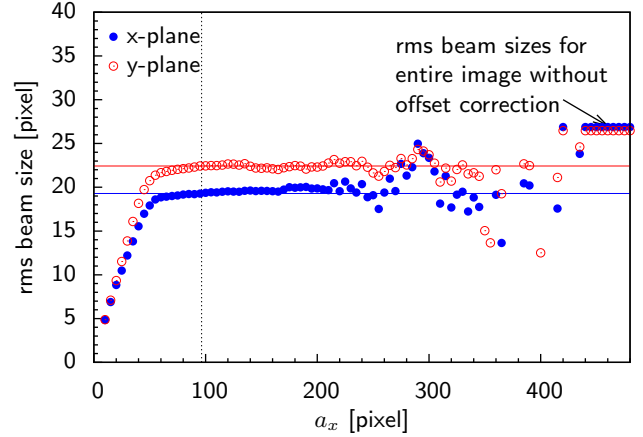


Figure 6.1: Dependence of the reconstructed beam sizes on the size of the region-of-interest. Plotted is the horizontal half-axis a_x (see text). The dotted line shows a_x for the ellipse resulting from the algorithm described in section 6.1.

small changes in the ellipse size. The ROI contains now the entire beam and also the offset is well estimated. After further increasing the ellipse size, the rms beam sizes become instable again. The reason for this is that for very large regions-of-interest only a few pixels are left to calculate the offset. Therefore, small fluctuations in these pixels have strong influence on the rms beam sizes.

6.1 Image analysis algorithm to reconstruct the second moments of the entire beam

The considerations above show that a necessary condition for a stable reconstruction of the rms beam sizes and the second moments of the beam distribution is to choose the size of the ROI so that we are in the stable region of the plot in Fig. 6.1. Let us consider a two-dimensional Gaussian distribution with the variances σ_x and σ_y . The contour lines are ellipses. The fraction P of the distribution inside an ellipse with the half-axes of $a_x = c\sigma_x$ and $a_y = c\sigma_y$ is given as [Com94]

$$P = 1 - \exp\left(-\frac{c^2}{2}\right). \quad (6.2)$$

For the measurements presented in this thesis, an algorithm converging at $c = 5$ is used ($P > 0.999996$). Due to the small dynamic range of the CCD camera (8 bit) long tails of the Gaussian distributions are cut. Therefore, using $c = 5$, the ROI is determined so, that the entire detected beam intensity is included in the ellipse.

The algorithm works as follows:

- Subtract the average over typically 20 background images from a single beam image.
- Select a circular starting region-of-interest (ROI) with the centre at the maximum of the beam profile in both planes. Calculate the offset as an average of the pixels outside this ROI and subtract the offset from the entire image. Use pixels inside the ROI to calculate the rms beam sizes.

- Select an elliptical ROI with the centre at the first moments $(\langle x \rangle, \langle y \rangle)$ of the previous ROI. The half-axes of the ellipse a_x and a_y are selected as $a_x = 5x_{\text{rms}}$ and $a_y = 5y_{\text{rms}}$, where x_{rms} and y_{rms} are the results using the previous ROI. The offset is determined and subtracted as above. The rms beam sizes are calculated using this new ROI.
- Repeat the previous step, until the rms beam sizes converge towards constant values. Calculate $\langle xy \rangle$ for the last ROI.
- Repeat the entire procedure for each beam image. Typically 20 images for each of the four OTR screens are evaluated.

The half-axis a_x of the resulting ROI is indicated in Fig. 6.1 as a dotted line. The effect of the ROI on the projections can be seen in Fig. 6.2. Three steps of the algorithm are shown in Fig. 6.3.

Since the beam position may jitter from shot to shot (typically around $20 \mu\text{m}$ to $40 \mu\text{m}$ rms at the OTR position), the calculation has to be applied to each single beam image. Averaging over the beam images would result in overestimated beam sizes, since the beam position jitter produces an additional beam size contribution. As the final value for the rms beam size (second moments, respectively), we use the mean value of the beam sizes determined from the single beam images.

For the calculation of the emittances, the error of this mean value has to be estimated. Sources for fluctuations in the beam sizes may be: jitter of the darkcurrent, noise in the camera system (X-rays, noise of the CCD), jitter of the beta functions for example due to fluctuations in the magnet power supplies, or jitter of the emittances for example due to a fluctuating laser shape on the cathode from shot to shot. In order to estimate the error in the beam sizes, the error for a single measurement is used. This is a conservative estimate, but it allows for the possibility that the beam size may fluctuate due to a jitter in the emittances from shot to shot.

6.2 Beam intensity cut to calculate the core emittance

As we have mentioned above the emittance depends sensitively on tails in the phase space distribution. A small fraction of particles can cause a significant increase of the emittance. Furthermore, fluctuations in these tails have a large influence on the emittance. Therefore, in addition to the emittance of the entire phase space distribution, the emittance of the high density core of this distribution is of interest. We can calculate such an emittance by cutting away a small fraction of particles in the tails in phase space. This cut can be done by applying a threshold procedure in the phase space, which means that the phase space distribution must be known.

When we calculate the emittance from the measured second moments, such a procedure is not possible, since we do not know from the spatial coordinates if a certain particle is in a tail of the phase space distribution. However, comparisons with the reconstructed phase space distributions using the MENT Algorithm show that an intensity cut as described below yields realistic results.

In order to estimate the emittance of the beam core containing a fraction f of the entire beam distribution, the part of the measured two-dimensional spatial distribution

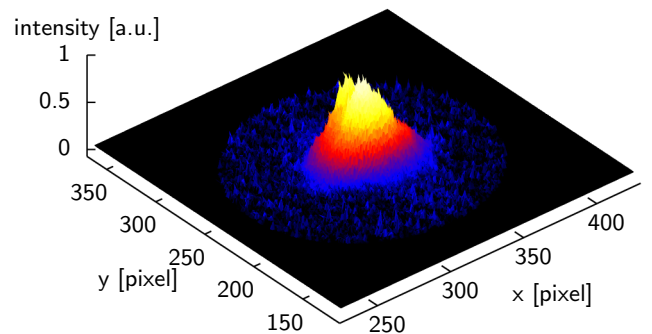
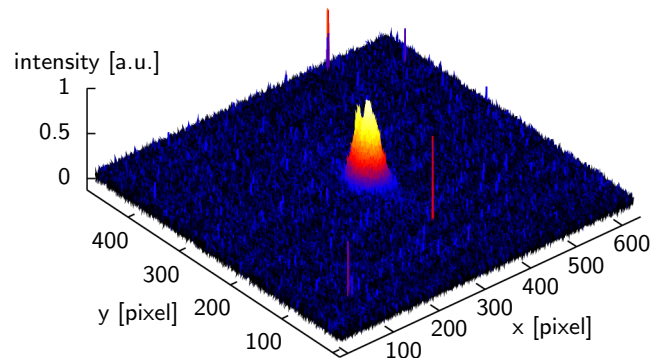
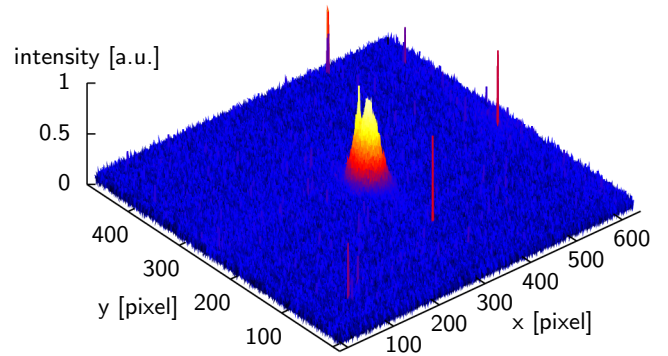


Figure 6.3: Example images to demonstrate the image analysis algorithm. From the single beam image (top) the averaged background is subtracted (middle). In the bottom image the ROI used for the calculation of the beam sizes is shown.

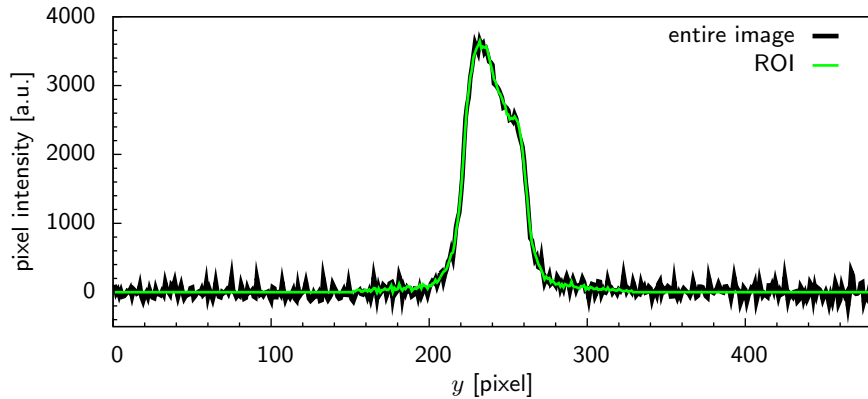


Figure 6.2: Projection of the measured 2D distribution onto the y -axis for the entire image and for the region-of-interest.

with the lowest intensity is cut away. In our final ROI from the algorithm described above the offset is chosen in a way that we have symmetric noise fluctuations around the baseline in areas inside the ROI with inexistent beam intensity. These positive and negative contributions compensate each other and do not contribute to the beam sizes. If we apply a simple threshold procedure to estimate the core of the beam, this balance is distorted and only the positive distributions are left, blowing up the rms beam sizes. Therefore, we use a slightly modified algorithm.

The algorithm works as described below.

- As an initial image, the ROI described above is used. The total intensity in this image corresponds to 100% of the beam distribution.
- A simple low pass filter, which substitutes the intensity of each pixel by the average of the 11×11 -pixel area surrounding this pixel, is applied to the initial ROI.
- A threshold procedure is applied to this filtered image. Every pixel with an intensity lower than the threshold is set to zero, every pixel with a higher intensity is set to one. This results in a mask which is multiplied with the initial ROI. The ratio f of the total intensity of this new image and the intensity of the initial ROI is calculated.
- The previous step is repeated and the threshold is changed until the remaining intensity fraction is the desired fraction f .
- From the final image the rms beam sizes (the second beam moments, respectively) are calculated.

The same algorithm is applied to the reconstructed phase space distribution from the MENT Algorithm to estimate the core emittance. In Fig. 6.4 the intensity distribution of the image in Fig. 6.3 is shown after a cut of 10% of the beam intensity.

6.3 Noise reduction with filters

Although the use of a region-of-interest reduces the noise in the density distribution significantly (see Fig. 6.2), a further noise reduction is possible by applying appropriate filters to the images.

Filtering in the spatial coordinates offers only reduced possibilities. Since the noise consists mainly of high frequencies, a common filter technique is first to perform a two dimensional Fourier transformation of the image, then to suppress the high frequencies and finally to transform the

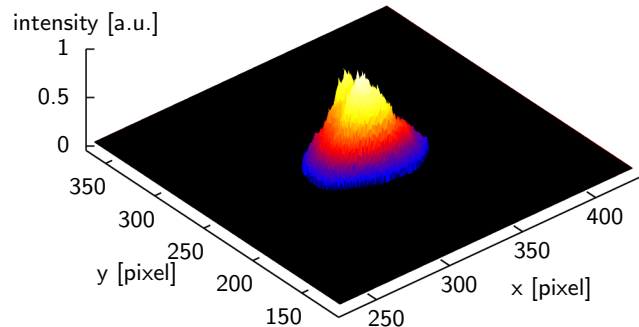


Figure 6.4: An example image demonstrating the intensity cut performed to calculate a core emittance. As an initial image the same image as shown in Fig. 6.3 is used. The remaining intensity ratio after the cut is $f = 90\%$.

distribution back to the spatial coordinates. This method, however, does not only remove the noise but also, since the high frequencies are missing, smears out the sharp edges in the measured beam density distribution.

A more efficient filtering can be achieved by using a wavelet transformation [Lin01] instead of the Fourier transformation. The use of an appropriate threshold technique in the wavelet domain reduces the noise while rarely changing the density distribution. In this thesis a wavelet package provided by the Rice University is used [BCF⁺02]. The filter is applied after subtracting the background but before searching the ROI. Figure 6.5 shows the difference in the profiles with and without a wavelet filter and in Fig. 6.6 an image before and after applying an wavelet filter is shown. For all measurements presented in this thesis such a filter is applied.

6.4 Determination of MENT profiles

In the MENT reconstruction of the phase space distribution we use the beam profiles of the selected ROI. The images are filtered before searching the ROI. In order to benefit from the repetition of the measurement (typically 20 times) the profiles are averaged. However, when the beam position jitters, a simple averaging results in a broadened profile. Therefore, the measured profiles are rebinned and the centre of all profiles is moved to the same position before averaging the profiles. The averaged profile is then used as input profile for the MENT reconstruction.

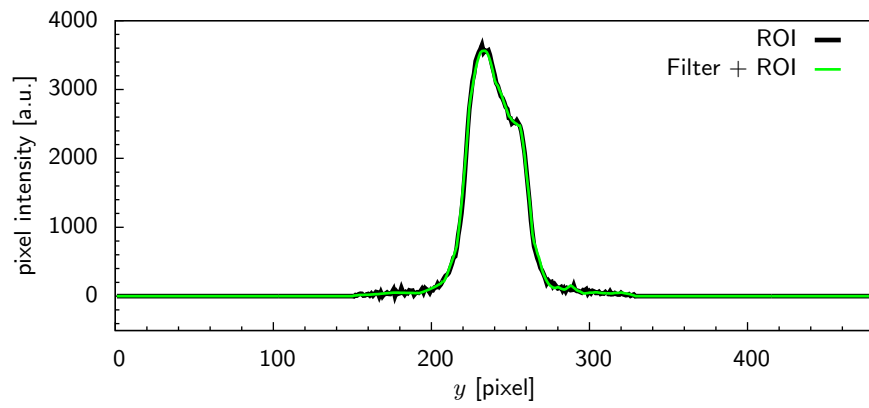


Figure 6.5: Projection of the region-of-interest onto the y -axis with and without applying a wavelet filter.

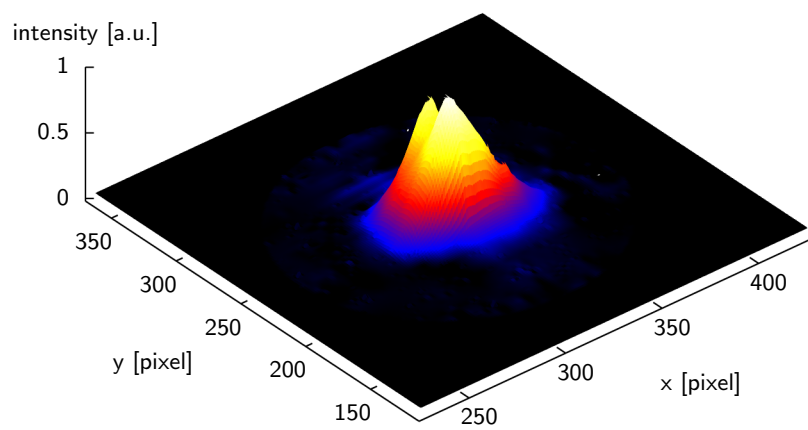
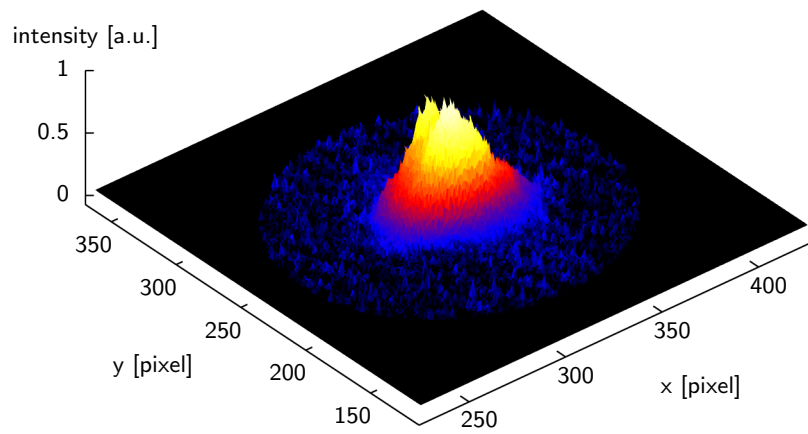


Figure 6.6: Difference between an original (top) and a wavelet filtered image (bottom). Both images show only the region-of-interest.

7 Measurements

7.1 Calibration of the OTR monitors

The calibration of the OTR monitors is done by using the calibration marks scratched onto the screen holders. The calibration marks are separated by 2 mm in both planes with an uncertainty of 3% [Cia05]. When using the highest magnification of the OTR monitors, there are only two calibration lines visible in the vertical plane and three to five in the horizontal plane.

The screen holder is illuminated and an image of the calibration marks is recorded (see Fig. 7.1, top). From this image the projections onto the horizontal and vertical planes are calculated. In the horizontal plane, the camera is looking at the calibration marks with an angle of 45° . Therefore, the marks appear to be quite narrow. Only the reflections of the light at the marks are visible, leading to sharp spikes in the horizontal profile. In the vertical plane, the marks are visible in the profiles as shadows (see Fig. 7.1, middle).

From these profiles a baseline is subtracted. After applying a threshold procedure only the spikes or shadows of the calibration marks are visible in the profiles (see Fig. 7.1, bottom). In the horizontal plane the centre of each spike is calculated using Eq. (2.41). The mean value of the distances between the single spikes is then used to calculate a horizontal calibration factor $C_{\text{OTR},x}$. Here we have to take into account that the screen is mounted with an angle of 45° . In the vertical plane a Gaussian profile is fitted at the edges of the shadows in the profile using 5 pixels of each side (see Fig. 7.1, bottom right). For the calculation of the vertical calibration factor $C_{\text{OTR},y}$ the distance between the centres of the two Gaussian fits is used.

The calibration factors for the screens in the BC2 diagnostic section are given in Tab. 7.1. The error in the horizontal plane is the statistical error resulting from the three to five calibration marks visible on the calibration images. This error is small compared to the uncertainty in the distance between the calibration marks. Therefore, a 3% error in the calibration factors is used as systematic error in the emittance calculations.

7.2 Emittance measurements

We present here only results of measurements in the BC2 diagnostic section. Some measurements have been also performed in the SUND section. Here however, further investigations and improvements are still needed, since, for example, the light intensity on two of the OTR screens is very low and synchrotron light originating in a dipole magnet in the collimator section can disturb the measurements.

As mentioned above, only effective emittances are calculated, since contributions due to dispersion are not known. We only present the normalized (2D) emittances $\epsilon_{N,x}$ and $\epsilon_{N,y}$.

The results for the intrinsic emittances need to be further investigated since we get imaginary values for some settings of the accelerator. Possible reasons for this are small alignment errors in the camera system or slightly skewed quadrupoles in the diagnostic section.

For all measurements, the nominal charge was 1 nC and the beam energy 127 MeV. The beam energy was determined from the current of the dipole magnets of the first

bunch compressor (BC2) when the beam was centred in the middle of the OTR screen in the dispersive section of the bunch compressor. Only one bunch per bunch train was used. During all measurements the beam was guided through the bunch compressor, but most of the measurements were performed without compression.

The measurements presented here were performed on different days. Therefore, the machine status and parameters like the laser profile on the cathode, the RF settings, and the guidance of the beam through the first accelerator module may be different. This may produce differences in the emittance measured on different days. The injector was not optimized for minimal emittances in all measurements.

The shown results have been obtained by two different methods: the fit (see Section 3.2) and the tomographic phase space reconstruction using the MENT Algorithm. In both cases we provide two normalized emittances: the rms emittance for the entire measured beam intensity (indicated here as 100% value) and the emittance of the beam core containing 90% of the beam intensity (indicated here as 90% value). The choice of cutting away 10% is quite arbitrary. However, one can see from the difference between those two numbers how strongly the tails contribute to the emittance.

For the results from the fit we present two kinds of errors. The first one is the statistical error resulting from the different beam sizes obtained for the different beam images (typically 20 images per screen). It is calculated using the error propagation presented in Section 3.3. The second error is the systematic error of the measurement. We have assumed the following systematic errors:

- 3% error of the beam sizes due to uncertainties of the calibration factors $C_{\text{OTR},x}$ and $C_{\text{OTR},y}$ of the OTR monitors
- 5% error of the beam energy
- 6% error of the gradient of the quadrupoles in the BC2 FODO section

The systematic error is calculated using Monte Carlo simulations. Rectangular error distributions are used with a width of two times the assumed error. The distributions are centred around the measured values. From the results of the Monte Carlo simulation the systematic error is determined as the rms value of the distribution. The plots below show only the statistical error. However, in the tables of Appendix C both the statistical and systematic errors are presented. No error estimation is performed for the results of the MENT Algorithm.

7.2.1 Matching of the Twiss parameters in the BC2 diagnostic section

As we have seen in Chapter 5, the matching of the Twiss parameters inside the FODO lattice is very important for accurate emittance measurements. To match the Twiss parameters to the design values, first an initial emittance measurement is performed. From this measurement we obtain the Twiss parameters at the first screen in the FODO lattice (4DBC2). By using Eq. (2.30) we track the Twiss parameters upstream of the matching section, in front of the FODO

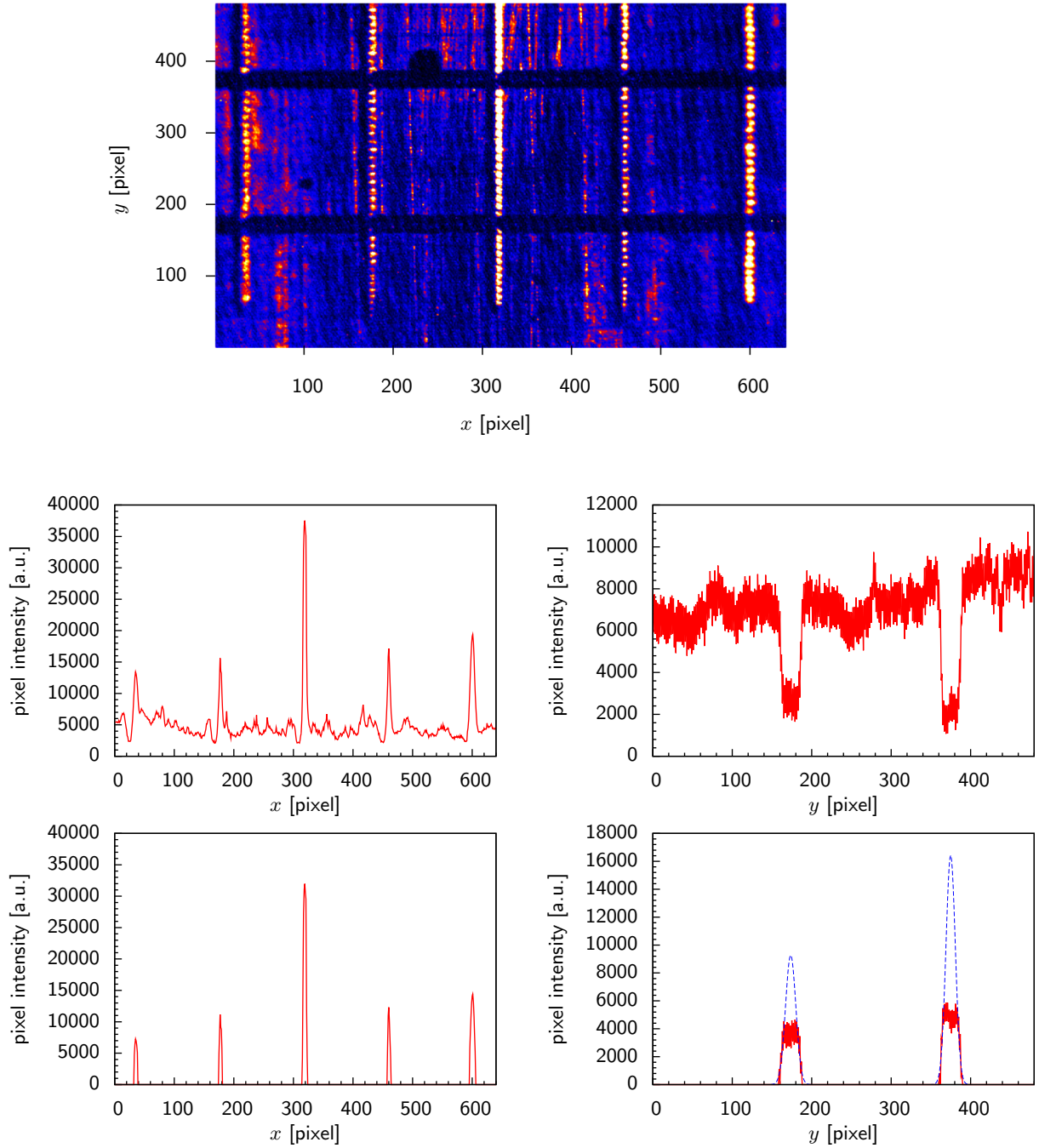


Figure 7.1: Calibration of the OTR monitors. Top: image of the calibration marks. Middle: projection of the calibration image onto the x - and y -plane. Bottom: projections after baseline subtraction and threshold procedure. In the vertical plane also the Gaussian fits are shown (dashed line).

	4DBC2	6DBC2	8DBC2	10DBC2
$C_{\text{OTR},x} \left[\frac{\mu\text{m}}{\text{pixel}} \right]$	8.874 ± 0.015	9.869 ± 0.059	10.035 ± 0.092	10.018 ± 0.054
$C_{\text{OTR},y} \left[\frac{\mu\text{m}}{\text{pixel}} \right]$	9.036	9.980	9.932	9.949

Table 7.1: Calibration factors for the OTR monitors in the BC2 diagnostic section. Only the values for the highest magnification are presented.

matching iteration	$\xi_x^{90\%}$	$\xi_y^{90\%}$	$\xi_x^{100\%}$	$\xi_y^{100\%}$
initial optics	1.316	1.319	1.275	1.210
first iteration	1.027	1.025	1.055	1.001
second iteration	1.002	1.009	1.024	1.013

Table 7.2: Example for a matching procedure in the BC2 diagnostic section. The measured Twiss parameters from the fit for 90% beam intensity are used to calculate a new optics.

lattice, and calculate a new optics within the matching section to obtain matched Twiss parameters. When starting with a mismatched beam, two or three iterations might be necessary to obtain a well matched beam, because not only the error of the measured emittance may be large but also the error of the Twiss parameters.

Typically, we calculate the Twiss parameters from the beam core containing 90% of the beam intensity. This avoids that tails in the phase space dominate the resulting values. However, in most cases also the Twiss parameters for 100% beam intensity are well matched when using the 90% values for the matching.

Table 7.2 gives an example of the quality of the matching. Two matching iterations have been performed using 90% of the beam intensity. In these examples, already the first iteration leads to a small mismatch in both planes. The effect of this procedure on the matching of the entire beam (100% beam intensity) is also presented.

7.2.2 Dependence of the emittance on the main solenoid current

An important component at the RF gun is the main solenoid. It is used to counteract space charge induced emittance growth. A small emittance is achieved, when the solenoid focuses the beam such that the beam waist is positioned at the first accelerator cavity of ACC1. The gradient of ACC1 is chosen such that the focusing of the beam during acceleration is small and a waist at the exit of ACC1 is produced.

Figure 7.2 shows the measured normalized emittances for different solenoid currents. Since the focusing of the beam depends on the main solenoid current, the optics in the matching section needs to be adjusted for each setting of the main solenoid in order to get a matched beam inside the diagnostic section. The consistency between the results from the fit and from the phase space tomography is very good. We see that for small emittances, the difference between the 100% values and the 90% values is almost a factor of two. The results are shown in Tables C.1 and C.2 in Appendix C.

In the horizontal plane we obtain a minimum emittance for a main solenoid current around 277 A to 278 A. In the vertical plane the minimum is shifted by 1 A to lower currents. The product of the two emittances has its minimum at a current of 277 A. This current is used for the operation of the machine.

The solid curve in Fig 7.2 shows ASTRA [AST] simulation results [Kim05]. A normalized emittance of 2 mm mrad for the minimum is used in this simulation. We see that the simulation describes the tendency of the measurement very well.

In Fig. 7.3 and 7.4 the reconstructed phase space distributions at the first screen (4DBC2) are shown. We can see also here that the occupied phase space area has a minimum around 277 A. The orientation of the phase space distribu-

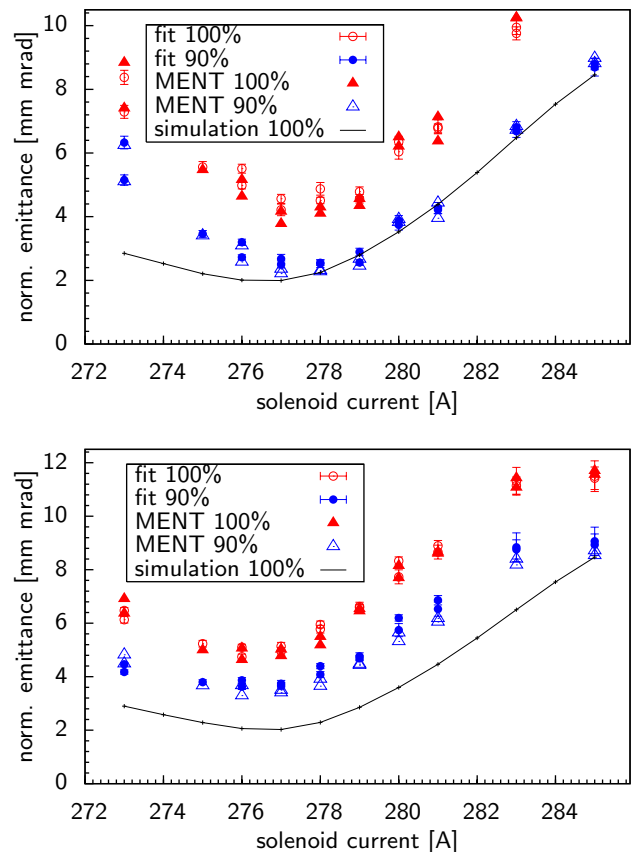


Figure 7.2: Normalized emittance versus the current of the main solenoid. Top: horizontal plane, bottom: vertical plane. The results of the fitting method (fit) and the tomographic phase space reconstruction (MENT) are shown both for 100% and 90% beam intensity.

tions is the same for all solenoid currents. This also shows, that the matching of the Twiss parameters works well.

7.2.3 Dependence of the emittance on the ACC1 off-crest phase

The phase of the first accelerator module ACC1 specifies the compression strength inside the first bunch compressor (BC2). If this phase is chosen in such a way that the bunches are accelerated on the crest of the RF wave, the bunches are not compressed. For smaller phases, the compression strength increases.

Figure 7.5 shows the dependence of the normalized emittance on the phase of the ACC1 RF wave. Only for the on-crest phase the beam energy is 127 MeV. For smaller phases the beam energy is given by $E = 127 \text{ MeV} \cdot \cos \phi$, where ϕ is the off-crest phase. At the beginning of the emittance measurements, the on-crest phase was determined by measuring the beam size on a screen inside the dispersive section of BC2. The minimum beam size corresponds to the minimum energy spread and we considered it as the on-crest phase. During the emittance measurements the on-crest phase has not been monitored. Later, we found that the ACC1 phase may drift about $\pm 1^\circ$ within about half an hour.

We can see that in the vertical plane, the normalized emittance is almost independent of the ACC1 phase. In the horizontal plane, we see a steep increase of the normalized emittance for large compressions. There are several

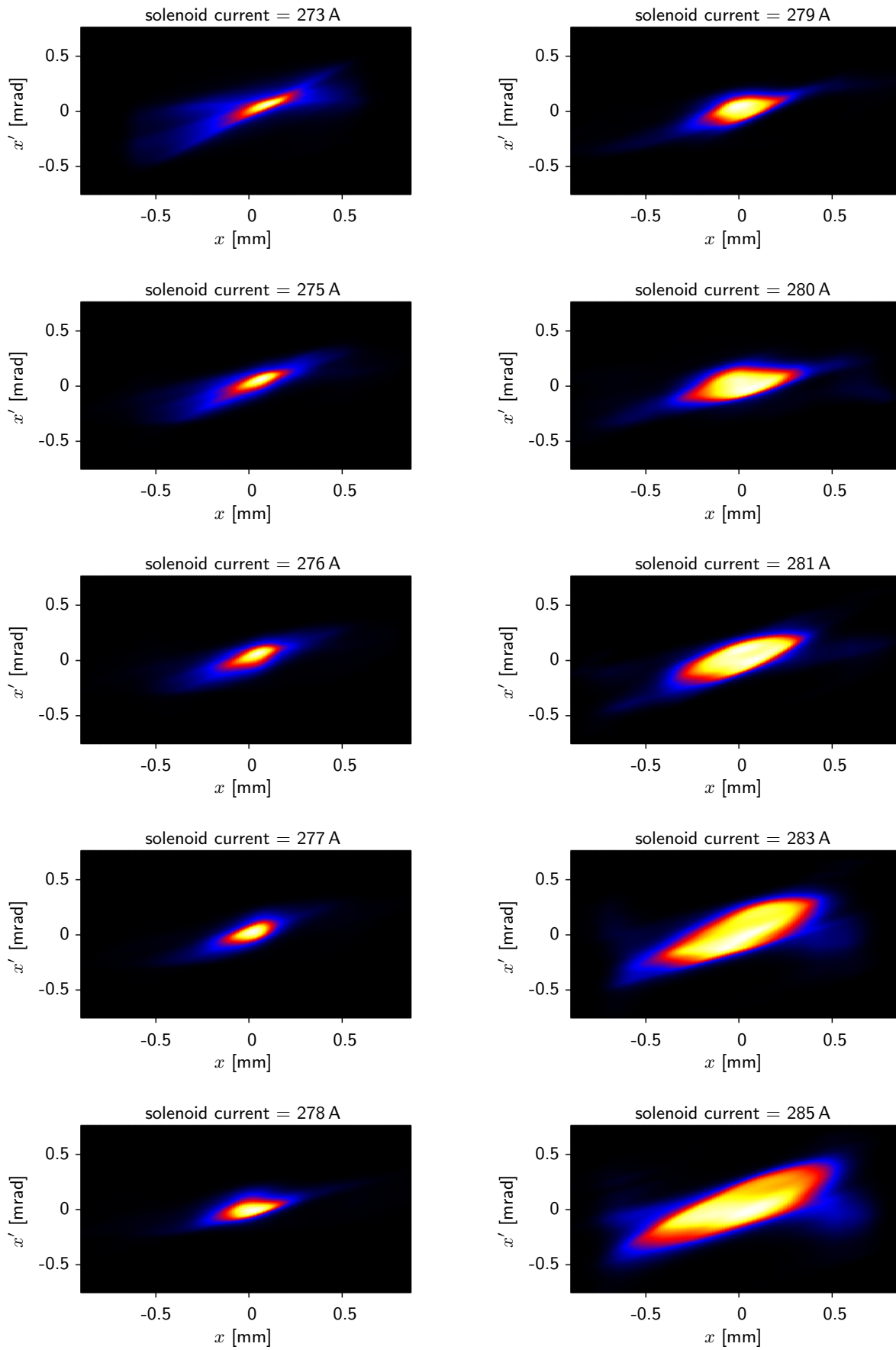


Figure 7.3: Reconstructed phase space distributions (horizontal plane) for different currents of the main solenoid.

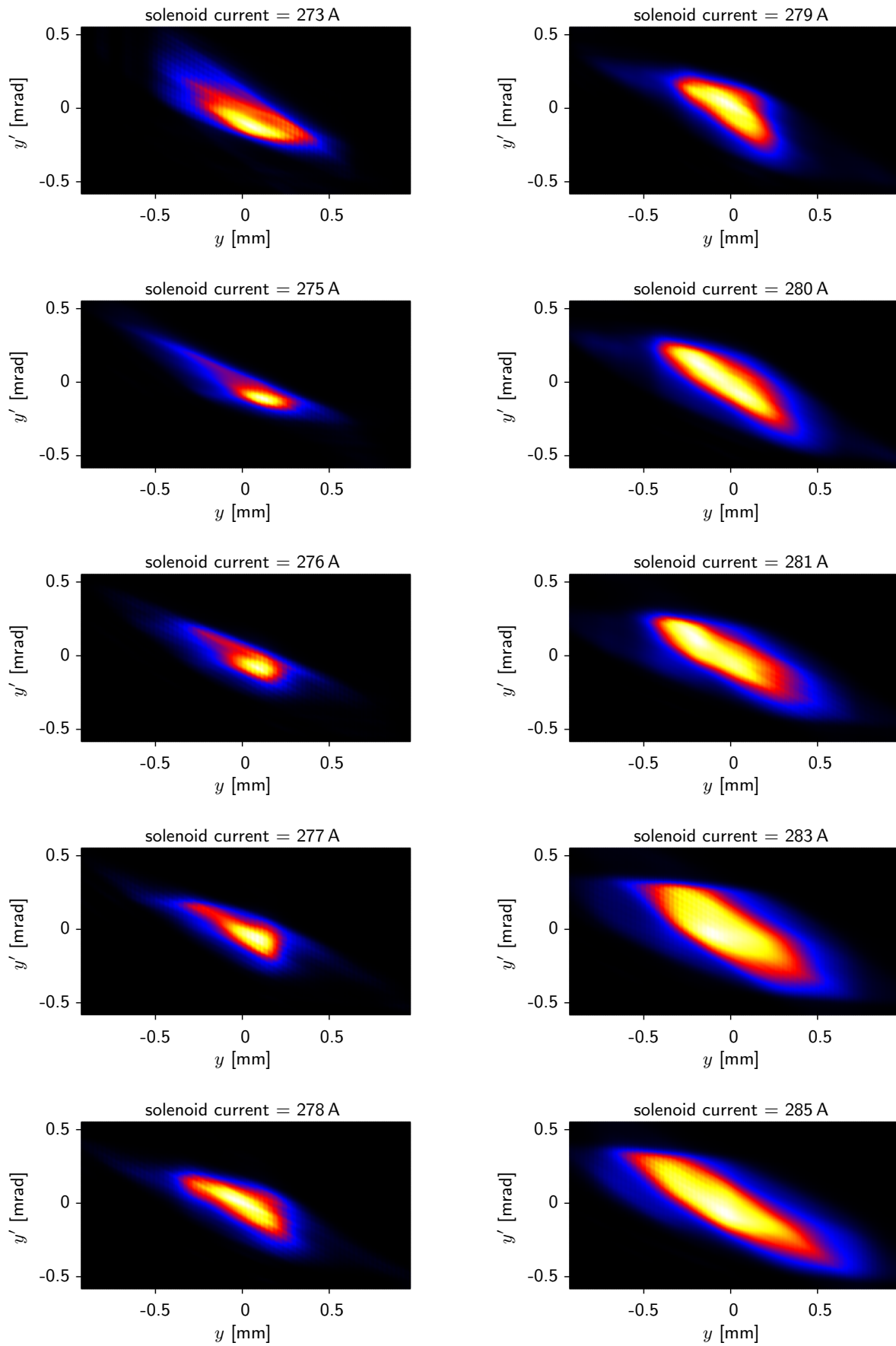


Figure 7.4: Reconstructed phase space distributions (vertical plane) for different currents of the main solenoid.

possible explanations for this, like coherent synchrotron radiation generated in the bunch compressor dipoles, or residual dispersion, but the reason for this emittance growth in the horizontal plane is not yet understood. It would be interesting to repeat this measurement and to measure the emittance also for decompressing phases ϕ . In that case the coherent synchrotron radiation can be neglected. In case of residual dispersion, however, we would expect the same behaviour of the measured emittance as we would for compressing phases ϕ , since the generated energy spread is the same.

In Fig. 7.6 and 7.7 the reconstructed phase space distributions at the first screen (4DBC2) for different ACC1 phases are shown. We can see that in the vertical plane the distribution is almost independent on the ACC1 phase. In the horizontal plane we see an increased fraction of the intensity in the tails of the distribution for increasing compression strength. In presence of dispersion, the transformation assumed in the tomographic reconstruction would be wrong, since no energy dependence is considered, and the tails in phase space could be reconstruction artefacts. We can also see that the shape of the high density core of the horizontal phase space distribution changes at a high compression strength. The reason is that we have matched the Twiss parameters to the design values for each setting of the ACC1 phase, using the results of the fit for 90% beam intensity. At low ACC1 phases, more than 10% of the beam intensity is in the tails of the phase space distribution, leading to a different matching for the beam core.

The measured normalized emittances are given in Tab. C.3 and C.4 in Appendix C.

7.2.4 Reproducibility of the emittance measurements

In order to analyse the reproducibility of the measured emittance, the measurement has been repeated ten times within a period of about an hour. The settings of the accelerator parameters have not been changed during the experiment. The results are shown in Fig. 7.8 and Tab. C.5 and C.6. The normalized emittance is stable during the measurements. The fluctuations in the horizontal plane are stronger (0.10 mm mrad rms, fit 100%) than in the vertical plane (0.05 mm mrad rms, fit 100%). This may be caused by orbit fluctuations in the bunch compressor due to small fluctuations in the beam energy. The normalized emittance for 90% beam intensity is roughly the same for both planes. However, the normalized emittance for 100% beam intensity is about 0.5 mm mrad larger in the horizontal plane than in the vertical plane which may be a hint for residual dispersion in the horizontal plane.

7.2.5 Smallest emittances measured

The smallest normalized emittances we have measured so far are shown in Tab. 7.3. For these measurements, 10 beam images and background images per screen were recorded. These measurements show that the normalized design emittance of 2 mm mrad has been achieved. As discussed in Section 4.1, measurements at PITZ indicate, that the emittance could even decrease by a factor of two when flat longitudinal and transverse laser profiles are used. This could not be measured here because such a laser beam is not yet available at the VUV-FEL.

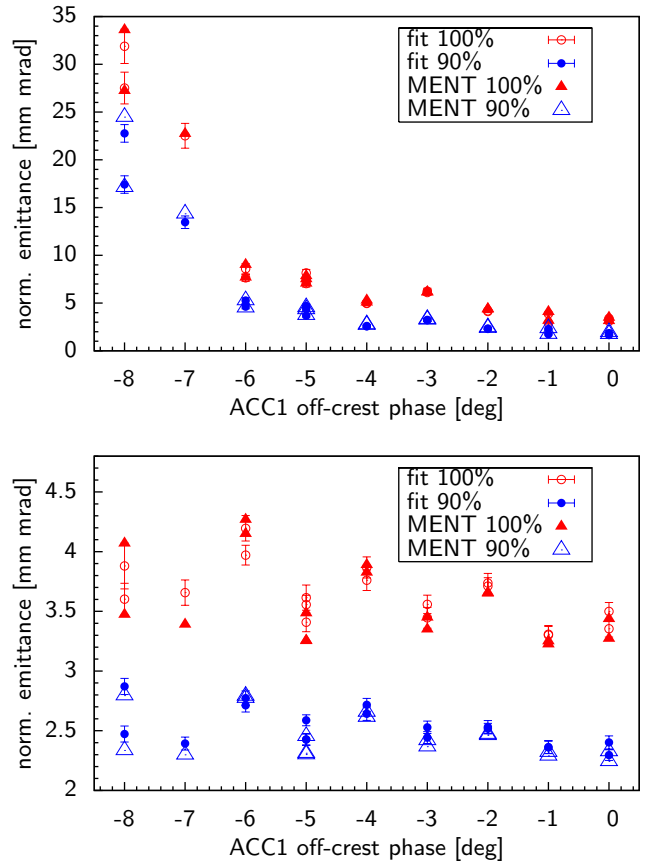


Figure 7.5: Normalized emittance versus the phase of the accelerator module ACC1. A phase of 0 corresponds to the on-crest phase. Top: horizontal plane, bottom: vertical plane. The results of the fitting method (fit) and the tomographic phase space reconstruction (MENT) are shown both for 100% and 90% beam intensity.

21.02. 2005	$\epsilon_{N,x} \pm \text{stat. err.} \pm \text{syst. err.}$ [mm mrad]	ξ_x	$\epsilon_{N,x}$ [mm mrad]
time	Fit 100 %		MENT 100%
4:23	$1.82 \pm 0.05 \pm 0.18$	1.128	1.83
4:31	$1.61 \pm 0.05 \pm 0.14$	1.073	1.70
4:47	$1.63 \pm 0.04 \pm 0.12$	1.069	1.68
	Fit 90 %		MENT 90%
4:23	$1.08 \pm 0.03 \pm 0.08$	1.116	1.08
4:31	$1.01 \pm 0.03 \pm 0.08$	1.025	1.00
4:47	$1.03 \pm 0.02 \pm 0.07$	1.026	0.98

21.02. 2005	$\epsilon_{N,y} \pm \text{stat. err.} \pm \text{syst. err.}$ [mm mrad]	ξ_y	$\epsilon_{N,y}$ [mm mrad]
time	Fit 100 %		MENT 100%
4:23	$1.95 \pm 0.08 \pm 0.11$	1.033	1.97
4:31	$1.88 \pm 0.07 \pm 0.10$	1.002	2.03
4:47	$1.86 \pm 0.04 \pm 0.11$	1.005	1.98
	Fit 90 %		MENT 90%
4:23	$1.17 \pm 0.06 \pm 0.08$	1.037	1.15
4:31	$1.13 \pm 0.06 \pm 0.07$	1.016	1.16
4:47	$1.17 \pm 0.03 \pm 0.08$	1.032	1.16

Table 7.3: Smallest emittances measured. Top: normalized rms emittances in the horizontal plane, bottom: normalized rms emittances in the vertical plane. The results for both 100% and 90% beam intensity are shown.

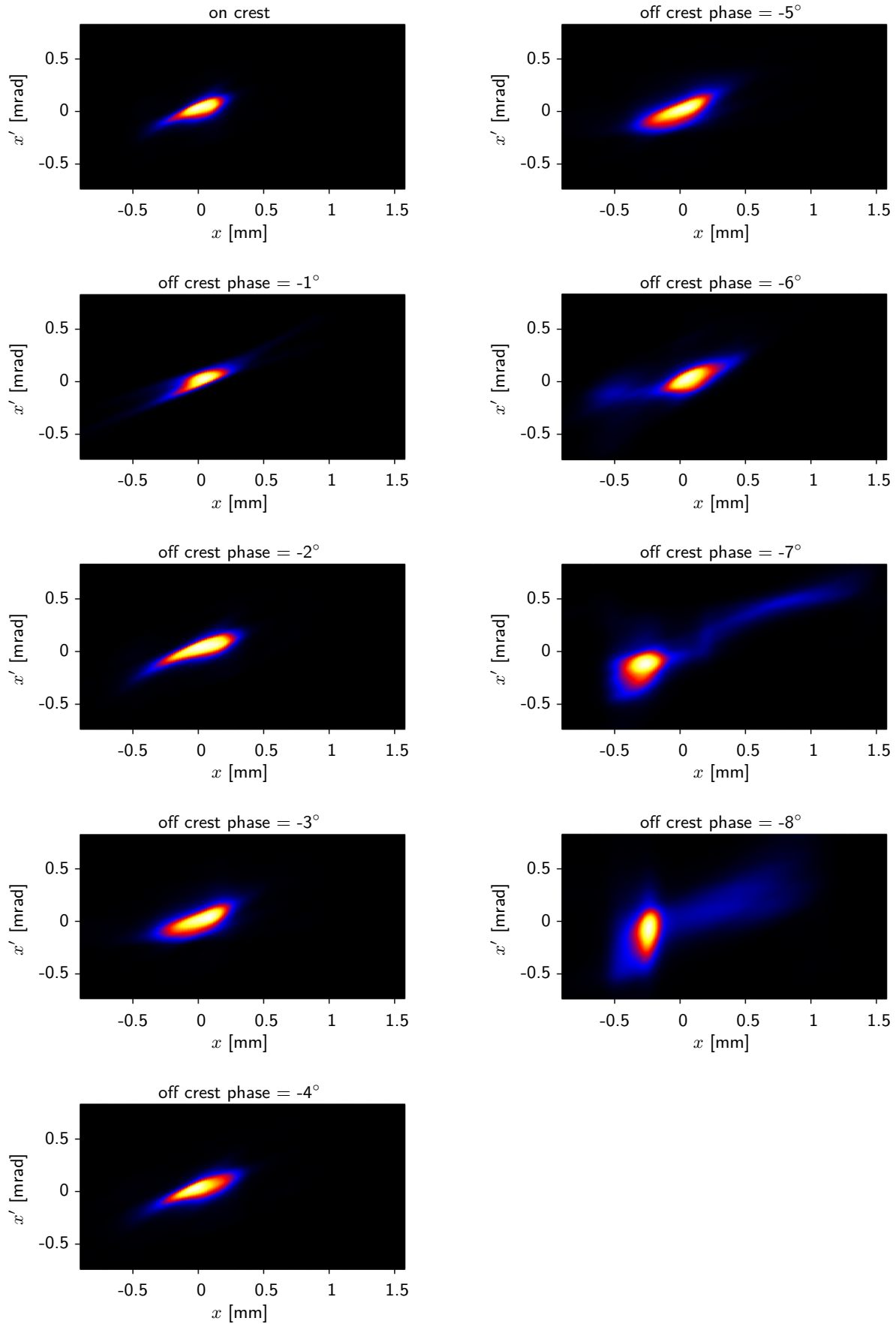


Figure 7.6: Reconstructed phase space distributions (horizontal plane) for different phases of the accelerator module ACC1.

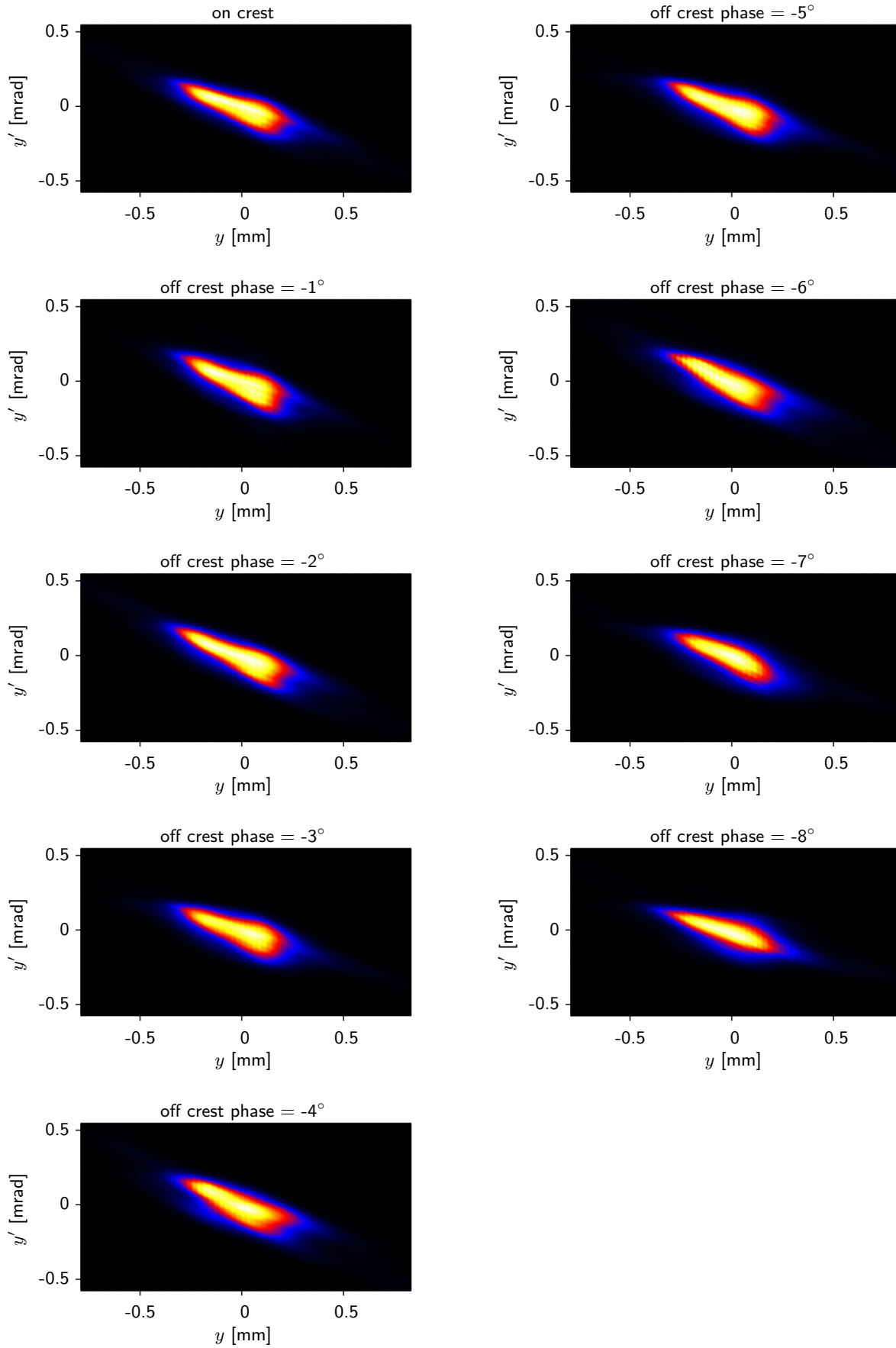


Figure 7.7: Reconstructed phase space distributions (vertical plane) for different phases of the accelerator module ACC1.

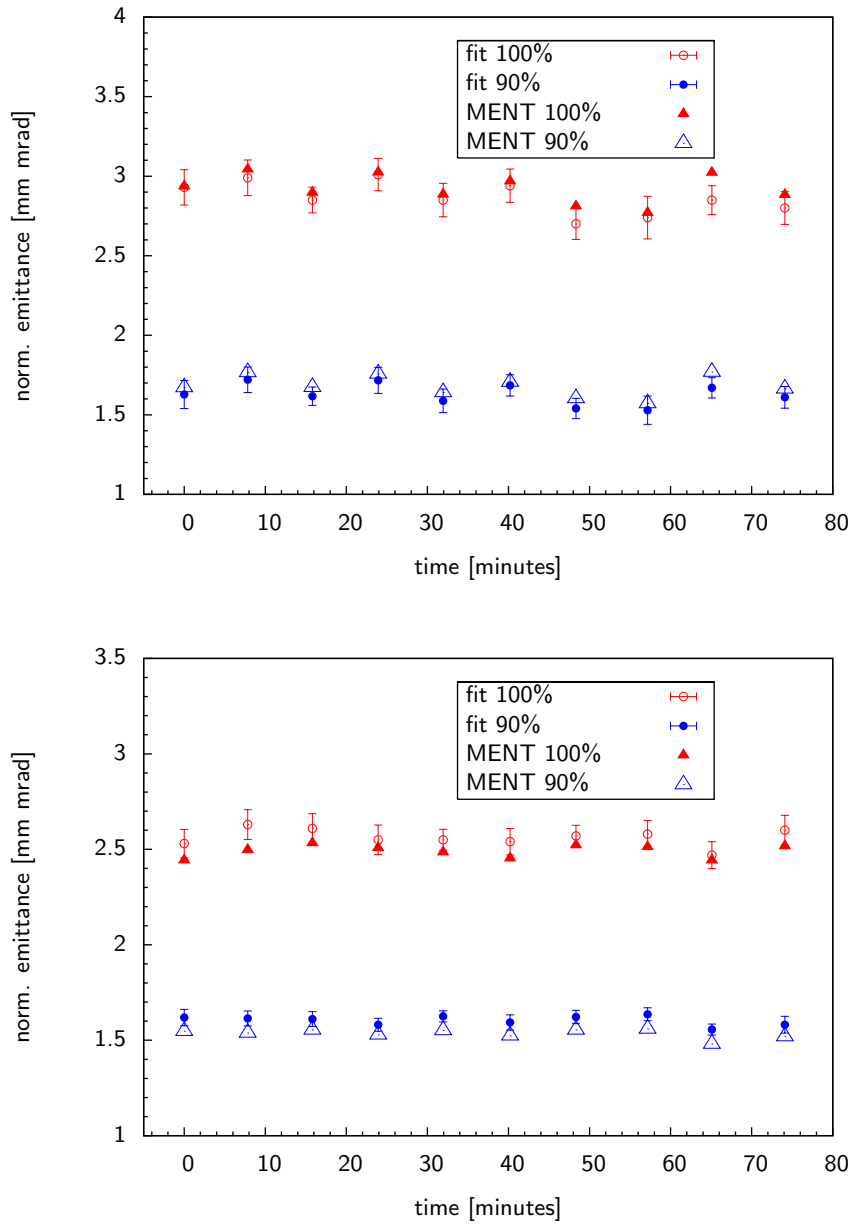


Figure 7.8: Reproducibility of the measured emittance. The measurement has been repeated ten times during 75 minutes. Top: horizontal plane, bottom: vertical plane. The results of the fitting method (fit) and the tomographic phase space reconstruction (MENT) are shown both for 100% and 90% beam intensity.

8 Conclusion

An electron beam with a small emittance and a high peak current is needed to drive a SASE FEL. For the understanding and optimization of the electron beam, precise measurements of the beam parameters are essential. At the VUV-FEL, the emittance is calculated from beam distribution measurements using optical transition radiation. At four screens in a FODO lattice images of the spatial beam distribution are recorded. We use two different methods for the determination of the emittance: In the first method, we fit the Twiss parameters and the emittance to the measured beam sizes and in the second method we perform a tomographic reconstruction of the phase space density distributions with the Maximum Entropy Algorithm.

It has been shown that the error of the measurement depends sensitively on the choice of the design Twiss parameters inside the FODO lattice. In addition, the precise knowledge of the beam profiles and beam widths is needed. By neglecting only a small fraction of particles inside the tails of the beam distributions, the determined emittance changes significantly. Therefore, an image analysis method was developed, which is insensitive to noise in the images and which is especially suited for the reconstruction of the tails in the beam profiles. In order to see how strongly the emittance is dominated by tails in the phase space distribution, not only the emittance of the entire beam is calculated, but also an emittance for the high density beam core. This core emittance is defined by cutting away 10% (arbitrary choice) of the beam intensity in the tails of the phase space distribution yielding a 90% emittance. This core emittance together with the emittance of the entire beam provides additional information for the optimization of the electron beam.

The experimental results from the fitting and the tomographic method agree well for both the emittance of the entire beam (100%) and for the core emittance, containing 90% of the beam intensity. By using the measured Twiss parameters, we were able to match the beam to the design optics successfully. The reproducibility of the measurements is very good. The measured emittances as a function of the main solenoid current have been compared to simulation results which describe the tendency of the measurements very well. For optimal settings of the accelerator parameters, normalized emittances below the design value of 2 mm mrad have been measured in both planes.

Outlook

The measurements presented within this thesis are performed in a diagnostic section downstream the first bunch compressor (BC2 section). In this section wire scanners can also be used for beam profile measurements. A comparison of the beam distributions measured with OTR monitors to those from wire scanners needs to be done.

We have only presented emittances containing the contributions of the dispersion (effective emittances). Determination of the dispersion is needed to determine pure betatron emittances.

In principle, we can also measure the correlations between the (x, x') - and (y, y') -phase spaces. Intrinsic emittances can be used to describe the occupied phase space area in such a case. We found that for some settings of the

accelerator parameters we obtain imaginary values for the intrinsic emittances. The reason for this has to be investigated. Possible sources are small alignment errors of the quadrupoles in the FODO lattice and of the optical system of the OTR monitors.

The emittance can also be measured in a diagnostic section in front of the undulators (SUND section). Synchrotron light on some of the screens and problems with the light yield of two screens in this section should be further investigated. A comparison between the measured emittances in the two diagnostic sections would give us information on the emittance transport through the accelerator.

A Transfer matrices of important beam line elements

The derivation of the most common beam line elements can be found in [RS93] and [Bro82]. Here we present only the results. It is always assumed that the elements are mounted in a way that they do not produce any coupling between the (x, x') - and (y, y') -plane.

Drift Space is the simplest element in a beam line. In the matrix formalism it can be described by the transfer matrix

$$\mathbf{R}_{\text{Drift}}(l) = \begin{pmatrix} 1 & l & 0 & 0 & 0 & 0 \\ 0 & 1 & 0 & 0 & 0 & 0 \\ 0 & 0 & 1 & l & 0 & 0 \\ 0 & 0 & 0 & 1 & 0 & 0 \\ 0 & 0 & 0 & 0 & 1 & 0 \\ 0 & 0 & 0 & 0 & 0 & 1 \end{pmatrix}, \quad (\text{A.1})$$

where l denotes the length of the drift space along the beam line. Since $1/\rho = 0$, where ρ denotes the bending radius of the reference trajectory, no dispersion is created in a drift space (see Eq. (2.12)).

Quadrupole Magnet with a uniform magnetic field gradient g can be described with help of a parameter $k = eg/p$, where p is the reference momentum of the particles. For $k > 0$ the transfer matrix is

$$\mathbf{R}_{\text{Q}}(k, l) = \begin{pmatrix} \cosh \phi & \frac{\sinh \phi}{\sqrt{|k|}} & 0 & 0 & 0 & 0 \\ \sqrt{|k|} \sinh \phi & \cosh \phi & 0 & 0 & 0 & 0 \\ 0 & 0 & \cos \phi & \frac{\sin \phi}{\sqrt{|k|}} & 0 & 0 \\ 0 & 0 & -\sqrt{|k|} \sin \phi & \cos \phi & 0 & 0 \\ 0 & 0 & 0 & 0 & 0 & 1 \\ 0 & 0 & 0 & 0 & 0 & 1 \end{pmatrix}. \quad (\text{A.2})$$

For $k < 0$ the on-diagonal 2×2 -matrices for x and y have to be interchanged:

$$\mathbf{R}_{\text{Q}}(k, l) = \begin{pmatrix} \cos \phi & \frac{\sin \phi}{\sqrt{|k|}} & 0 & 0 & 0 & 0 \\ -\sqrt{|k|} \sin \phi & \cos \phi & 0 & 0 & 0 & 0 \\ 0 & 0 & \cosh \phi & \frac{\sinh \phi}{\sqrt{|k|}} & 0 & 0 \\ 0 & 0 & \sqrt{|k|} \sinh \phi & \cosh \phi & 0 & 0 \\ 0 & 0 & 0 & 0 & 0 & 1 \\ 0 & 0 & 0 & 0 & 0 & 1 \end{pmatrix}. \quad (\text{A.3})$$

In both equations $\phi = l\sqrt{|k|}$, where l is the magnetic length of the quadrupole. For $k > 0$ the quadrupole is focusing in the vertical plane and defocusing in the horizontal plane. For $k < 0$ the situation is vice versa. Since $1/\rho = 0$, no dispersion is created in a quadrupole magnet.

Sector Dipole Magnet is a dipole magnet whose end faces are perpendicular to the central beam trajectory. The transfer matrix of a horizontally deflecting sector dipole magnet with a uniform magnetic field is

$$\mathbf{R}_{\text{S}}(\rho_x, \alpha) = \begin{pmatrix} \cos \alpha & \rho_x \sin \alpha & 0 & 0 & 0 & \rho_x(1 - \cos \alpha) \\ -\frac{\sin \alpha}{\rho_x} & \cos \alpha & 0 & 0 & 0 & \sin \alpha \\ 0 & 0 & 1 & \rho_x \alpha & 0 & 0 \\ 0 & 0 & 0 & 1 & 0 & 0 \\ -\sin \alpha & -\rho_x(1 - \cos \alpha) & 0 & 0 & 1 & -\rho_x(\alpha - \sin \alpha) \\ 0 & 0 & 0 & 0 & 0 & 1 \end{pmatrix}. \quad (\text{A.4})$$

Here α is the deflection angle and ρ_x denotes the bending radius of the beam trajectory. Since $1/\rho_x \neq 0$, horizontal dispersion is generated.

Rectangular Dipole Magnet is a dipole magnet with parallel magnet faces, i.e. its end faces are not perpendicular to the central beam trajectory. If the magnet is installed symmetrically with respect to the central beam trajectory, it can be described introducing an additional edge focusing matrix

$$\mathbf{F}(\rho_x, \alpha) = \begin{pmatrix} 1 & 0 & 0 & 0 & 0 & 0 \\ \frac{\tan \alpha/2}{\rho_x} & 1 & 0 & 0 & 0 & 0 \\ 0 & 0 & 1 & 0 & 0 & 0 \\ 0 & 0 & -\frac{\tan \alpha/2}{\rho_x} & 1 & 0 & 0 \\ 0 & 0 & 0 & 0 & 1 & 0 \\ 0 & 0 & 0 & 0 & 0 & 1 \end{pmatrix}. \quad (\text{A.5})$$

The transfer matrix for the rectangular dipole magnet can then be expressed as a matrix product of $\mathbf{F}(\rho_x, \alpha)$ and $\mathbf{R}_{\text{S}}(\rho_x, \alpha)$:

$$\mathbf{R}_{\text{RDM}}(\rho_x, \alpha) = \mathbf{F}(\rho_x, \alpha) \cdot \mathbf{R}_{\text{S}}(\rho_x, \alpha) \cdot \mathbf{F}(\rho_x, \alpha). \quad (\text{A.6})$$

Since $1/\rho_x \neq 0$, horizontal dispersion is generated.

B Symplectic transformation to calculate the intrinsic emittances

The symplectic transformation (see Eq. (2.49)) to calculate the intrinsic emittances is presented in this section. The derivation can be found in [Kub99].

An n -dimensional transformation matrix \mathbf{U} is called symplectic, if it fulfils the symplecticity condition [Wie03b]

$$\mathbf{U}^T \mathbf{J}_n \mathbf{U} = \mathbf{J}_n, \quad (\text{B.1})$$

where \mathbf{J}_n denotes the n -dimensional unit symplectic matrix composed of $n/2$, n even, submatrices $\begin{pmatrix} 0 & 1 \\ -1 & 0 \end{pmatrix}$:

$$\mathbf{J}_n = \begin{pmatrix} 0 & 1 & & & & \\ -1 & 0 & & & & \\ & & \ddots & & & \\ & & & \ddots & & \\ & & & & 0 & 1 \\ 0 & & & & -1 & 0 \end{pmatrix}. \quad (\text{B.2})$$

According to [Kub99] the symplectic transformation matrix \mathbf{U} which yields the intrinsic emittances as given in Eq. (2.49) can be calculated as described in the following. Solving the eigenvalue problem

$$\mathbf{J}_4 \boldsymbol{\sigma}^{4\text{D}} \mathbf{x} = \lambda \mathbf{x} \quad (\text{B.3})$$

yields four imaginary eigenvalues $\lambda^{(j)}$ and four imaginary eigenvectors $\mathbf{x}^{(j)}$. The eigenvectors $\mathbf{x}^{(j)}$ can be separated into imaginary and real parts: $\mathbf{x}_i^{(j)}$ and $\mathbf{x}_r^{(j)}$. The four eigenvectors can be expressed as

$$\begin{aligned} \mathbf{x}^{(1)} &= \mathbf{x}_r^{(1)} + i\mathbf{x}_i^{(1)} & \mathbf{x}^{(2)} &= \mathbf{x}_r^{(1)} - i\mathbf{x}_i^{(1)} \\ \mathbf{x}^{(3)} &= \mathbf{x}_r^{(3)} + i\mathbf{x}_i^{(3)} & \mathbf{x}^{(4)} &= \mathbf{x}_r^{(3)} - i\mathbf{x}_i^{(3)}. \end{aligned} \quad (\text{B.4})$$

The same separation for the eigenvalues $\lambda^{(i)}$ yields

$$\begin{aligned} \lambda^{(1)} &= i\lambda_i^{(1)} & \lambda^{(2)} &= -i\lambda_i^{(1)} \\ \lambda^{(3)} &= i\lambda_i^{(3)} & \lambda^{(4)} &= -i\lambda_i^{(3)}. \end{aligned} \quad (\text{B.5})$$

With Eq. (B.4) the matrix \mathbf{U} can be expressed as

$$\mathbf{U} = \begin{pmatrix} \frac{\mathbf{x}_r^{(1)}}{\sqrt{\mathbf{x}^{(1)T} \mathbf{J} \mathbf{x}^{(1)}}} & \frac{\mathbf{x}_i^{(1)}}{\sqrt{\mathbf{x}^{(1)T} \mathbf{J} \mathbf{x}^{(1)}}} & \frac{\mathbf{x}_r^{(3)}}{\sqrt{\mathbf{x}^{(3)T} \mathbf{J} \mathbf{x}^{(3)}}} & \frac{\mathbf{x}_i^{(3)}}{\sqrt{\mathbf{x}^{(3)T} \mathbf{J} \mathbf{x}^{(3)}}} \end{pmatrix}. \quad (\text{B.6})$$

It can also be shown that $\mathbf{U}^T \boldsymbol{\sigma}^{4\text{D}} \mathbf{U}$ is related to the eigenvalues above as

$$\mathbf{U}^T \boldsymbol{\sigma}^{4\text{D}} \mathbf{U} = \begin{pmatrix} \lambda_i^{(1)} & 0 & 0 & 0 \\ 0 & \lambda_i^{(1)} & 0 & 0 \\ 0 & 0 & \lambda_i^{(3)} & 0 \\ 0 & 0 & 0 & \lambda_i^{(3)} \end{pmatrix}. \quad (\text{B.7})$$

C Tables with measurement results

main solenoid current [A]	30.01.2005 time	$\epsilon_{N,x} \pm \text{stat. err.} \pm \text{syst. err.}$ [mm mrad]	ξ_x	$\epsilon_{N,x}$ [mm mrad]
		Fit 100 %		MENT 100%
273.0	13:02	$8.27 \pm 0.22 \pm 0.43$	1.011	8.67
273.0	13:09	$7.20 \pm 0.20 \pm 0.30$	1.128	7.28
275.0	12:16	$6.02 \pm 0.16 \pm 0.29$	1.020	5.59
275.0	12:24	$5.52 \pm 0.18 \pm 0.21$	1.115	5.38
276.0	13:27	$4.90 \pm 0.11 \pm 0.21$	1.067	4.55
276.0	13:38	$5.43 \pm 0.14 \pm 0.23$	1.044	5.08
277.0	09:45	$4.13 \pm 0.18 \pm 0.21$	1.008	3.74
277.0	11:56	$4.47 \pm 0.14 \pm 0.22$	1.014	4.09
278.0	13:58	$4.83 \pm 0.20 \pm 0.17$	1.215	4.24
278.0	14:10	$4.49 \pm 0.11 \pm 0.22$	1.027	4.07
279.0	10:04	$4.50 \pm 0.14 \pm 0.20$	1.048	4.29
279.0	10:12	$4.73 \pm 0.15 \pm 0.22$	1.029	4.50
280.0	14:31	$6.01 \pm 0.23 \pm 0.24$	1.130	6.36
280.0	14:40	$6.28 \pm 0.17 \pm 0.30$	1.030	6.10
281.0	10:31	$6.74 \pm 0.21 \pm 0.32$	1.013	7.01
281.0	10:39	$6.71 \pm 0.14 \pm 0.33$	1.024	6.27
283.0	11:01	$9.64 \pm 0.21 \pm 0.45$	1.071	10.03
283.0	11:09	$9.79 \pm 0.22 \pm 0.52$	1.039	10.00
285.0	11:26	$12.76 \pm 0.39 \pm 0.67$	1.035	12.84
285.0	11:33	$12.60 \pm 0.35 \pm 0.64$	1.034	12.96
		Fit 90 %		MENT 90%
273.0	13:02	$6.25 \pm 0.19 \pm 0.32$	1.002	6.11
273.0	13:09	$5.11 \pm 0.16 \pm 0.21$	1.102	5.00
275.0	12:16	$3.78 \pm 0.15 \pm 0.19$	1.032	3.57
275.0	12:24	$3.44 \pm 0.10 \pm 0.14$	1.067	3.33
276.0	13:27	$2.68 \pm 0.08 \pm 0.16$	1.002	2.52
276.0	13:38	$3.14 \pm 0.10 \pm 0.17$	1.000	3.03
277.0	09:45	$2.64 \pm 0.14 \pm 0.16$	1.013	2.17
277.0	11:56	$2.45 \pm 0.11 \pm 0.15$	1.009	2.30
278.0	13:58	$2.49 \pm 0.12 \pm 0.11$	1.047	2.27
278.0	14:10	$2.51 \pm 0.09 \pm 0.15$	1.004	2.25
279.0	10:04	$2.52 \pm 0.09 \pm 0.14$	1.004	2.42
279.0	10:12	$2.85 \pm 0.12 \pm 0.16$	1.001	2.61
280.0	14:31	$3.71 \pm 0.16 \pm 0.16$	1.050	3.83
280.0	14:40	$3.82 \pm 0.16 \pm 0.24$	1.009	3.74
281.0	10:31	$4.22 \pm 0.17 \pm 0.24$	1.003	4.35
281.0	10:39	$4.18 \pm 0.12 \pm 0.25$	1.005	3.87
283.0	11:01	$6.58 \pm 0.19 \pm 0.34$	1.011	6.71
283.0	11:09	$6.68 \pm 0.18 \pm 0.43$	1.005	6.55
285.0	11:26	$8.55 \pm 0.26 \pm 0.49$	1.000	8.57
285.0	11:33	$8.65 \pm 0.17 \pm 0.54$	1.000	8.73

Table C.1: Measured normalized horizontal rms emittances for different main solenoid currents. Top: 100% beam intensity, bottom: 90% beam intensity.

main solenoid current [A]	30.01.2005 time	$\epsilon_{N,y} \pm \begin{matrix} \text{stat.} \\ \text{err.} \end{matrix} \pm \begin{matrix} \text{syst.} \\ \text{err.} \end{matrix}$ [mm mrad]	ξ_y	$\epsilon_{N,y}$ [mm mrad]
Fit 100 %				MENT 100%
273.0	13:02	$6.46 \pm 0.10 \pm 0.35$	1.019	6.86
273.0	13:09	$6.14 \pm 0.13 \pm 0.32$	1.052	6.34
275.0	12:16	$5.06 \pm 0.11 \pm 0.21$	1.077	4.91
275.0	12:24	$5.23 \pm 0.13 \pm 0.20$	1.082	4.99
276.0	13:27	$5.09 \pm 0.10 \pm 0.30$	1.021	5.02
276.0	13:38	$4.71 \pm 0.10 \pm 0.23$	1.013	4.61
277.0	09:45	$5.14 \pm 0.15 \pm 0.27$	1.007	5.00
277.0	11:56	$4.93 \pm 0.13 \pm 0.24$	1.012	4.75
278.0	13:58	$5.94 \pm 0.13 \pm 0.30$	1.003	5.47
278.0	14:10	$5.82 \pm 0.14 \pm 0.30$	1.023	5.17
279.0	10:04	$6.61 \pm 0.16 \pm 0.35$	1.015	6.40
279.0	10:12	$6.59 \pm 0.12 \pm 0.33$	1.025	6.49
280.0	14:31	$8.30 \pm 0.15 \pm 0.39$	1.016	8.11
280.0	14:40	$7.71 \pm 0.27 \pm 0.43$	1.005	7.68
281.0	10:31	$8.63 \pm 0.26 \pm 0.44$	1.002	8.60
281.0	10:39	$8.86 \pm 0.20 \pm 0.50$	1.003	8.57
283.0	11:01	$11.22 \pm 0.53 \pm 0.70$	1.014	11.35
283.0	11:09	$11.07 \pm 0.33 \pm 0.72$	1.008	11.01
285.0	11:26	$11.37 \pm 0.42 \pm 0.58$	1.006	11.49
285.0	11:33	$11.45 \pm 0.57 \pm 0.55$	1.007	11.64
Fit 90 %				MENT 90%
273.0	13:02	$4.43 \pm 0.06 \pm 0.25$	1.001	4.80
273.0	13:09	$4.15 \pm 0.08 \pm 0.24$	1.018	4.46
275.0	12:16	$3.41 \pm 0.08 \pm 0.15$	1.049	3.45
275.0	12:24	$3.73 \pm 0.09 \pm 0.16$	1.038	3.65
276.0	13:27	$3.83 \pm 0.10 \pm 0.26$	1.035	3.65
276.0	13:38	$3.61 \pm 0.11 \pm 0.19$	1.005	3.29
277.0	9:45	$3.65 \pm 0.13 \pm 0.19$	1.006	3.48
277.0	11:56	$3.72 \pm 0.13 \pm 0.20$	1.001	3.38
278.0	13:58	$4.39 \pm 0.09 \pm 0.25$	1.005	3.87
278.0	14:10	$4.07 \pm 0.11 \pm 0.23$	1.001	3.62
279.0	10:04	$4.76 \pm 0.13 \pm 0.26$	1.064	4.38
279.0	10:12	$4.68 \pm 0.09 \pm 0.24$	1.078	4.41
280.0	14:31	$6.20 \pm 0.12 \pm 0.30$	1.028	5.60
280.0	14:40	$5.72 \pm 0.25 \pm 0.33$	1.003	5.31
281.0	10:31	$6.52 \pm 0.27 \pm 0.35$	1.001	6.02
281.0	10:39	$6.86 \pm 0.17 \pm 0.37$	1.002	6.16
283.0	11:01	$8.80 \pm 0.54 \pm 0.55$	1.024	8.36
283.0	11:09	$8.72 \pm 0.36 \pm 0.56$	1.015	8.14
285.0	11:26	$8.92 \pm 0.40 \pm 0.43$	1.006	8.49
285.0	11:33	$9.05 \pm 0.53 \pm 0.42$	1.008	8.67

Table C.2: Measured normalized vertical rms emittances for different main solenoid currents. Top: 100% beam intensity, bottom: 90% beam intensity.

ACC1 off-crest phase [deg]	06.02.2005 time	$\epsilon_{N,x} \pm \text{stat. err.} \pm \text{syst. err.}$ [mm mrad]	ξ_x	$\epsilon_{N,x}$ [mm mrad]
Fit 100 %			MENT 100%	
0	11:00	$3.08 \pm 0.10 \pm 0.18$	1.039	3.13
0	11:09	$3.40 \pm 0.11 \pm 0.19$	1.012	3.48
-1	16:20	$2.91 \pm 0.11 \pm 0.15$	1.130	3.15
-1	16:37	$3.87 \pm 0.14 \pm 0.21$	1.031	4.07
-2	11:54	$4.13 \pm 0.13 \pm 0.22$	1.008	4.39
-2	12:04	$4.19 \pm 0.16 \pm 0.20$	1.010	4.34
-3	15:56	$6.10 \pm 0.30 \pm 0.31$	1.063	6.13
-3	16:04	$6.25 \pm 0.30 \pm 0.28$	1.061	6.15
-4	12:53	$5.00 \pm 0.24 \pm 0.29$	1.006	5.28
-4	13:00	$4.95 \pm 0.24 \pm 0.26$	1.029	5.06
-5	15:27	$7.48 \pm 0.36 \pm 0.60$	1.359	7.51
-5	15:37	$7.03 \pm 0.36 \pm 0.35$	1.051	7.06
-5	15:47	$8.16 \pm 0.36 \pm 0.43$	1.039	7.83
-6	13:47	$7.63 \pm 0.36 \pm 0.45$	1.008	7.68
-6	13:55	$8.60 \pm 0.54 \pm 0.51$	1.029	9.00
-7	15:18	$22.5 \pm 1.3 \pm 1.1$	1.048	22.7
-8	14:35	$31.9 \pm 1.8 \pm 1.9$	1.583	33.6
-8	14:51	$27.5 \pm 1.7 \pm 1.8$	1.074	27.2
Fit 90 %			MENT 90%	
0	11:00	$1.65 \pm 0.05 \pm 0.09$	1.001	1.73
0	11:09	$1.85 \pm 0.06 \pm 0.10$	1.003	1.93
-1	16:20	$1.73 \pm 0.07 \pm 0.09$	1.031	1.74
-1	16:37	$2.28 \pm 0.08 \pm 0.14$	1.007	2.35
-2	11:54	$2.34 \pm 0.09 \pm 0.11$	1.045	2.44
-2	12:04	$2.30 \pm 0.09 \pm 0.10$	1.056	2.38
-3	15:56	$3.25 \pm 0.13 \pm 0.18$	1.023	3.31
-3	16:04	$3.20 \pm 0.14 \pm 0.15$	1.031	3.25
-4	12:53	$2.60 \pm 0.12 \pm 0.14$	1.007	2.75
-4	13:00	$2.56 \pm 0.12 \pm 0.12$	1.013	2.70
-5	15:27	$4.68 \pm 0.21 \pm 0.40$	1.145	4.54
-5	15:37	$3.68 \pm 0.15 \pm 0.22$	1.020	3.73
-5	15:47	$4.36 \pm 0.18 \pm 0.29$	1.021	4.32
-6	13:47	$4.62 \pm 0.22 \pm 0.20$	1.043	4.51
-6	13:55	$5.27 \pm 0.29 \pm 0.24$	1.134	5.26
-7	15:18	$13.46 \pm 0.65 \pm 0.53$	1.151	14.35
-8	14:35	$22.8 \pm 0.9 \pm 1.8$	1.777	24.5
-8	14:51	$17.4 \pm 0.9 \pm 1.1$	1.012	17.1

Table C.3: Measured normalized rms emittances for different ACC1 off-crest phases (horizontal plane). Top: 100% beam intensity, bottom: 90% beam intensity.

ACC1 off-crest phase [deg]	06.02.2005 time	$\epsilon_{N,y} \pm \begin{matrix} \text{stat.} \\ \text{err.} \end{matrix} \pm \begin{matrix} \text{syst.} \\ \text{err.} \end{matrix}$ [mm mrad]	ξ_y	$\epsilon_{N,y}$ [mm mrad]
Fit 100 %				MENT 100%
0	11:00	$3.35 \pm 0.07 \pm 0.16$	1.022	3.27
0	11:09	$3.50 \pm 0.08 \pm 0.16$	1.017	3.44
-1	16:20	$3.31 \pm 0.07 \pm 0.18$	1.018	3.25
-1	16:37	$3.30 \pm 0.08 \pm 0.19$	1.017	3.23
-2	11:54	$3.71 \pm 0.07 \pm 0.16$	1.026	3.66
-2	12:04	$3.74 \pm 0.08 \pm 0.16$	1.047	3.65
-3	15:56	$3.45 \pm 0.09 \pm 0.21$	1.008	3.35
-3	16:04	$3.56 \pm 0.08 \pm 0.20$	1.009	3.45
-4	12:53	$3.87 \pm 0.09 \pm 0.19$	1.002	3.89
-4	13:00	$3.76 \pm 0.09 \pm 0.18$	1.003	3.83
-5	15:27	$3.62 \pm 0.11 \pm 0.19$	1.029	3.26
-5	15:37	$3.56 \pm 0.08 \pm 0.19$	1.007	3.49
-5	15:47	$3.41 \pm 0.08 \pm 0.19$	1.003	3.25
-6	13:47	$3.97 \pm 0.08 \pm 0.19$	1.014	4.15
-6	13:55	$4.20 \pm 0.11 \pm 0.21$	1.016	4.27
-7	15:18	$3.66 \pm 0.11 \pm 0.18$	1.008	3.39
-8	14:35	$3.88 \pm 0.19 \pm 0.28$	1.037	4.07
-8	14:51	$3.60 \pm 0.13 \pm 0.19$	1.043	3.47
Fit 90 %				MENT 90%
0	11:00	$2.30 \pm 0.05 \pm 0.12$	1.003	2.24
0	11:09	$2.40 \pm 0.06 \pm 0.13$	1.002	2.33
-1	16:20	$2.36 \pm 0.05 \pm 0.13$	1.013	2.32
-1	16:37	$2.36 \pm 0.05 \pm 0.13$	1.012	2.29
-2	11:54	$2.52 \pm 0.04 \pm 0.12$	1.013	2.47
-2	12:04	$2.53 \pm 0.05 \pm 0.12$	1.012	2.46
-3	15:56	$2.44 \pm 0.05 \pm 0.16$	1.006	2.37
-3	16:04	$2.53 \pm 0.05 \pm 0.15$	1.007	2.42
-4	12:53	$2.72 \pm 0.05 \pm 0.16$	1.007	2.66
-4	13:00	$2.64 \pm 0.06 \pm 0.14$	1.002	2.61
-5	15:27	$2.43 \pm 0.05 \pm 0.14$	1.007	2.31
-5	15:37	$2.59 \pm 0.05 \pm 0.15$	1.002	2.45
-5	15:47	$2.43 \pm 0.05 \pm 0.14$	1.011	2.30
-6	13:47	$2.71 \pm 0.06 \pm 0.15$	1.022	2.77
-6	13:55	$2.77 \pm 0.06 \pm 0.16$	1.015	2.79
-7	15:18	$2.39 \pm 0.05 \pm 0.13$	1.010	2.30
-8	14:35	$2.87 \pm 0.07 \pm 0.18$	1.011	2.79
-8	14:51	$2.47 \pm 0.07 \pm 0.15$	1.023	2.34

Table C.4: Measured normalized rms emittances for different ACC1 off-crest phases (vertical plane). Top: 100% beam intensity, bottom: 90% beam intensity.

11.02.2005 time	$\epsilon_{N,x} \pm \begin{matrix} \text{stat.} \\ \text{err.} \end{matrix} \pm \begin{matrix} \text{syst.} \\ \text{err.} \end{matrix}$ [mm mrad]	ξ_x	$\epsilon_{N,x}$ [mm mrad]
	Fit 100 %		MENT 100%
4:19	$2.93 \pm 0.11 \pm 0.14$	1.036	2.94
4:27	$2.99 \pm 0.11 \pm 0.13$	1.019	3.04
4:35	$2.85 \pm 0.08 \pm 0.12$	1.020	2.90
4:43	$3.01 \pm 0.10 \pm 0.14$	1.020	3.02
4:51	$2.85 \pm 0.11 \pm 0.12$	1.030	2.89
4:59	$2.94 \pm 0.11 \pm 0.13$	1.025	2.97
5:07	$2.70 \pm 0.10 \pm 0.13$	1.030	2.81
5:16	$2.74 \pm 0.13 \pm 0.12$	1.023	2.77
5:24	$2.85 \pm 0.09 \pm 0.13$	1.029	3.02
5:33	$2.80 \pm 0.10 \pm 0.12$	1.030	2.88

	Fit 90 %		MENT 90%
4:19	$1.63 \pm 0.09 \pm 0.06$	1.169	1.67
4:27	$1.72 \pm 0.08 \pm 0.07$	1.110	1.77
4:35	$1.62 \pm 0.06 \pm 0.06$	1.117	1.67
4:43	$1.72 \pm 0.08 \pm 0.07$	1.117	1.76
4:51	$1.59 \pm 0.07 \pm 0.06$	1.154	1.64
4:59	$1.69 \pm 0.07 \pm 0.07$	1.121	1.71
5:07	$1.54 \pm 0.06 \pm 0.07$	1.135	1.60
5:16	$1.53 \pm 0.09 \pm 0.06$	1.129	1.57
5:24	$1.67 \pm 0.06 \pm 0.07$	1.125	1.77
5:33	$1.61 \pm 0.07 \pm 0.07$	1.140	1.66

Table C.5: Reproducibility of the emittance measurement (horizontal plane). Top: measured normalized rms emittances for 100% beam intensity. Bottom: measured normalized rms emittances for 90% beam intensity.

11.02.2005 time	$\epsilon_{N,y} \pm \begin{matrix} \text{stat.} \\ \text{err.} \end{matrix} \pm \begin{matrix} \text{syst.} \\ \text{err.} \end{matrix}$ [mm mrad]	ξ_y	$\epsilon_{N,y}$ [mm mrad]
	Fit 100 %		MENT 100%
4:19	$2.53 \pm 0.07 \pm 0.13$	1.022	2.44
4:27	$2.63 \pm 0.08 \pm 0.13$	1.012	2.50
4:35	$2.61 \pm 0.08 \pm 0.14$	1.004	2.53
4:43	$2.55 \pm 0.08 \pm 0.14$	1.005	2.51
4:51	$2.55 \pm 0.06 \pm 0.15$	1.002	2.49
4:59	$2.54 \pm 0.07 \pm 0.13$	1.009	2.45
5:07	$2.57 \pm 0.06 \pm 0.15$	1.002	2.52
5:16	$2.58 \pm 0.07 \pm 0.15$	1.008	2.51
5:24	$2.47 \pm 0.07 \pm 0.14$	1.008	2.44
5:33	$2.60 \pm 0.08 \pm 0.13$	1.005	2.52

	Fit 90 %		MENT 90%
4:19	$1.62 \pm 0.04 \pm 0.09$	1.014	1.55
4:27	$1.61 \pm 0.04 \pm 0.09$	1.016	1.54
4:35	$1.61 \pm 0.04 \pm 0.10$	1.009	1.55
4:43	$1.58 \pm 0.03 \pm 0.10$	1.012	1.53
4:51	$1.63 \pm 0.03 \pm 0.10$	1.008	1.55
4:59	$1.59 \pm 0.04 \pm 0.09$	1.013	1.52
5:07	$1.62 \pm 0.04 \pm 0.11$	1.010	1.55
5:16	$1.64 \pm 0.03 \pm 0.10$	1.009	1.56
5:24	$1.56 \pm 0.03 \pm 0.10$	1.014	1.48
5:33	$1.58 \pm 0.04 \pm 0.09$	1.015	1.52

Table C.6: Reproducibility of the emittance measurement (vertical plane). Top: measured normalized rms emittances for 100% beam intensity. Bottom: measured normalized rms emittances for 90% beam intensity.

References

- [A⁺02a] V. Ayvazyan et al., *Generation of GW radiation pulses from a VUV free electron laser operating in the femtosecond regime*, Phys. Rev. Lett. 88 **104802** (2002).
- [A⁺02b] V. Ayvazyan et al., *A new powerful source for coherent VUV radiation: Demonstration of experimental growth and saturation at the TTF free electron laser*, Eur. Phys. J. D 20 (2002), 149–156.
- [AST] www.desy.de/~mpyflo/Astra_documentation.
- [B⁺01] R. Brinkmann et al., *TESLA: The superconducting electron positron linear collider with an integrated X-ray laser laboratory. Technical design report. Part 2: The accelerator*, Tech. report, DESY-01-011, 2001.
- [Bas02] Basler Vision Technologies, Ahrensburg, Germany, *Basler A301f Camera User's Manual*, May 2002.
- [BCF⁺02] R. Baraniuk et al., *Rice Wavelet Toolbox*, Dec 2002, www.dsp.rice.edu/software/rwt.shtml.
- [BL01] S. A. Bogacz and V. A. Lebedev, *Betatron motion with coupling of horizontal and vertical degrees of freedom*, eConf **C010630** (2001), T511.
- [Bro82] K. L. Brown, *A first- and second-order matrix theory for the design of beam transport systems and charged particle spectrometers*, SLAC Report 75 (1982).
- [Buo93] J. Buon, *Multi-dimensional beam emittance and β -functions*, Proceedings of the Particle Accelerator Conference 1993 (Washington DC), May 17-20 1993, pp. 469–471.
- [C⁺05] L. Catani et al., *A large distributed digital camera system for accelerator beam diagnostics*, Proceedings of PCaPAC 2005 (Hayama, Japan), March 22-25 2005.
- [Cas03] P. Castro, *Monte Carlo simulations of emittance measurements at TTF2*, DESY-TECHNICAL-NOTE-2003-03 (2003).
- [CCC⁺04] A. Cianchi et al., *Commissioning of the OTR beam profile monitor system at the TTF/VUV-FEL injector*, Proceedings of the EPAC 2004 Conference (Lucerne, Switzerland), July 5-9 2004, pp. 2619–2621.
- [Cia05] A. Cianchi, INFN-Roma2, private communication, March 2005.
- [Com94] M. Comunian, *Emittance measurements in Compact Linear Collider Test Facility*, Draft copy of a thesis presented at Università degli Studi di Padova, Dipartimento di Fisica "Galileo Galilei", 1994.
- [Efr02] Efremov Institute Saint-Petersburg, *Certificate of quadrupole magnet TQA-xxx*, unpublished, 2002.
- [Gei99] M. Geitz, *Investigation of the transverse and longitudinal beam parameters at the TESLA Test Facility linac*, Ph.D. thesis, University of Hamburg, Nov 1999, published as DESY report DESY-THESIS-1999-033.
- [GF45] V. Ginzburg and I. Frank, Journ. Phys. USSR 9 **353** (1945).
- [HBF⁺03] K. Honkavaara et al., *Design of OTR beam profile monitors for the TESLA Test Facility, Phase 2 (TTF2)*, Proceedings of the 2003 Particle Accelerator Conference (Portland), May 12-16 2003, pp. 2476–2479.
- [HC04] K. Honkavaara and J.-P. Carneiro, *Considerations of emittance measurements at the TTF/VUV-FEL injector*, unpublished, Feb 2004.
- [Hol05] Y. Holler, DESY, private communication, May 2005.
- [Isi] www.isi-seal.com/searchs/doc/fusedsilicaintro.htm.
- [K⁺04] M. Krasilnikov et al., *Optimizing the PITZ electron source for the VUV-FEL*, Proceedings of EPAC 2004 (Lucerne, Switzerland), July 5-9 2004, pp. 360–362.
- [Kim05] Y. Kim, DESY, *Astra simulations*, private communication, April 2005.
- [Kub99] K. Kubo, *How to calculate 'intrinsic' emittances from 4-dimensional beam matrix*, ATF Internal Report 99-02 (1999).
- [Lab] LabVIEWTM, National Instruments, Austin (Tx).
- [Lin01] M. Lindemann, *Wavelet-Thresholding-Methoden in der Signal- und Bildverarbeitung*, Diplomarbeit, Universität Potsdam, Jan 2001.
- [MAA⁺04] V. Miltchev et al., *Transverse emittance measurements at the photo injector test facility at DESY Zeuthen*, Proceedings of the FEL 2004 Conference (Trieste, Italy), Aug 29 - Sep 3 2004.
- [Min79] G. N. Minerbo, *MENT: A Maximum Entropy Algorithm for reconstructing a source from projection data*, Comp. Graphics Image Proc. **48** (1979).
- [MMSS91] N. Merminga, P. Morton, J. Seeman and W. Spence, *Transverse phase space in the presence of dispersion*, SLAC-PUB-5514 (May 1991).

- [Mot85] C. T. Mottershead, *Maximum entropy beam diagnostic tomography*, IEEE Transactions on Nuclear Science **NS-32**, No. 5 (1985).
- [MSJ81] G. N. Minerbo, O. R. Sander and R. A. Jameson, *Four-dimensional beam tomography*, IEEE Transactions on Nuclear Science **NS-28**, No. 3 (1981).
- [MZ03] M. Minty and F. Zimmermann, *Measurements and control of charged particle beams*, Springer, Berlin, Heidelberg, New York, 2003.
- [PTVF93] W. H. Press, S. A. Teukolsky, W. T. Vetterling and B. P. Flannery, *Numerical Recipes in C, The Art of Scientific Computing*, Cambridge University Press, Cambridge, New York, Port Chester, Melbourne, Sydney, 1993.
- [RS93] J. Roßbach and P. Schmüser, *Basic course on accelerator optics, Lectures given at the CERN Accelerator School*, DESY internal report M-93-02 (1993).
- [S⁺02a] S. Schreiber et al., *Improved operation of the TTF photoinjector for FEL operation*, Proceedings of EPAC 2002 (Paris, France), June 3-7 2002, pp. 1804–1806.
- [S⁺02b] J. Sekutowicz et al., *A design of a 3rd harmonic cavity for the TTF2 photoinjector*, TESLA-FEL Report 2002-05, DESY (2002).
- [Sch04a] J. Scheins, *Tomographic reconstruction of transverse and longitudinal phase space distributions using the Maximum Entropy Algorithm*, TESLA Report 2004-08 (2004).
- [Sch04b] S. Schreiber, *Commissioning of the VUV-FEL injector at TTF*, Proceedings of the EPAC 2004 Conference (Lucerne, Switzerland), July 5-9 2004, pp. 351–353.
- [SSY99] E. L. Saldin, E. A. Schneidmiller and M. Yurkov, *The physics of Free Electron Lasers*, Springer-Verlag, Berlin, 1999.
- [Stu04] F. Stulle, *A bunch compressor for small emittances and high peak currents at the VUV Free-Electron Laser*, Ph.D. thesis, University of Hamburg, Oct 2004, published as DESY report DESY-THESIS-2004-041.
- [The02] The TTF FEL Team, *SASE FEL at the TESLA Test Facility, Phase 2*, TESLA-FEL-2002-01, DESY (2002).
- [WE00] M. Woodley and P. Emma, *Measurement and correction of cross-plane coupling in transport lines*, SLAC-PUB 8581 (2000).
- [Wei03] H. Weise, *Superconducting RF structures - test facilities and results*, Proceedings of the 2003 Particle Accelerator Conference (Portland), May 12 - 16 2003, pp. 673–677.
- [Wet80] W. Wetherell, *The calculation of image quality; applied optics and optical engineering*, vol. III, Academic press, 1980.
- [Wie03a] H. Wiedemann, *Particle Accelerator Physics I, Basic principles and linear beam dynamics*, 2nd ed., Springer, Berlin, Heidelberg, New York, 2003.
- [Wie03b] H. Wiedemann, *Particle Accelerator Physics II, Nonlinear and higher-order beam dynamics*, 2nd ed., Springer, Berlin, Heidelberg, New York, 2003.

Acknowledgements

First of all, I would like to thank my advisors Prof. Dr. Jörg Roßbach and Prof. Dr. Peter Schmüser for introducing the field of accelerator physics to me and giving me the opportunity and the help to prepare my thesis at DESY.

I am grateful to Dr. Katja Honkavaara for her advice and support. Whenever I had a problem with my experimental and theoretical work, she was there to help me.

Special thanks to Dr. Siegfried Schreiber for the many fruitful discussions about topics like the VUV-FEL injector, error sources and calculation for my measurements.

Dr. Holger Schlarb, Dr. Klaus Flöttmann, and Dr. Dirk Nölle I would like to thank for their support and the many advices they gave to me.

For their assistance and advice with the OTR system and the image server I like to thank my Italian colleagues Dr. Michele Castellano, Dr. Luciano Catani, Dr. Alessandro Cianchi, and Enrica Chiadroni.

I want to thank Dr. Yujong Kim for providing me simulation results and for spending many hours with me doing emittance measurements.

Michael Röhrs I like to thank for the interesting discussions about emittance theory and his helpful advices to my thesis.

For his help with programming languages and any kind of computer problems I am indebted to Lars Fröhlich. Dr. Jürgen Scheins I like to thank for providing me his code of the MENT Algorithm. I am grateful to Dr. Pedro Castro for helping me with ROOT.

Special thanks to Kirsten Hacker and Martin Löhl for proof-reading my thesis and helping me to eliminate many errors in the English language.

I am grateful to my colleagues Dr. Nicoleta Baboi, Bolko Beutner, and Andy Bolzmann for many interesting discussions on various physical and non-physical topics.

I would like to thank the entire VUV-FEL shift crew for the chance to learn from them and for the measurements they made for me.

Finally, I want to thank my family for their support in all situations.